EXPLORING THE RELATIONSHIP BETWEEN MITOCHONDRIAL-LINKED CELL DEATH AND MUSCLE ATROPHY DURING OVARIAN CANCER PROGRESSION

Shahrzad Khajehzadehshoushtar

A THESIS SUBMITTED TO THE FACULTY OF GRADUATE STUDIES IN PARTIAL FULFILLMENT OF THE REQUIREMENTS FOR THE DEGREE OF MASTER OF SCIENCE

Graduate Program in Kinesiology and Health Sciences

York University

Toronto, Ontario

August 2024

Abstract

The mechanisms underlying muscle atrophy during ovarian cancer are not fully understood. This study investigated the role of mitochondrial hydrogen peroxide (mH_2O_2)-mediated apoptosis and necroptosis in muscle atrophy using an orthotopic epithelial ovarian cancer (EOC) model at 40 and 80 days of tumor progression. We also examined the effects of the mitochondrial-targeted antioxidant SkQ1 on mH_2O_2 levels, regulation of apoptosis and necroptosis, and atrophy. Contrary to existing literature, muscle atrophy preceded EOC-induced changes in mH_2O_2 emission, and SkQ1, despite lowering mH_2O_2, did not prevent atrophy. Apoptotic markers (mPT, caspase-3, -9 activity) were elevated early in EOC progression and remained high, while necroptosis markers (RIPK1, phosphorylated MLKL/total MLKL) decreased with cancer progression. EOC-induced changes in necroptosis were unaffected by SkQ1, whereas markers of apoptosis (caspase-3/-9 activities) were downregulated by SkQ1. This study lays a crucial foundation for future research into regulated cell death pathways as mechanisms of cancer-induced atrophy.

Acknowledgements

To Maman, Baba and Gramma, thank you for supporting me endlessly and always making my dreams your own. I hope to make you proud.

To my sister Helen, who knows too much about cancer cachexia for a 12-year-old, thank you for being my audience of one while I practiced presentations.

To Madison, Arshdeep, Brooke, Luca, Shivam, and Aditya, thank you for cheering me on when things were going well and more importantly, thank you for cheering me on when they weren't.

To Luca, I don't know how to thank you everything you've done for me, but thank you. It frightens me to think I won't be able to immediately run to my mentor for help anymore, but I wholeheartedly trust all the training you've provided me.

To Dr. Perry, who not only gave me the opportunity to pursue this degree but also encouraged me to investigate a topic I was (and still am) interested in. Thank you for responding to my email inquiry about an undergraduate project three years ago, for your endless support on weekdays, weekends, and holidays, and for teaching me that science is a creative subject.

To my Izzy, who has stood by me through all my career doubts and changes in direction. Thank you for being my rock (no promises I won't change directions again or apply for more farming jobs).

I didn't want to end my acknowledgements with a cheesy quote, but when else do you get to use a quote in life? Here it goes:

"*I have no special talent. I am only passionately curious*." – Albert Einstein

(Einstein may have stolen this from Chris Perry)

TABLE OF CONTENTS

LIST OF TABLES

LIST OF FIGURES

LIST OF SUPPLEMENTARY FIGURES

LIST OF ABBREVIATIONS

ATP	Adenosine Triphosphate
ADP	Adenosine Diphosphate
ANT	Adenine Nucleotide Translocase
APAF-1	Apoptotic Protease Activating Factor 1
B	Bv6
BAK	Bcl-2 Antagonist/Killer
BAX	BCL-2 Associated X
BCA	Bicinchoninic Acid Assay
Bcl-2	B-Cell Lymphoma-2 Anti-Apoptotic Protein
BID	BH3 Interacting-Domain Death Agonist
BLEB	Blebbistatin
BSA	Bovine Serum Albumin
Ca^{2+}	Calcium ion
CDNB	2,4-Dinitrochlorobenzene
cFLIP	Cellular FLICE-Like Inhibitory Protein
$cFLIP_L$	Cellular FLICE-Like Inhibitory Protein Long
CI	Complex I
cIAP1/2	Cellular Inhibitor Of Apoptosis Protein-1 And 2
CII	Complex II
CIII	Complex III
CIV	Complex IV
CK	Creatine Kinase
CoQ	Coenzyme Q
CRC	Calcium Retention Capacity
CSA	Cross-Sectional Area
Cyt C	Cytochrome C
DD	Death Domain
DMD	Duchenne Muscular Dystrophy
DMSO	Dimethylsulfoxide
e^-	Electron
E1	Ubiquitin-Activating Enzymes
E2	Ubiquitin-Conjugating Enzymes
E3	Ubiquitin-Ligase Enzymes
EDL	Extensor Digitorum Longus
EOC	Epithelial Ovarian Cancer
EOC-40	Epithelial Ovarian Cancer Injected Mice Assessed 40 Days Post Injection

EOC-40-SkQ1	Epithelial Ovarian Cancer Injected Mice, Subjected To Skq1 In Drinking Water, Assessed 40 Days Post Injection
EOC-80	Epithelial Ovarian Cancer Injected Mice Assessed 80 Days Post Injection
EOC-80-SkQ1	Epithelial Ovarian Cancer Injected Mice, Subjected To Skq1 In Drinking Water, Assessed 80 Days Post Injection
ETC	Electron Transport Chain
FADD	FAS-Associated Death Domain
FADH	Flavin Adenine Dinucleotide
$FADH_2$	Flavin Adenine Dinucleotide + Hydrogen (Reduced Form)
Fmax	Fluorescence Maximum
Gastroc	Gastrocnemius
GM	Growth Medium
H^+	Proton
H_2O	Water Molecule,
H_2O_2	Hydrogen Peroxide
I	Z-VAD-IEDT
ID8 EOC	Spontaneously transformed murine ovarian epithelial cells
IL-1	Interleukin-1
Il-6	Interleukin-6
IM	Inner Membrane
IMS	Intermembrane Space
KO	Knock Out
LF PVDF	Low-Fluorescence Polyvinylidene Difluoride Membrane
LUBAC	Linear Ubiquitin Chain Assembly Complex
MCU	Mitochondrial Calcium Uniporter
MFD	Minimum Feret's Diameter
mH_2O_2	Mitochondrial Hydrogen Peroxide
MHC	Myosin Heavy Chain
MLKL	Mixed-Lineage Kinase-Like Pseudokinase
MOMP	Mitochondrial Outer Membrane Pore
mPT	Mitochondrial Permeability Transition
mPTP	Mitochondrial Permeability Transition Pore
NAD^+	Nicotinamide Adenine Dinucleotide
NADH	Nicotinamide Adenine Dinucleotide + Hydrogen (Reduced Form)
NADPH	Nicotinamide Adenine Dinucleotide Phosphate
NCLX	$Na^+/Ca^{2+/}Li^+$ Exchange Channel
NF-Kβ	Nuclear Factor-Kappa Beta
NOX	NADPH Oxidases

O_2	Oxygen Molecule
$O_2^{\cdot -}$	Superoxide
OM	Outer Membrane
P	Phosphate Group
PCD	Programmed Cell Death
PDX	Patient-Derived Xenograft
Pi	Inorganic Phosphate,
PI	Phosphatidylinositol
PM	Plasma Membrane
pMLKL	Phosphorylated Mixed-Lineage Kinase-Like Pseudokinase
pRIPK1	Phosphorylated Receptor-Interacting Serine/Threonine Kinase 1
pRIPK3	Phosphorylated Receptor-Interacting Serine/Threonine Kinase 3
Quad	Quadriceps
RCD	Regulated Cell Death
RHIM	RIP Homotypic Interaction Motif
RIPK1	Receptor-Interacting Serine/Threonine Kinase 1
RIPK3	Receptor-Interacting Serine/Threonine Kinase 3
ROS	Reactive Oxygen Species
SOD	Superoxide Dismutase
Sol	Soleus
SS	Szeto-Schiller
SS-31	Szeto-Schiller 31, Elamipretide
T	TNF-A
TA	Tibialis Anteriod
tBID	Truncated BID
TNF-α	Tumor Necrosis Factor Alpha
TNFR	TNF-A Receptor
TPP	Triphenylphosphonium
TRADD	TNFR1-Associated Death Domain
TRAF2	TNFR-Associated Factor 2
Ub	Ubiquitin Moiety
UPS	Ubiquitin-Proteasome System
WG	White Gastrocnemius
Z	Z-VAD-FMK

CHAPTER 1. INTRODUCTION

Muscle mass is the most significant predictor of cancer survival[1]. Approximately 70% of individuals with cancer develop cancer cachexia, a syndrome characterized by an irreversible loss of muscle mass (atrophy) and often adipose tissue, that is irreversible with nutritional intervention [2]. Skeletal muscle atrophy in cancer patients correlates with heightened side effects to anti-cancer treatments at a given dose (greater dose-limiting toxicity), increased likelihood of treatment discontinuation, and prolonged hospital stays [2–6] . Furthermore, skeletal muscle atrophy is linked to lower survival rates following tumor resection surgeries, a higher likelihood of tumor recurrence, and diminished overall survival rates, contributing to nearly 30% of cancer-related fatalities globally [2,3,5,7]. Despite its prevalence and impact on individuals' lives, there is no established standard treatment for cachexia due to its multifaceted nature; the manifestation of muscle atrophy varies depending on tumor type, stage, and even sex differences [2,8]. For example, liver cancer has approximately an 80% likelihood of inducing cachexia, whereas kidney cancer has around a 30% chance[5]. Therefore, a comprehensive understanding of the molecular mechanisms governing muscle atrophy during cancer progression is crucial for developing effective treatment strategies.

Mitochondrial reactive oxygen species (mROS), a byproduct of ATP generation, have recently garnered significant attention as a potential mechanism for cancer-induced atrophy. This interest is driven by the discovery of heightened mitochondrial hydrogen peroxide (mH_2O_2), a form of ROS, in the skeletal muscle of cancer models[9–12]. For instance, in a Lewis Lung Carcinoma (LLC) model of cachexia, *Brown et al.* (2017) observed a twofold to threefold increase in mitochondrial ROS (specifically mH_2O_2) production in the plantaris muscle within 1-3 weeks post-tumor injection. Similarly, *Delfinis et al.* (2022) noted elevated mH_2O_2 production in the

quadriceps and diaphragm of C26 mice two weeks post-tumor injection. Some studies have sought to investigate the role of mROS in cancer-induced skeletal muscle atrophy by pharmacologically blockade of mROS[12–14]. These studies found that pharmacological inhibition of mROS alleviated skeletal muscle mass loss and overall body weight in cancerous mice, though not to the levels of healthy controls [12–14]. Nonetheless, the resulting preservation of muscle mass presents a promising avenue for skeletal muscle treatment during cancer progression. Additionally, existing literature, specifically the association between muscle atrophy and mROS raises the question of how mitochondrial ROS influences muscle atrophy during cancer progression.

Consequences of excessive mROS include aberrant protein turnover, where protein synthesis is downregulated and proteolysis is upregulated, and premature induction of regulated cell death pathways[15–18]. Cancer cachexia literature largely attributes the observed skeletal muscle atrophy to the former consequence of mROS: aberrant protein turnover. While this may hold true for several pre-clinical animal models of cachexia, muscle biopsies from human patients present a more nuanced picture[19–24]. In these human samples, protein synthesis (specifically the mTOR pathway) and proteolysis (specifically the ubiquitin-protease system) remain largely unchanged [12–14]. The divergent changes in protein synthesis and degradation between animal models and human patients highlight the need for pre-clinical models that better replicate the human phenotype. The orthotopic ovarian cancer model investigated by *Delfinis et al.* (2024) and *Ogilvie et al.* (2023) has been shown to replicate the human cachexia phenotype more closely, with skeletal muscle proteolytic pathways remaining unchanged. Furthermore, the absence of changes in protein synthesis and degradation suggests that alternative mechanisms, such as the latter consequence of excessive ROS—regulated cell death—may be driving cancer-induced atrophy at the muscle level.

Research in both human and animal models of cancer cachexia has underscored the role of regulated cell death (RCD) pathways, particularly apoptosis. The classical extrinsic apoptosis pathway is triggered by circulating cytokines, such as tumor necrosis factor-alpha (TNF-α), which has been shown to be elevated in both animal models and human cancer patients[25–28]. Apoptosis can also be induced intrinsically by mROS, elevated Ca^{2+} levels, and DNA damage. Intriguingly, both extrinsic and intrinsic apoptosis converge on the mitochondria, leading to the formation of the mitochondrial outer membrane pore (MOMP) the mitochondrial permeability transition pore (mPTP), respectively[18,25,29]. These pores allow proapoptotic proteins to leak from the mitochondria, forming the apoptosome and activating executioner caspases like caspase-3. This cascade ultimately results in cell shrinkage, chromatin condensation, and the generation of apoptotic bodies, which are then cleared by immune cells[25].

Significant research is required to confirm whether the sequence of events in skeletal muscle apoptosis aligns with canonical apoptotic pathways, as skeletal muscle cells are multinucleated and possess distinct clusters of mitochondria (intermyofibrillar vs. subsarcolemmal)[30]. Nonetheless, existing literature on apoptosis in skeletal muscle has demonstrated the activity of caspases, DNA fragmentation, mPT formation, and components of both MOMP and the apoptosome[31–34]. While the precise mechanisms governing apoptosis in muscle fibers remain elusive, the influential role of apoptosis in muscle atrophy models is evident. Additionally, markers of apoptosis have been shown to be elevated in muscle biopsies from patients with gastric, colorectal, and gastrointestinal cancers[35,36]. However, various models of muscle atrophy do not consistently exhibit increases in apoptosis, suggesting that atrophy might be regulated by alternative programmed cell death pathways yet to be identified.

Emerging evidence indicates the presence of a novel necroptosis pathway conserved across multiple cell types[37,38]. Circulating cytokines such as TNF-α induce necroptosis by autophosphorylating receptor-interacting serine/threonine kinase 1 (RIPK1), which subsequently binds and phosphorylates RIPK3, forming a functional 'necrosome'[25]. The necrosome phosphorylates mixed-lineage kinase domain-like (MLKL) pseudokinase monomers, leading to the formation of MLKL pores on the cell membrane[25]. This process results in the release of cytosolic contents and subsequent cell death. Recent literature suggests that the necrosome, through its interaction with the pyruvate dehydrogenase complex (PDC), can increase mROS production, specifically mH_2O_2[39]. Furthermore, mROS oxidizes and induces autophosphorylation of RIPK1, promoting further necrosome-mediated pore formation on the cell membrane, thereby accelerating necroptosis[40]. Additionally, while classical literature describes the induction of necroptosis starting with extracellular death signals, recent studies suggest that RIPK3 and subsequent steps of necroptosis can still occur in the absence of such signals[41,42]. The identification of these proteins in skeletal muscle, and their association with muscle diseases such as polymyositis and Duchenne muscular dystrophy, suggests necroptosis as an unexplored regulator of muscle cell death and cachexia[43–46]. Given the integral role of mROS in both apoptosis and necroptosis, pharmacologically mitigating mROS may elucidate whether either RCD pathway plays a significant role in cancer-induced atrophy.

The purpose of my MSc thesis is twofold: first, to investigate the involvement of mitochondrial ROS (mROS)-mediated regulated cell death (RCD) pathways, such as apoptosis and necroptosis, in the regulation of muscle atrophy during cancer progression; and second, to examine whether the reduction of mROS through a mitochondrial targeting antioxidant (SkQ1) prolongs the preservation of muscle mass in these mice. To achieve this, an orthotopic syngeneic

mouse model of epithelial ovarian cancer (EOC) cachexia was employed, assessing both pre-cachexia (40 days post-cancer induction) and cachexia stages (80 days post-cancer induction) and comparing them to PBS-injected sham mice. To address the second objective, half of the mice received the commercially available mROS inhibitor SkQ1 in their drinking water.

CHAPTER 2. LITERATURE REVIEW

2.1 CANCER CACHEXIA

2.1.1 Human Experience of Cachexia

Cachexia is a syndrome characterized by irreversible loss of muscle mass, often accompanied by a reduction in adipose tissue, that is not reversible with nutritional support[2]. The syndrome arises due to a combination of decreased food intake and abnormal metabolism[2]. Cachexia is comorbid to various diseases such as congestive heart failure, chronic pulmonary disease, AIDS, and cancer, the latter recognized as "cancer cachexia"[2]. This condition affects approximately 70% of cancer patients and contributes to 30% of cancer-related deaths worldwide [2]. Reduced muscle mass in cancer patients correlates with poor response to radiation and chemotherapy, early discontinuation of treatment, prolonged hospitalizations, and lower survival rates[3,5]. Moreover, individuals experiencing cancer cachexia often require assistance with daily activities like walking, bathing, and toilet use, and commonly report poor mental health[4].

Clinicians diagnose cachexia by assessing changes in food consumption, muscle mass and strength, typically evaluating changes in body weight and body mass index (BMI). However, researchers often use cross-sectional imaging techniques such as CT, MRI, and DEXA in human studies, as well as muscle cross-sectional area measurements in animal studies, for a more precise assessment skeletal muscle changes[2]. The progression of cachexia spans three stages: precachexia, cachexia, and refractory cachexia[2]. Precachexia entails weight loss equal to or less than 5% of body weight, accompanied by anorexia and metabolic alterations [2]. Cachexia involves weight loss exceeding 5% of body weight, reduced food intake, and systemic inflammation [2]. Refractory cachexia ensues after cachexia, usually when the tumor is unresponsive to anti-cancer treatments [2]. At this stage, individuals often have a life expectancy of less than 3 months [2]. There is no cure

or standard of care for cachectic individuals with physicians recommending multimodal treatments, including exercise and anti-inflammatory medication such as corticosteroids [2].

2.1.2 Models of Cachexia

There are several models utilised to study cancer cachexia, including both cell culture and animal models (fig.1). In vitro models allow direct manipulation of pathways involved in cancer cachexia, however these models fail to recapitulate the complexity of the tumor microenvironment. Thereby, rodent models of cancer better reflect the phenotypic and genetic heterogeneity of human cancer cachexia. Among animal models in rodents, there are allograft models, xenograft models, and genetically engineered models[47,48]. These models differ in many aspects, including rate of tumour development, location of tumour and technical difficulty of tumour inoculation. Most importantly, the ability of rodent models to recapitulate metastasis, the process of tumor cell migration from the primary site to the distant organs, differs based on the model. Thus, careful considerations must be made when choosing a rodent model to closely mimic human cancer cachexia.

Genetically engineered models commonly employ the use of loxP and Cre crossing to induce the overexpression of specific oncogenes in a tissue-specific manner[47]. Examples include the KPC model for pancreatic ductal adenocarcinoma and the Pik3ca mouse models for colorectal, lung, and ovarian cancers[47,49]. However, these models often lack human-like metastasis and commence tumour development from birth, a process not characteristic of human tumours, albeit more recent models like Pik3ca model show closer resemblance to human metastasis and cachexia[47]. A disadvantage of these models is that they are technically challenging compared to xenograft and allograft models explained in the following text.

Xenograft models involve injection of human tumours in immunodeficient rodents at their typical growth sites[47,48]. The pancreatic patient-derived xenograft (PDX) model is an extensively studied xenograft model that closely mirrors the pancreatic cancer cachexia seen in humans[47,48]. Despite their resemblance to human metastasis and neoplasm, the use of human xenograft models is limited by the availability of human tumour tissue. Additionally, the use of immunodeficient mice prevents investigation of tumour-host interactions, particularly the role of inflammation and the adaptive immune system which is recognized to contribute to many aspects of primary tumour growth and metastasis.

Allograft models, widely used for preclinical research, involve injecting rodent cancer cells into syngeneic rodents subcutaneously, intramuscularly, or intraperitoneally [47,48]. These models can be separated into ectopic models, where the tumor is injected at a site where it would not naturally develop, or orthotopic models, where the tumors grow at their natural growth site. Orthotopic models better replicate human cancers by enabling interactions with the tissue of origin. While allograft models are the least technically challenging model to induce, not all allograft models manifest the metastasis observed in corresponding human cancers. However, more recent models, such as an epithelial ovarian cancer (EOC) model, have successfully induced EOC orthotopically and showed metastasis akin to stage III EOC in humans[9,50].

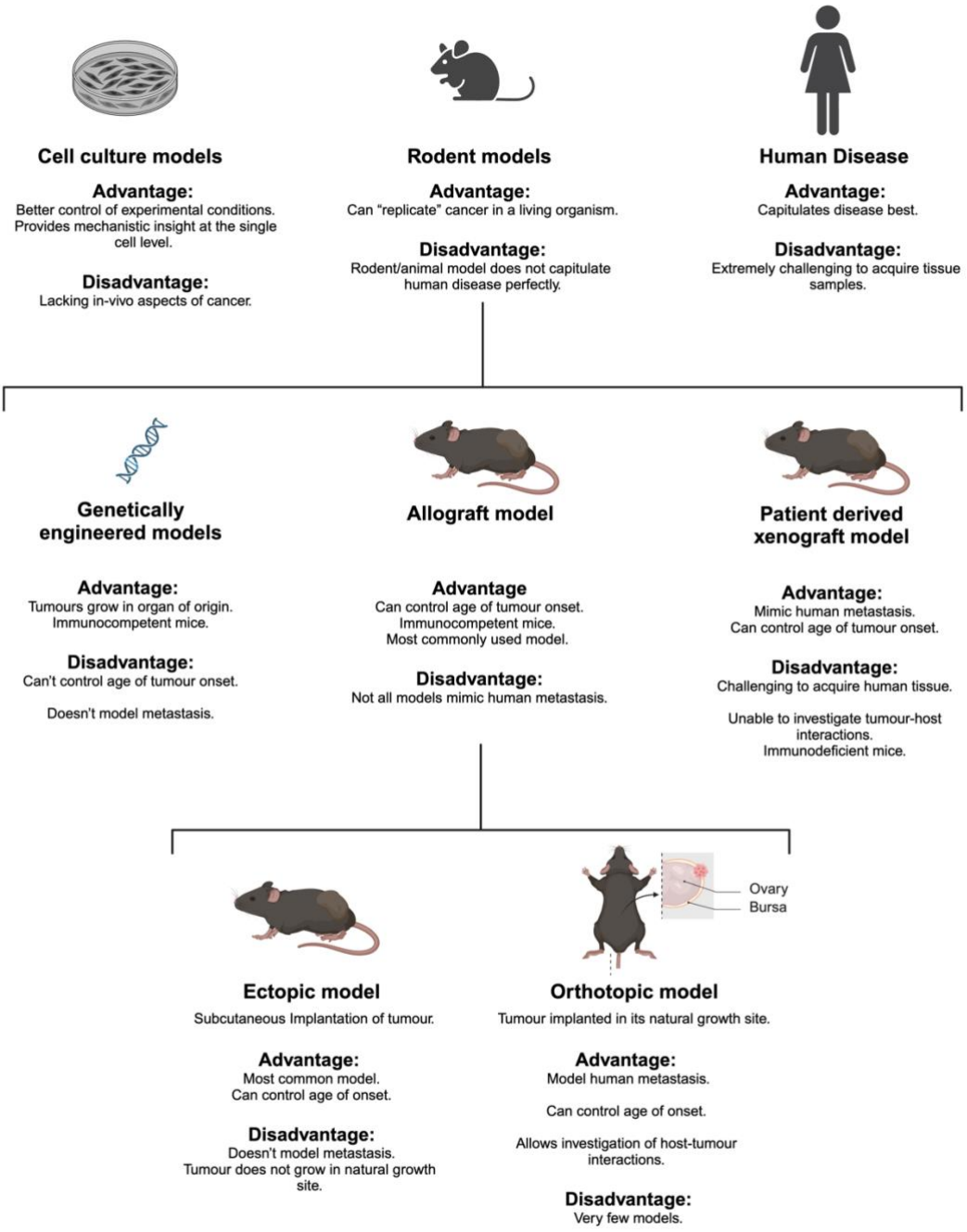

Figure 1.Flow chart illustrating the distinctions among various cancer cachexia models.

2.1.3 Advancements in Cancer Cachexia literature

Research into cancer-related cachexia has gained momentum in the past decade, with *Fearon et al.* (2011) establishing an international consensus on the definition of cachexia and a diagnostic framework. However, deciphering the precise mechanism of cachexia remains challenging due to its heterogeneity and multifaceted nature[8]. Cancer cachexia displays variability based on tumor type, location, and mass[5]. For instance, a person with liver cancer has an approximately 80% likelihood of developing cachexia, while someone with kidney cancer has around a 30% chance[5]. Additionally, even with similar tumor development, not all individuals will experience cachexia and these discrepancies are further pronounced when considering sex differences. Due to these variations among individuals, the direct cause of cachexia remains elusive.

Given its multifactorial nature, cachexia likely results from the coordinated action of multiple factors and pathways secreted by both the tumor and the host [8]. The association between circulating cytokines such as IL1B, IL4, IL6, IL8, IL10, IFNγ, and TNF-α and cancer cachexia has been extensively studied. These cytokines consistently appear elevated in both human and mouse models of cancer cachexia[26–28]. Additionally, skeletal muscle can produce cytokines, known as myokines[51]. However, while animal studies show varying changes in myokine mRNA transcript levels, human studies report these levels as largely unchanged[20,51,52]. Once at the muscle, circulating cytokines like TNF-α can relay information to myofibers, regulating anabolic and catabolic pathways. These cytokines can also instigate regulated cell death, a less-explored outcome in cachexia literature. Despite these insights, much work remains to identify the specific roles of cytokines and myokines in cancer-induced atrophy. For a more detailed review of cachexia mechanisms, refer to *Setiawan et al.* (2023) [53].

The literature on the mechanisms driving cancer cachexia at the skeletal muscle level has primarily focused on the dysregulation of anabolic (synthesis) and catabolic (proteolysis) protein pathways, leading to a net catabolic state[51]. Protein synthesis and degradation pathways are complex and interconnected, making it challenging to determine whether one or multiple pathways are activated during cancer progression or if the atrophy phenotype results from a coordinated effort by all pathways[51]. Much of the research on protein synthesis in cancer cachexia has concentrated on the mTOR pathway. Animal studies consistently show a decrease in protein synthesis via the mTOR pathway[19]. However, human studies present a more nuanced picture, with the mTOR pathway remaining unchanged or decreased in only one study[20,21]. These inter-species differences highlight the need for models that more closely mimic human cancer cachexia.

Protein catabolism or proteolysis is the breakdown of proteins into their amino acid components and occurs through four major pathways in skeletal muscle: the ubiquitin-proteasome system (UPS), the calpain pathway, apoptotic caspases, and the autophagy-lysosomal pathway[51]. The UPS has the largest body of literature supporting its occurrence in cancer cachexia. The UPS system involves the transfer of a ubiquitin chain from E1 (ubiquitin-activating enzymes) to E2 (ubiquitin-conjugating enzymes) to E3 (ubiquitin-ligase enzymes) and finally onto the protein to be degraded, effectively tagging the protein for proteolysis[51]. The 26S proteasome complex then recognizes the ubiquitin chain and breaks down the protein[51]. The activation of the UPS has largely been inferred from increased expression of E3 ligases in skeletal muscle, namely MuRF1 and MAFbx/Atrogin1[51]. Although these ligases appear ubiquitously expressed in animal models of cancer cachexia, they remain primarily unchanged in human cancer patients[19,22–24,54]. Thus, while the UPS system is enhanced in animal models, it may not play a significant role in human skeletal muscle atrophy, suggesting alternative pathways of muscle atrophy could be at play. Interestingly,

the novel orthotopic ovarian cancer model discussed in section 1.1.2 showed no changes in Atrogin and MuRF1 mRNA levels at 90 days with ovarian cancer (cachectic) compared to controls, more closely mimicking human cancer-induced atrophy[9]. For a more detailed review of protein catabolism, refer to *Martin et al.* (2023).

2.2 REGULATION OF MITOCHONDRIAL BIOENERGETICS

2.2.1 Introduction to Energy Transfer

All chemical reactions, including those occurring within our bodies every second, necessitate free energy. In humans, this vital 'energy' is harnessed from fuel molecules, primarily carbohydrates and fats acquired through our diets, and ultimately trapped within Adenosine triphosphate (ATP)[55].

Once in the cell, fuel molecules undergo many processes and transformations allowing the cell to extract all it necessitates from these molecules. Carbohydrates for example, are broken down into glucose molecules during digestion and are then delivered to cells via the bloodstream[55]. Once within the cells, glucose molecules undergo glycolysis, β-oxidation and the TCA cycle forming ATP molecules, NADH and $FADH_2$[55]. While ATP is formed during the aforementioned processes, electron carrier molecules nicotinamide adenine dinucleotide (NADH) and flavin adenine dinucleotide ($FADH_2$) carry electrons from one glucose molecule to the mitochondria and hold the means to generate much larger quantities of ATP.

2.2.2 Mitochondrial Morphology

In order to understand how mitochondria regulate bioenergetics in skeletal muscle cells, we must first be acquainted with the morphology mitochondria itself. Mitochondria contain a relatively permeable outer membrane (OM) that allows passage of most ions and molecules below 1000 daltons, and an impermeable inner membrane (IM) that only permits passage of specific

transporters and carriers (fig. 2a) [55]. The inner membrane is also laden with proteins facilitating the transfer of electrons from the carrier molecules NADH and $FADH_2$ to oxygen (O_2), together called the Electron transport chain (ETC), and ATP synthase[55]. The intermembrane space (IMS) is the space separating the inner and outer mitochondrial membranes and houses some key proteins such as cytochrome *c*[55]. Located at the centre of the mitochondria is the matrix, which contains proteins essential for various processes and mitochondrial DNA[55]. While different areas within mitochondria serve distinct functions, for ATP generation, the inner membrane and the IMS hold utmost significance.

A

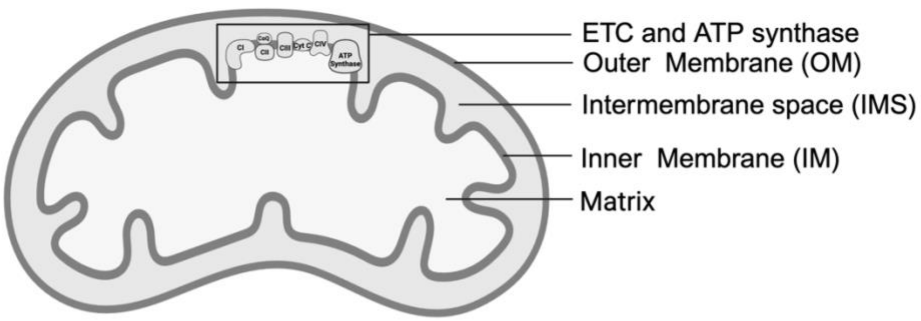
ETC and ATP synthase
Outer Membrane (OM)
Intermembrane space (IMS)
Inner Membrane (IM)
Matrix

B

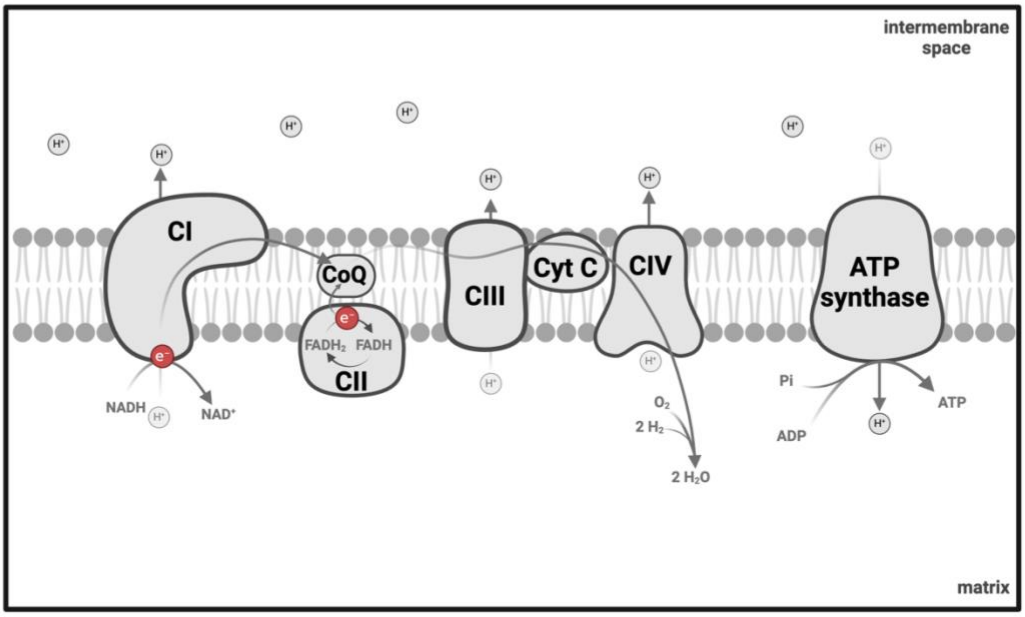
intermembrane space
CI
CoQ
CII
FADH2 FADH
CIII
Cyt C
CIV
ATP synthase
NADH
NAD+
O2
2 H2
2 H2O
Pi
ADP
ATP
matrix

C


ROS

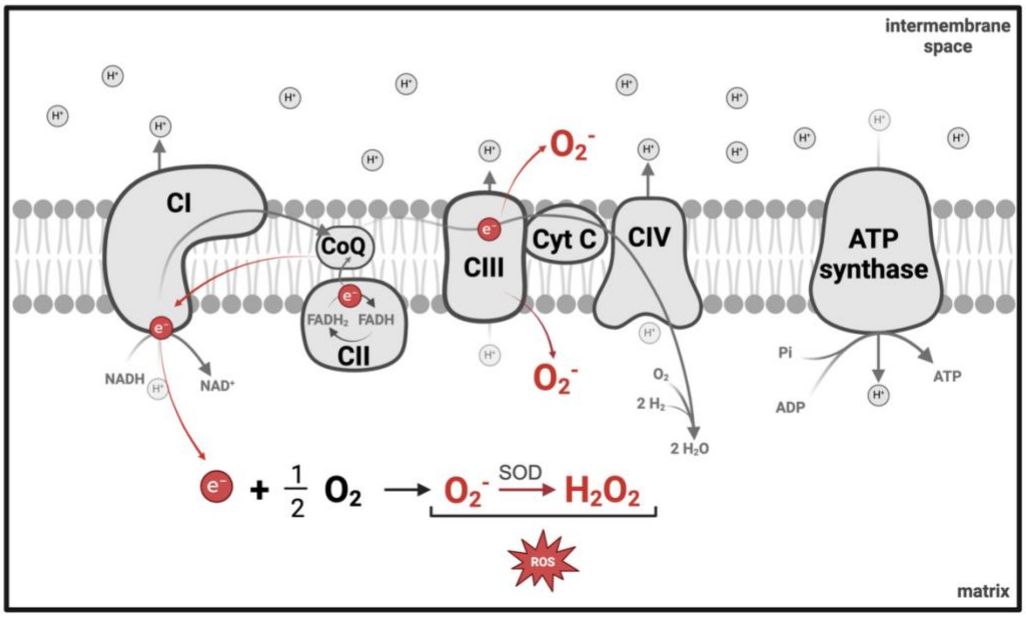
intermembrane space
CI
CoQ
CII
FADH2 FADH
CIII
Cyt C
CIV
ATP synthase
O2-
NADH
NAD+
O2
2 H2
2 H2O
Pi
ADP
ATP
e- + 1/2 O2 → O2- SOD → H2O2
ROS
matrix

Figure 2. Energy transfer and ROS generation in the mitochondria. A) Mitochondrial morphology. **B)** Energy transfer (via electrons) from NADH and $FADH_2$ to O_2. Electron flow through the ETC is coupled to proton pumping from the matrix to the intermembrane space. Protons in the intermembrane space drive ATP synthase to entrap energy within the bond between ADP and Pi, forming ATP. **C)** Sites of ROS generation at the inner mitochondrial membrane. $\mathbf{O_2^{\cdot-}}$ is catalyzed by superoxide dismutases (SOD) in the mitochondrial matrix and IMS, generating H_2O_2. **CI**: Complex I, **CII**: Complex II, **CIII**: Complex III, **CIV**: Complex IV, **CoQ**: Coenzyme Q, **Cyt C**: Cytochrome *c*, **NADH**: Nicotamide adenine dinucleotide, $\mathbf{FADH_2}$: Flavin adenine dinucleotide, $\mathbf{O_2}$: oxygen molecule, $\mathbf{H_2O}$: water molecule, **Pi**: inorganic phosphate, **ADP**: Adenosine diphosphate, **ATP**: Adenosine triphosphate, $\mathbf{H^+}$: proton, $\mathbf{e^-}$: electron, **ROS**: Reactive oxygen species. $\mathbf{O_2^{\cdot-}}$: Superoxide, $\mathbf{H_2O_2}$: Hydrogen peroxide, **SOD**: Superoxide dismutase. Information retrieved from [55,56].

1.2.3 Coupled Oxidative Phosphorylation

NADH and $FADH_2$ formed during glucose processing localise to the mitochondrial matrix. At the mitochondrial inner membrane, complex I and II extract electrons from NADH and $FADH_2$, respectively, leaving behind NAD^+ and FADH (fig. 2b)[55]. These extracted electrons subsequently travel through a series of proteins and carriers forming the electron transport chain (ETC): from complex I and II to coenzyme Q, then complex III, cytochrome *c*, complex IV and ultimately reaching an oxygen (O_2) molecule[55]. The union of an electron with O_2 allows O_2 to combine with two protons (H^+), generating a water molecule (H_2O)[55]. The free energy released during electron passage through the ETC facilitates the transfer of protons across the inner membrane[55]. Specifically, complexes I, III, and IV 'pump' protons from the matrix to the IMS[55,56]. Of note, electron transport through the ETC and proton pumping are coupled, one cannot occur without the other. As a result, the ETC establishes a substantial hydrogen concentration within the IMS compared to the mitochondrial matrix[55]. Thus, the ETC creates an electrochemical gradient across the inner membrane, with the mitochondrial matrix being relatively negatively charged, and the IMS positively charged[55]. The electrochemical gradient propels flow of protons through complex V, also known as ATP synthase, back to the cytosol[55]. ATP synthase harnesses energy released during the flow of protons to phosphorylate ADP, entrapping energy within phosphorylated ADP,

now ATP[55]. The flow of electrons through the ETC and ultimate reduction of an oxygen molecule, along with the generation of ATP by ATP synthase is known as ‘coupled’ oxidative phosphorylation or respiration[55].

2.2.4 Mitochondrial ROS Generation

Under healthy conditions, electron movement through the ETC, coupled with proton pumping, efficiently drives ATP synthase (fig.2c)[55]. However, elevated membrane potential, such that the proton concentration is much higher in the IMS exerts a backpressure on the system. Consequently, electrons ‘slip' and prematurely ‘leak’ from various ETC sites back into the matrix or to the IMS[56]. Previous literature has identified complexes I, III and in part complex II (through reverse-electron flow to complex I) as major sites for electron slip within the ETC[57]. Electrons slip off Complex I into the mitochondrial matrix, while electrons from complex III slip off into both the mitochondrial matrix and the IMS[56,57]. The prematurely slipped electron is accepted by free O_2 on the matrix or IMS side of the inner membrane, forming a superoxide radical ($O_2^{\cdot-}$), a type of ROS[56].

Within the cytosol and IMS, two $O_2^{\cdot-}$ radicals spontaneously dismutate, forming O_2 and hydrogen peroxide (H_2O_2)[56]. Additionally, superoxide is catalyzed by superoxide dismutases (SOD) in the mitochondrial matrix and IMS, generating H_2O_2. Subsequently, endogenous antioxidant systems, notably the peroxiredoxin-thioredoxin systems, act as ROS 'sinks,' clearing H_2O_2[56]. The functionality of these antioxidant systems is critical, as decreased efficiency or faulty catalysis may escalate ROS levels in subcellular compartments. At moderate rates of production and concentrations, ROS aid in cellular functions [56]. However, excessive ROS levels can alter redox states of cellular membranes and proteins, inducing cellular damage, unchecked cell proliferation, and premature cell death[56].

2.2.5 A Deeper Look into Superoxide ($O_2^{\cdot-}$) and Hydrogen Peroxide (H_2O_2)

As previously mentioned, premature electron slip from complexes I, II and III generate superoxide (fig. 2c)[56,57]. $O_2^{\cdot-}$ acts as a free radical due to its unpaired electron, exhibiting high reactivity as both a reducing and oxidizing agent[56]. Additionally, $O_2^{\cdot-}$ readily donates its unpaired electron or accepts another electron and two proton atoms (H^+), forming H_2O_2[56]. In contrast to $O_2^{\cdot-}$, H_2O_2 is more stable and possesses a longer half-life, making it an effective signaling molecule[56]. H_2O_2 is also uncharged, enabling its passage across the mitochondrial membranes and into the cytosol[56]. H_2O_2 acts primarily as a strong oxidizing agent, readily extracting electrons[56]. Additionally, H_2O_2 interacts with proteins that contain cysteine thiolates to form a sulfenate, which in itself can alter protein function or trigger subsequent inter or intramolecular reactions, such as disulfide formation[56]. While ROS specifically affect proteins with thiolate groups, they do not target specific proteins directly. Instead, ROS will oxidize or reduce any nearby cysteine-containing proteins indiscriminately. Furthermore, cells manage ROS activity through the precise positioning of ROS generators and buffers, which controls where oxidation and reduction occur[56]. This spatial regulation allows certain areas within a cell to be more oxidized or reduced than others.

2.2.6 Calcium Handling

Apart from energy transfer to ATP and ROS production, mitochondria are also responsible for calcium (Ca^{2+}) handling. While the sarcoplasmic reticulum is primarily responsible for Ca^{2+} uptake in muscle cells, mitochondria can also uptake Ca^{2+}, particularly during cytosolic Ca^{2+} overload[58]. The influx of Ca^{2+} into mitochondria is mainly facilitated by the mitochondrial calcium uniporter (MCU), while calcium efflux is predominantly managed by the $Na^+/Ca^{2+/}Li^+$ (NCLX) exchange channel[58]. These channels collectively modulate mitochondrial free Ca^{2+} concentrations.

Under normal physiological conditions, Ca^{2+} uptake is relatively small, and the NCLX maintains mitochondrial calcium levels. However, in instances of excessive mitochondrial free Ca^{2+}, the NCLX fails to expel Ca^{2+} as rapidly as it is absorbed[58]. This discrepancy between the rates of Ca^{2+} influx and efflux can potentially result in mitochondrial Ca^{2+} overload. Ca^{2+} overload in the mitochondria ultimately disrupts mitochondrial function by impairing ATP production and amplifying ROS generation. To prevent these unfavorable outcomes, mitochondria expel Ca^{2+} through transient opening of mitochondrial permeability transition pore (mPTP) in addition to the NCLX[58,59]. The mPTP is a non-selective channel in the inner mitochondrial membrane that allows solutes smaller than 1.5 kDa to pass through in a process called mitochondrial permeability transition (mPT). Although the precise composition of the mPTP remains uncertain, compelling evidence suggests that ATP synthase, the adenine nucleotide translocase (ANT), and the matrix protein cyclophilin D either directly constitute the pore or regulate its formation[59]. Additionally, when there is excessive mROS emission, the mPTP can undergo prolonged mitochondrial permeability transition (mPT) which is a catastrophic event that ultimately leads to cell death.

The mPTP is a non-selective channel in the inner mitochondrial membrane that allows solutes smaller than 1.5 kDa to pass through in a process called mitochondrial permeability transition (mPT) [59]. Although the precise composition of the mPTP remains uncertain, compelling evidence suggests that ATP synthase, adenine nucleotide translocase (ANT), and the matrix protein cyclophilin D either directly constitute the pore or regulate its formation[29]. Additionally, excessive mROS emission can cause the mPTP to undergo prolonged mitochondrial permeability transition (mPT), a catastrophic event that ultimately leads to apoptosis (section 1.3.5, fig. 3)[29].

2.2.7 The Roles Of mPTP And MOMP In Cell Death Mechanisms

Under normal circumstances, transient mPT functions as a protective mechanism to alleviate excessive calcium accumulation. However, prolonged mPT leads to matrix space swelling, causing the inner mitochondrial membrane surface area to surpass that of the outer mitochondrial membrane[60,61]. This overextension ultimately results in the rupturing of the outer mitochondrial membrane, enabling intermembrane space proteins, such as cytochrome *c* to escape to the cytosol [60,61]. This event triggers the formation of the apoptosome, initiating the apoptotic pathway[61].

The mPTP isn't the sole pore responsible for releasing cytochrome *c* into the cytosol and triggering apoptosis. Traditionally, the mitochondrial outer membrane pore (MOMP) was considered the initiator of cytochrome *c* release[61]. Unlike mPTP, which can trigger apoptosis due to high mitochondrial ROS and Ca^{2+} concentrations, MOMP activation relies on pro-apoptotic Bcl-2 family members like BAX and tBID that are outside of the mitochondria[61]. The precise mechanism by which these pro-apoptotic proteins induce MOMP formation remains unclear; however, their activity ultimately leads to the release of cytochrome *c* from the IMS, formation of the apoptosome, activation of caspase-3 and subsequent apoptosis (discussed in chapter 1.3.4, fig. 3).

2.2.8 Mitochondrial targeting antioxidants

In resting myoblasts, approximately 45% of net cellular H_2O_2 is produced at mitochondrial electron transport chain (ETC) sites, while cytosolic NADPH oxidases (NOX) contribute about 40%, and enzymatic sources account for the rest[56]. This substantial H_2O_2 generation by mitochondria, coupled with their involvement in numerous pathologies, has led to the development of therapeutics specifically targeted to mitochondria. As previously mentioned, the IMM maintains

a membrane potential, creating a relatively negative charge in the mitochondrial matrix compared to other subcellular compartments. This characteristic has been exploited by many mitochondrial-targeting antioxidants to target and accumulate within the mitochondria. Mitochondrial antioxidants can be classified into two categories: lipophilic cation-linked and peptide-based mitochondrial antioxidants[62].

Peptide-based antioxidants are usually linked to small positively charged peptides known as Szeto-Schiller (SS)-peptides[62]. These SS-peptides incorporate four alternating aromatic/basic amino acids that offer essential hydrophobicity and positive charge at physiological pH, facilitating their infiltration across membranes and targeting towards the mitochondria[62]. Among these antioxidants, SS-31, also known as elamipretide, is the most commonly used. SS-31 contains dimethyl tyrosine residues that interact with oxygen radicals, converting them into unreactive tyrosine radicals[62]. Moreover, SS-31 accumulates on the inner mitochondrial membrane, safeguarding and restoring mitochondrial structure, fostering ATP synthesis, diminishing electron leakage and cardiolipin peroxidation[62,63].

Lipophilic cation-linked mitochondrial-targeting antioxidants consist of a lipophilic cation and a large hydrophobic chain. The lipophilic cation, typically triphenylphosphonium (TPP), which acts as a 'magnet' for the negatively charged mitochondrial matrix[62]. The positive charge of the cation is spread over a considerable surface area, allowing it to move freely across membranes and direct itself toward the negatively charged mitochondrial matrix[62]. One well-known antioxidant in this category is mitoQ, composed of a ubiquinone moiety (anti-oxidant) linked to a TPP moiety by a 10-carbon alkyl chain[62]. SkQ1, a newer antioxidant with a structure similar to MitoQ, consists of plastoquinone conjugated to TPP by a 10-carbon chain[62]. Plastoquinone is derived from plant chloroplasts and has shown to possess stronger antioxidant

properties. Both MitoQ and SkQ1 sit in the inner mitochondrial membrane and prevent the formation of superoxide by scavenging leaking electrons from complex I and III[62,64]. Literature on both MitoQ and SkQ1 have established that both anti-oxidants prevent tumorigenesis, tumour growth and metastasis in some cancers such as rhabdomyosarcoma[65,66]. At low doses, both act as antioxidants; however, at high concentrations, they are pro-oxidant, potentially leading to toxicity[62]. However, SkQ1 demonstrates lower pro-oxidant activity than MitoQ, making it a safer option for prolonged use.

2.2.9 Mitochondria in Cancer Cachexia

Given the significant role mitochondria play within cells, their involvement in cancer cachexia is not surprising. While mitochondrial bioenergetics have not been extensively explored in cachexia studies, the limited research conducted has revealed increased ROS generation during early stages of tumour progression. For instance, in an LLC model of cachexia, *Brown et al.* (2017) discovered a twofold to threefold elevation in mH_2O_2 in the plantaris muscle 1-3 weeks post tumor inoculation. Similarly, *Delfinis et al.* (2022) observed heightened mitochondrial H_2O_2 production 2 weeks post tumour-inoculation in quadriceps and diaphragm of C26 mice. It is worth mentioning that both studies assessed complex I ROS emission. Thus, changes in ROS emission from the pyruvate dehydrogenase complex, complex II and III is yet to be determined.

Although increased mROS generation in skeletal muscle of cachectic mice is evident, whether enhanced mROS generation favours muscle loss remains uncertain. To date, few studies have attempted to address this question. *Brown et al.* (2020) induced the LLC model in SOD1 knockout mice, rendering the mice unable to convert $O_2^{\cdot -}$ radicals to H_2O_2. SOD1 knockout mice with LLC did not exhibit exacerbated cachexia compared to controls (no significant differences in muscle mass compared to controls). However, this outcome might be attributed to SOD1 being a

cytosolic dismutase that regulates cytosolic $O_2^{\cdot-}$ rather than mitochondrial[67]. Consequently, the question persists: does heightened mROS production in skeletal muscle during cancer-induced cachexia have a beneficial or detrimental effect on muscle mass?

Additionally, cancer-cachexia studies using mitochondrial therapeutics (SS-31 and MitoQ) have shown improved hind-limb skeletal muscle mass, albeit improvements did not reach wild-type levels[12–14]. Of the three cachexia studies using mitochondrial-specific antioxidants, only one measured mROS emission. In a C26 model, *Smuder et al.* (2020) showed mH_2O_2 production in the absence of substrates and ADP (basal, state I) decreased to wild-type concentrations with SS-31 in the diaphragm, and diaphragm CSA was completely rescued 4 weeks post-tumor inoculation. However, these results contradict *Delfinis et al.* (2022) who saw no changes in pyruvate-malate (state II)-stimulated and ADP-supported (state III) mH_2O_2 emission 4-weeks post C26 tumor inoculation. The discrepancy between these two studies may be because they assessed different types of mROS emission (state I vs. state II and III). This highlights the need to assess all plausible sources of ROS in the skeletal muscle of cachectic mice.

Mitochondrial ROS emission in skeletal muscle of cancer patients has not been investigated directly, however, indirect evidence of oxidative stress is apparent. *Puig-Vilanova et al.* (2015) observed increased protein carbonylation and lipid peroxidation in the skeletal muscle of lung cancer patients. These findings indicate elevated overall ROS within the myofiber, though not specifically from mitochondrial ROS. Nonetheless, given that mitochondria are major contributors to ROS in myofibers, it is likely that mitochondrial ROS contributed to the observed protein carbonylation and lipid peroxidation.

Table 1. Comprehensive Summary of original research studies measuring mitochondrial ROS in skeletal muscle of cancer cachexia models. These studies were sourced from PubMed using the keywords "ROS" and "cancer cachexia".

Study	Model (human, rodent, cell culture)?	Type of cancer	Tissue	ROS measured?	ROS increased or decreased?	Intervention?	Effect of intervention?
Delfinis et al. (2022)	mouse	Colorectal C26	quadriceps	yes	↑ at 4 weeks	n/a	n/a
			diaphragm	yes	↑ at 2 weeks		
Delfinis et al. (2024)	mouse	Epithelial Ovarian Cancer	TA	yes	↑ at 90 days	n/a	n/a
			diaphragm	yes	=		
Brown et al. (2017)	mouse	lewis lung carcinoma	plantaris	yes	↑	no	n/a
Halle et al. (2019)	mouse	colorectal C26	quadriceps	yes	↓	n/a	n/a
Ballaro et al. (2021)	mouse	colorectal C26	hindlimb skeletal muscle	no	n/a	SS-31	Skeletal muscle mass and body-weight improved albeit not to control levels.
Pin, Huot and Bonetto (2022)	mouse	colorectal C26	hindlimb skeletal muscle	no	n/a	MitoQ	MitoQ ameliorated skeletal muscle mass in C26 mice albeit not to healthy levels.
Smuder et al. (2020)	mouse	colorectal C26	diaphragm	yes	↑	SS-31	ROS decreased by SS-31, atrophy rescued.
Brown et al. (2020)	mouse	lewis lung carcinoma	red gastrocnemius	yes	=	SOD1 KO	Cachexia not exacerbated.

2.3 REGULATED CELL DEATH

2.3.1 Introduction to Regulated Cell Death

Cell death is an inevitable facet of life, yet it serves as a crucial protective mechanism for the entire organism. Regulated cell death (RCD), is cell death that relies on dedicated molecular

machinery, allowing for potential modulation through pharmacological or genetic interventions[25]. RCD manifests in two main forms: programmed cell death (PCD) for regular cellular turnover, or as a response to disruptions in the intracellular or extracellular environment. In instances of prolonged stress, cells might undergo RCD to eliminate non-functional or potentially harmful cells, or to release signaling molecules that alert nearby cells or the organism of potential threats[25]. Various forms of RCD have been identified to date, including apoptosis, necroptosis, and ferroptosis. This literature review will focus on the classical Tumor Necrosis Factor- alpha (TNF-α) induced apoptosis and necroptosis pathways that are ubiquitous to many cell types. A more comprehensive review can be found in *Galluzzi et al.* (2018).

2.3.2 TNF- α Mediated Signalling in Cell Death

TNF-α is a small soluble protein that triggers cellular responses upon binding to Tumor Necrosis Factor (TNF) receptors, TNFR1 or TNFR2[68]. While TNFR1 is ubiquitously expressed in human cells, TNFR2 is predominantly found in immune cells, neurons, and endothelial cells [68,69]. In skeletal muscle, TNF-α acts as a ligand and specifically binds to TNFR1, initiating an intracellular response. TNFR1, located in the plasma membrane, contains a death domain (DD) enabling the recruitment of TNFR1-associated death domain (TRADD) and receptor-interacting serine/threonine-protein kinase 1 (RIPK1), together forming complex I[68,69]. This complex triggers cell survival signalling via the nuclear factor-kappa β (NF-Kβ) pathway. However, when a cell is under stress, TNFR1 signaling leads to the formation of complex IIa, IIb, and IIc (fig. 3)[25].

Once recruited to the TNFR1-TRADD complex, RIPK1 undergoes various post-translational modifications dictating the cell's fate[25,70]. Initially, TRADD ubiquitinates lysine 63 (K63) on RIPK1. This K63 ubiquitination recruits TNFR-associated factor 2 (TRAF2) and RING finger E3 ligase cellular inhibitor of apoptosis protein-1 and 2 (cIAP1/2), further promoting K63

ubiquitination of RIPK1[25,70]. Additionally, recruitment of the linear ubiquitin chain assembly complex (LUBAC) induces linear M1 polyubiquitination of RIPK1, completing the formation of complex I [25,70]. The ubiquitination status of RIPK1 determines whether the cell will survive (via complex I), undergo apoptosis (via complex IIa and IIb), or undergo necroptosis (via complex IIc) [25,70]. Ubiquitination of RIPK1 at K63 facilitates the recruitment of proteins involved in the NF-Kβ pathway, ultimately increasing the expression of anti-apoptotic proteins. Thus, if RIPK1 loses its protective ubiquitin chains, it dissociates from complex I (with or without TRADD) and assembles one of the three forms of complex II based on intracellular conditions [25,70].

Following NF-Kβ activation, cellular FLICE-like inhibitory protein long (cFLIP-L) prevents interaction of procaspase-8 with complex IIa [25,70]. In the absence or reduced activation of NF-Kβ, cFLIP-L levels decrease, leading to the formation of complex IIa, consisting of TRADD, FAS-associated death domain (FADD), and pro-caspase-8 [25,70]. Complex IIa triggers the autocleavage of procaspase-8 into its active form, caspase 8, initiating apoptosis (fig. 3).

In the absence of TRADD, de-ubiquitinated RIPK1 forms complex IIb, comprising FADD, procaspase-8, RIPK1, and RIPK3[70]. Formation of complex IIb also results in procaspase-8 autocleavage and apoptosis. Caspase-8 in complex IIb cleaves RIPK1 and RIPK3, further committing the cell to apoptosis (fig. 3).

Occasionally, under conditions of high cellular reactive oxygen species (ROS), FADD, cFLIP, procaspase-8, de-ubiquitinated RIPK1, and RIPK3 form complex IIc, also known as the 'necrosome,' committing the cell to an alternative regulated cell death (RCD) pathway known as necroptosis (fig. 3) [25,70].

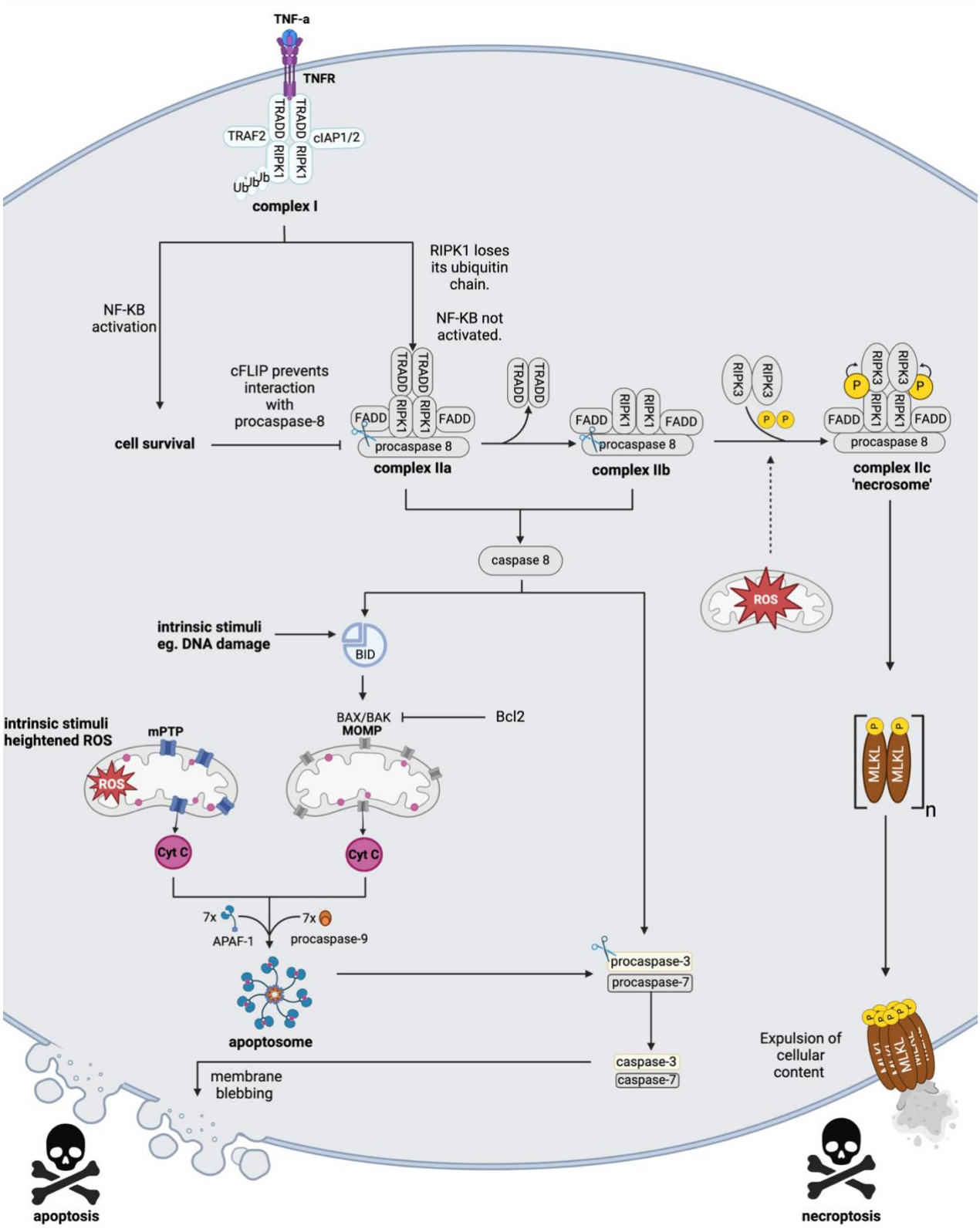
TNF-a
TNFR
TRADD
TRADD
TRAF2
cIAP1/2
RIPK1
RIPK1
Ub
complex I
NF-KB activation
RIPK1 loses its ubiquitin chain.
NF-KB not activated.
cFLIP prevents interaction with procaspase-8
cell survival
FADD
FADD
procaspase 8
complex IIa
complex IIb
RIPK3
RIPK3
P
complex IIc 'necrosome'
caspase 8
ROS
intrinsic stimuli eg. DNA damage
BID
BAX/BAK MOMP
Bcl2
intrinsic stimuli heightened ROS
mPTP
Cyt C
7x
APAF-1
procaspase-9
apoptosome
procaspase-3
procaspase-7
caspase-3
caspase-7
membrane blebbing
MLKL
n
Expulsion of cellular content
apoptosis
necroptosis

Figure 3. TNF-α induced apoptosis and necroptosis. TNF-α binding to its recepter TNFR induces complex I formation. When RIPK1 in complex I loses its protective ubiquitin chain, complex I progresses into either complex IIa, IIb and IIc depending on cellular conditions. When the NF-KB pathway is not activated and cFLIP levels are low, procaspase-8 is cleaved in complex IIa. In the absence of TRADD, procaspase-8 can also be cleaved. In instances of elevated RIPK3 expression and mitochondrial ROS, formation of complex IIc (necrosome) is favoured. Cleaved caspase-8 can cleave and activate executioner caspases-3 and -7 or cleave BID, leaving tBID which in conjuncture with BAX and BAK can induce MOMP. Heightened mitochondrial ROS can also trigger prolonged mPTP formation. Both MOMP and mPTP allow release of pro-apoptotic proteins like cytochrome *c* from the mitochondria. In the cytosol, Cytochrome *c* along with APAF-1 and procaspase-9 form the heptameric apoptosome. The apoptosome cleaves and activates caspases-3 and -7 which then cleave other cellular protein and fragment DNA, ultimately leading to membrane blebbing and cell death (apoptosis). On the other hand, complex IIc formation leads to MLKL phosphorylation and subsequent oligomerization on the cellular plasma membrane. MLKL oligomers permeabilize the membrane allowing cellular content to leak out of the cell, subsequently the cell dies. **APAF-1:** Apoptotic protease activating factor 1, **BAK:** Bcl-2 antagonist/killer, **BAX:** BCL-2 associated X, **Bcl-2:** B-cell lymphoma-2 anti-apoptotic protein, **BID:** BH3 interacting-domain death agonist, **cFLIP:** cellular FLICE-like inhibitory protein, **cIAP1/2:** Cellular inhibitor of apoptosis protein-1 and 2, **Cyt *c*:** Cytochrome *c*, **FADD:** FAS-associated death domain, **MLKL:** Mixed-Lineage Kinase-Like Pseudokinase , **MOMP:** Mitochondrial Outer Membrane Pore, **mPTP:** mitochondrial Permeability Transition Pore, **NF-KB:** Nuclear factor-kappa beta, **P:** Phosphate group, **RIPK1:** receptor-interacting serine/threonine kinase 1, **RIPK3:** receptor-interacting serine/threonine kinase 3, **ROS:** Reactive Oxygen Species, **tBID:** truncated BID , **TNF-α:** Tumor Necrosis Factor alpha, **TNFR:** TNF-a Receptor, **TRADD:** TNFR1-associated death domain, **TRAF2:** TNFR-associated factor 2, **Ub:** Ubiquitin moiety. Information retrieved from [25,59,70].

2.3.3 Apoptosis

Apoptosis, derived from the Greek term meaning "to fall off" (as leaves fall from a tree), is a form of programmed cell death (PCD) that occurs under physiological conditions to facilitate regular cellular turnover[71]. This process enables cells that fail to pass specific checkpoints to upregulate essential proteins and self-initiate their death, effectively allowing these cells to "fall off" from the organism as the Greek term implies. Apoptosis functions as a regulated cell death pathway, activated not only during regular cellular turnover but also in response to perturbations in the extracellular and intracellular environments. Perturbations including extracellular cell death

signals (e.g. TNF-α), viral invasion, DNA damage, and heightened ROS emission can trigger either the extrinsic or intrinsic apoptotic cascades[25].

Apoptosis relies on a family of cysteine proteases called caspases. These enzymes are synthesized as inactive precursors, known as procaspases, which consist of three parts: a prodomain that facilitates protein interactions, a p20 subunit housing the catalytic cysteine-histidine dyad, and a p10 subunit contributing to substrate specificity[72]. Caspases are categorized into two classes: initiators, like caspase-8 and -9, and executioners, such as caspases-3, and -7. Depending on the apoptotic pathway activated (intrinsic vs extrinsic), different sets of caspases are involved. However, both cascades consist of several mechanisms that ultimately converge at the mitochondria[25]. Ultimately, these mechanisms ensure the efficient removal of non-functional or harmful cells, thereby maintaining the health and stability of the organism.

2.3.4 Extrinsic Apoptosis

Under specific cellular conditions, interaction of TNF-α interaction with its receptor triggers the formation of complex IIa and IIb. Both complexes catalyze the autocleavage of procaspase-8 into its active form, caspase-8 (fig.3)[25]. Once activated, caspase-8 targets aspartic acid residues at the junctions between the prodomain, p20, and p10 subunits of executioner procaspase-3[19]. Consequently, two p20 and p10 subunits assemble non-covalently, resulting in the active executioner caspase-3[19]. Caspase 3 then cleaves and activates procaspase-9[19]. Executioner caspases cleave multiple structural and signalling proteins rendering them dysfunctional and bring about the apoptotic phenotype.

The connection between active caspase 8 and mitochondria, associating external triggers with mitochondria to initiate apoptosis, depends on the B-cell lymphoma (Bcl-2) family of proteins. Intrinsic signals, like DNA damage, also converge with mitochondria with the assistance

of Bcl-2 proteins[73]. Bcl-2 family members possess up to four conserved Bcl-2 homology (BH) domains (BH1, BH2, BH3, and BH4) and can assume either pro-apoptotic or anti-apoptotic roles[73]. A specific subset of Bcl-2 proteins, known as BH3-only proteins, such as BH3 interacting-domain death agonist (BID), function as intracellular death ligands[73]. During extrinsic apoptosis, caspase-8 cleaves BID, leaving a truncated form (tBID) that prompts the accumulation of BCL-2 associated X (BAX) apoptosis regulator and Bcl-2 antagonist/killer (BAK) on the mitochondrial outer membrane by mechanisms that are currently not fully understood[18,59,74,75]. Subsequently, BAX and BAK form oligomers, and permeabilize the mitochondrial outer membrane forming the mitochondrial outer membrane permeability pore (MOMP)[18]. This event triggers the release of intermembrane space proteins such as cytochrome *c* to the cytosol. Once mitochondria undergo MOMP, the cell is committed to death, representing a critical 'point of no return' checkpoint in apoptosis (fig.3)[59].

The pro-survival Bcl-2 family proteins prevent the formation of MOMP by directly inhibiting the oligomerization of BAX and BAK on the mitochondria, indirectly sequestering BH3-only activators, and facilitating the retro-translocation of BAX and BAK from the mitochondria to the cytosol, thereby limiting their accumulation on the mitochondria[73,76]. Thus, an elevated BAX to Bcl-2 protein ratio indicates a cells susceptibility to MOMP. As mentioned in the previous section, stimuli intrinsic to the mitochondria, high ROS and Ca^{2+} concentrations, can also induce mitochondrial membrane permeabilization (through mPTP), cytochrome *c* release and subsequent apoptosis[18,59]. However, the mPTP spans both the inner and outer mitochondrial membrane unlike MOMP which spans only the outer membrane (fig.3).

2.3.5 Intrinsic Apoptosis

Intrinsic apoptosis can be triggered from a host of intracellular insults such as nuclear DNA damage and enhanced mROS emission. Similar to extrinsic apoptosis, the 'point of no return' for apoptotic cells is the formation of MOMP or prolonged formation of mPT[59]. Both MOMP and mPT allow release of pro-apoptogenic proteins that normally reside in the mitochondria to the cytosol, thereby triggering a cascade of events that leads to the cells' demise [18,59,74,75]. One such pro-apoptogenic protein is cytochrome *c*, which is known for its role in the electron transport chain.

Upon its release from the mitochondria, cytochrome *c* associates with cytoplasmic apoptotic peptidase activating factor 1 (APAF1) monomers and procaspase-9, assembling a heptameric structure known as the "apoptosome" [18,59,74,75]. Once the apoptosome is established, apoptotic protease activating factor 1 (APAF-1) facilitates the dimerization of procaspase-9 and its autocleavage into caspase-9[41] [77,78]. Active caspase-9 dimers proceed to cleave executioner caspases like procaspases-3 and 7 [18,77,78]. Subsequently, executioner caspases cleave crucial structural proteins and enzymes, ultimately driving the cell towards death. This ultimately leads to cell shrinkage, chromatic condensation, formation of cytoplasmic blisters and apoptotic bodies (fig.3).

2.3.6 Apoptosis in Muscle

Apoptosis has also been observed in skeletal muscle fibers. However, whether apoptosis in muscle follows the classical pathways outlined in the previous sections remains uncertain. Several considerations must be taken into account when assessing apoptosis in skeletal muscle. First, mature skeletal muscle fibers are long and multinucleated. Certain studies suggest that individual myonuclei, rather than the entire myofibers, undergo apoptosis[30]. This process could

lead to reduced protein expression within a fiber, potentially causing atrophy but not complete myofiber cell death[30]. The debate persists regarding whether whole muscle fibers or individual myonuclei are subject to apoptosis, and relatively limited research has been conducted on this topic.

Second, mitochondrial content varies between myofibers. Slow-twitch fibers, like those in the soleus, have more mitochondria than fast-twitch fibers, such as those in the plantaris[79]. Given the integral role of mitochondria in both intrinsic and extrinsic apoptosis, the quantity of mitochondria in tissues may influence the susceptibility of the muscle to apoptosis. For example, comparisons between the red (primarily slow-twitch) and white (primarily fast-twitch) portions of the gastrocnemius in rats have shown differences in AIF and cytochrome *c* release[31]. This suggests that differences in mitochondrial content between muscles and fibers may influence apoptotic signaling.

Despite these special considerations, evidence indicates that apoptotic markers play a role in regulating muscle atrophy. Studies have demonstrated that inducing the mitochondrial permeability transition pore (mPTP) in single fibers of mouse flexor digitorum brevis (FDB) muscles can increase mitochondrial ROS (mROS) and caspase-3 activity, resulting in a reduction in muscle fiber diameter[33]. Moreover, research has shown that caspase-3 can cleave muscle contractile proteins in both L6 muscle cell cultures and psoas muscle[80].

Apoptosis has also been observed in human and animal models of cachexia (Table 2). Muscle biopsies from colorectal cancer patients revealed a threefold increase in myofiber DNA fragmentation, chromatin condensation, elevated levels of caspase-8 and -9, and the presence of apoptotic bodies[35,36]. In $Apc^{min/+}$ mice, a model of spontaneous intestinal and colon cancer, heightened expression of proapoptotic markers (BAX mRNA and protein, APAF-1 protein) was

observed in both the red and white portions of the gastrocnemius and soleus muscles in cachectic mice[81]. Caspase 3, 8 and 9 activity have also been elevated two-fold in MAC16 tumour bearing mice[82]. *Wang et al.* (2015) also found higher protein content of caspase-3 and BAX in C26 colorectal cancer mice compared to controls. Further, *Wang et al.* (2015) treated C26 mice with z-VAD-FMK, a pan-caspase inhibitor and found that atrophy was alleviated albeit not to control levels. While the precise mechanism governing apoptosis in muscle fibers remains elusive, the influential role of apoptosis in cancer-induced muscle atrophy is evident.

Table 2. Summary of original literature on apoptosis within skeletal muscle in cancer cachexia models. The literature was identified through PubMed (U.S National Library of Medicine) using keywords "apoptosis" and "cancer cachexia".

Study	Model (human, rodent, cell culture)?	Type of cancer	Tissue	Apoptotic Markers Measured	Effect of cancer on apoptotic markers?
de Castro et al. (2019)	human	gastric and colorectal cancer	rectus abdominis	caspase 8, caspase 9 cleavage	⬆
Busquets et al. (2007)	human	gastro-intestinal cancer	rectus abdominis	DNA fragmentation	⬆
Belizario, Lorite and Tisdale (2001)	mouse	MAC16 PDX	gastrocnemius	caspase 3,8 and 9 activity	⬆
Baltgalvis et al. (2010)	mouse	intestinal and colon cancer	gastrocnemius	BAX and APAF1 protein contetnt. BAX mRNA	⬆
Wang et al. (2015)	mouse	C26 colorectal	gastrocnemius	BAX and BCL-2 mRNA, caspase 3 mRNA. BAX, BCL-2 caspase 3 protein content	⬆

2.3.7 Necroptosis

Necroptosis is a recently discovered RCD pathway that operates independently and in the absence of apoptosis. When RIPK1 loses its protective ubiquitin chain, it auto-phosphorylates at serine 166 (S166), leading to the formation of complex IIc, also known as the 'necrosome' (fig. 3) [25,40]. Research across various cell types has revealed that the necrosome may comprise different proteins: cFLIP, FADD, procaspase-8, RIPK1, and RIPK3[18,25,70]. Nevertheless, consistent evidence highlights the integral role of RIPK1 and RIPK3 in driving necroptosis[39,41–43]. Foundational work by *Zhang et al.* (2017) showcased that mROS, particularly H_2O_2, oxidizes RIPK1 and triggers autophosphorylation of S166 on RIPK1, promoting and accelerating necrosome formation.

Upon phosphorylation of S166, RIPK1 dimerizes, recruiting and binding RIPK3 dimers via their shared RIP homotypic interaction motif (RHIM) domains[40]. This interaction leads RIPK1 to phosphorylate the kinase domain of RIPK3, resulting in a functional necrosome[40]. Subsequently, the necrosome further recruits and phosphorylates mixed-lineage kinase-like (MLKL) pseudokinase, which serves as the principal executor of necroptosis[41,83].

RIPK3-mediated phosphorylation is believed to initiate MLKL oligomerization[83–85]. These MLKL oligomers, likely trimers or tetramers, then travel along microtubules and accumulate at the plasma membrane (PM), where they interact with PM components phosphatidylinositol (PI) and cardiolipin [83–85]. Once at the PM, MLKL oligomers form pores and permeabilize the membrane, facilitating the leakage of otherwise impermeable cellular contents, resulting in cell death (fig. 3) [84,85].

2.3.8 Necroptosis in Muscle

Necroptosis has been detected in diverse cell types and associated with various diseases such as cancer, cardiovascular issues, and inflammatory diseases. Key components of necroptosis, RIPK1, RIPK3, and MLKL, have been identified in C2C12 myoblasts[86]. Additionally, phosphorylated RIPK3 and MLKL have been identified in muscle biopsies of patients with immune-mediated necrotizing myopathy, dermatomyositis and polymyositis[43,87]. RIPK3 protein has also been shown in skeletal muscle (EDL, TA, Gastrocnemius, soleus) of C57BL/6 mice[44]. Previous literature has also demonstrated an increase in the expression of RIPK1, RIPK3 and MLKL in 3-week-old *mdx* mice, a model for Duchenne muscular dystrophy[44]. Further, *Morgan et al.* (2018) showed lower muscle degeneration, evidenced by lower IgG myofiber infiltration in TA's of 3-week-old *mdxRipk3*$^{-/-}$ mice compared to *mdx* mice. Interestingly, IgG myofiber infiltration was similar in 4.5- and 9-week *mdx* and *mdxRipk3*$^{-/-}$ mice, demonstrating that necroptosis, specifically RIPk3, is most active during the peak degenerative phase of DMD (3 weeks)[44]. Additionally, serum Creatine kinase (CK) levels of 3-month-old mice was lower in *mdxRipk3*$^{-/-}$ compared to *mdx* mice, indicating lower overall skeletal muscle turnover in the absence of RIPK3[44]. The limited research on the role of necroptosis in skeletal muscle suggests the occurrence of this RCD in skeletal muscle and its role in atrophy. However, the precise role of necroptosis in cancer-induced cachexia remains undetermined.

Table 3. Summary of original literature investigating necroptosis in skeletal muscle. Literature was identified on PubMed (U.S National Library of Medicine) using the key words "necroptosis" and "skeletal muscle".

Study	Model (human, rodent, cell culture)?	Disease/ Intervention	Tissue	Necroptotic markers measured?	Markers increased or decreased?
Kim et al. (2021)	cell culture	TNF-α, BV6 and zVAD treatment	C2C12	RIPK1, RIPK3 and MLKL phosphorylation	⬆
Shi, Wang, Ke and Lu (2023)	Sprague-Dawley rats	Eccentric exercise	gastrocnemius	RIPK3, MLKL, p-RIPK3 and p-MLKL	⬆
Kamiya et al. (2022)	human	Polymyositis patients	TA	RIPK1, RIPK3 and MLKL	Markers detected but not quantified.
	mouse	Myositis	TA		
Peng et al. (2022)	human	Dermatomyositis and Amyopathic Dermatitis	muscle biopsy (specific muscles unknown)	RIP3 and MLKL protein content	⬆
Morgan et al. (2018)	human	Duchenne Muscular Dystrophy	quadriceps	p-MLKL	⬆
	mouse	mdx	TA	RIPK1/3 and MLKL mRNA, RIPK3 and MLKL protein expression	
Zhou et al. (2020)	mouse	Cardiotoxin induced muscle injury	TA	RIPK1/3 and MLKL protein content	⬆
Dubuisson et al. (2023)	mouse	mdx	quadriceps	p-RIPK1	⬆

CHAPTER 3. RATIONALE, AIMS AND HYPOTHESIS

3.1 RATIONALE

Cancer-induced muscle atrophy (cachexia) has been primarily linked to aberrant protein turnover. While decreased protein synthesis and increased proteolysis are evident in pre-clinical models of cachexia, these patterns do not fully align with observations in human models, suggesting the presence of alternative, unexplored pathways in cachexia [19–24]. Enhanced mROS (specifically H_2O_2) emission observed in skeletal muscle of cancer cachectic mice may provide insight into alternative atrophy-deriving pathways[9,10,88].

The relationship between mROS and proteolysis has been explored in *in vivo* cancer models, both rodent and human [12–14]. However, the role of mROS-regulated cell death pathways in skeletal muscle remains largely unexamined. While several regulated cell death (RCD) pathways exist, only a few are influenced or accelerated by ROS[25]. Among these, even fewer have been shown to regulate skeletal muscle mass, and their role in cancer-induced atrophy is not well understood[35,43,89]. Additionally, a comparative analysis of classical apoptosis mechanisms and other RCDs in atrophying skeletal muscle has yet to be conducted.

Cancer cachexia studies typically assess mitochondrial bioenergetics at a single time point, offering only a snapshot of the events occurring in skeletal muscle mitochondria. While informative, this approach fails to elucidate the dynamic mechanisms and relationships between ROS and muscle atrophy, underscoring the need for studies employing multiple time points[90,91]. Furthermore, although increased mROS has been observed in cancer-induced muscle atrophy and other atrophy models, few studies have attempted to attenuate mROS using commercially available mitochondrial-targeting antioxidants to clarify the underlying mechanisms[14].

Finally, there is a growing call for more orthotopic cancer models, as they better replicate the tumor-host interactions and metastasis seen in humans[92]. The orthotopic ovarian cancer model used in this study meets these criteria. Given that ovarian cancer cachexia is one of the less-studied forms of this syndrome, further research in this area is warranted.

3.2 SPECIFIC AIMS

Aim 1: Determine whether prevention of skeletal muscle mH_2O_2 production via SkQ1 can rescue ovarian cancer induced skeletal muscle atrophy.

Aim 2: Determine whether the exhibited atrophy during ovarian cancer progression is due to mH_2O_2 induced muscle cell death (apoptosis and necroptosis) and whether preventing mH_2O_2 emission can prevent or decelerate these RCDs.

3.3 DETAILED SPECIFIC AIMS

Aim 1: Determine whether prevention of skeletal muscle mH_2O_2 production via SkQ1 can rescue ovarian cancer induced skeletal muscle atrophy.

Objective: Assess mH_2O_2 emission in permeabilized white gastrocnemius fibers across all five experimental groups. Measure the cross-sectional area (CSA) of gastrocnemius muscle fibers to determine the degree of fiber-specific atrophy in each group. These assessments will help determine if SkQ1 can effectively reduce cancer-induced mH_2O_2 emission and preserve myofiber CSA.

Expected Results: Existing literature on skeletal muscle in cancer models indicates a correlation between increased mH_2O_2 levels and myofiber atrophy[10,88]. Consequently, we anticipate elevated mH_2O_2 emission in the skeletal muscle of EOC mice. By employing a two time-point study design

(precachexia vs. cachexia), we aim to discern whether mH_2O_2 elevation precedes myofiber atrophy. We expect that inhibiting mH_2O_2 production with SkQ1 will mitigate the observed atrophy, enhancing our understanding of cancer-induced muscle wasting.

Limitation: The selected time points (40 days vs. 80 days) may not fully capture the progression of mROS emission changes.

Aim 2: Determine whether the exhibited atrophy during ovarian cancer progression is due to mH_2O_2 induced muscle cell death (apoptosis and necroptosis) and whether preventing mH_2O_2 emission can prevent or decelerate these RCDs.

Objective: Investigate whether mH_2O_2 induces apoptosis and necroptosis in skeletal muscle during EOC progression and assess whether preventing mH_2O_2 production can prevent or decelerate these cell death pathways. To achieve this, we will measure markers of apoptosis (mitochondrial permeability transition, and caspase-9 and -3 activity) and necroptosis (RIPK1, RIPK3, MLKL, and their phosphorylated forms) in the skeletal muscle of all five experimental groups. These markers will be specifically analyzed in the white gastrocnemius muscle to complement our mH_2O_2 data. This will help determine whether changes in mH_2O_2 emission precede or correlate with changes in cell death markers. Administration of the mitochondrial-targeting antioxidant SkQ1 will help us determine whether preventing mH_2O_2 emission can regulate apoptosis and necroptosis in skeletal muscle.

Expected Results: The selected cancer progression time points (40 days and 80 days) are based on previous studies using this model, which allowed us to identify pre-cachectic (40 days) and cachectic (80 days) stages[9]. We expect that markers of both apoptosis and necroptosis will be elevated prior to (40 days) or concurrent with (80 days) a decrease in myofiber cross-sectional

area. Given existing literature showing that mROS can induce or accelerate apoptosis and necroptosis, we hypothesize that attenuating mROS with SkQ1 will reduce these cell death markers[25,40].

Limitation: Changes in cell death markers are transient but induce lasting effects. Our study design, which includes only two time points (40 and 80 days), may be insufficient in capturing these transient changes comprehensively. Additionally, while apoptosis and necroptosis pathways are mutually exclusive within a single cell, they are not mutually exclusive within a tissue. Some myofibers in the gastrocnemius may undergo apoptosis while others undergo necroptosis. This study design does not allow us to determine which specific fibers undergo which form of regulated cell death (RCD); rather, it will indicate whether either pathway is present and elevated in some groups.

3.4 HYPOTHESIS

We hypothesize that mitochondrial mH_2O_2 induces skeletal muscle atrophy in a time-dependent manner. Further, enhanced mH_2O_2 with cancer progression induces apoptosis and necroptosis within myofibers deriving the exhibited atrophy. Additionally, administration of the mitochondrial targeting antioxidant, SkQ1, will attenuate mH_2O_2 emission, thereby mitigating the RCDs apoptosis and necroptosis and ultimately preventing atrophy.

3.5 AUTHOR CONTRIBUTIONS

The majority of the experiments in this project were carried out by Shahrzad Khajehzadehshoushtar. Dr. Jim Petrik's lab at the University of Guelph was responsible for injecting all EOC mice. Mice morphometric data were collected by S.K and L.D over three months. Caspase activity assays were conducted by F.R at the University of Waterloo, as this assay is part of their expertise. All other assays were completed by S.K.

3.6 ADDITIONAL CONTRIBUTIONS

Co-Author Published

Delfinis LJ, Ogilvie LM, **Khajehzadehshoushtar S**, et al. Muscle weakness and mitochondrial stress occur before severe metastasis in a novel mouse model of ovarian cancer cachexia. *Mol Metab*. 2024;86:101976.

Garibotti MC, **Khajehzadehshoushtar S**, Andrews NJ, Malekzadeh R. Age-related changes of skeletal muscle metabolic response to contraction are also sex-dependent. *J Physiol*. Published online December 27, 2023.

First Author in Progress

Khajehzadehshoushtar S, Delfinis LJ, Rahman F, Garibotti MC, Gandhi S, Brahmbhatt AN, Morris BA, Garlisi B, Lauks S, Aitken C, Petrik J, Quadrilatero J, Perry CGR. Exploring the relationship between mitochondrial-linked cell death and muscle atrophy during ovarian cancer progression.

Co-Author in Progress

Delfinis LJ, **Khajehzadehshoushtar S**, and Perry CGR. Understanding mitochondrial function vs dysfunction in non-disease- and disease-induced muscle disuse/inactivity. Invited review, *J Phyiol*.

Delfinis LJ, **Khajehzadehshoushtar S**, Flewweling LD, Andrews NJ, Garibotti MC, Gandhi S, Brahmbatt A, Morris B, Garlisi B, Lauks S, Aitken C, Cheng AJ, Petrik J, Perry CGR. Muscle weakness before and during ovarian cancer-induced cachexia is partially prevented by the mitochondrial-targeted drug SkQ1 in mice**.**

Garibotti MC, Thuhan AT, Delfinis LJ, **Khajehzadehshoushtar S**, Abdul-Sater AA, Perry CGR. An examination of relationships between mitochondrial stress and muscle health in a modified mouse model of experimental autoimmune myositis.

CHAPTER 4. METHODS

Study Approval

All procedures were approved by the Animal Care Committees at the University of Guelph and York university (AUP# 2021-04) and in compliance with Canadian Council on Animal Care guidelines.

Study Design

Transformed murine ovarian surface epithelial cells (EOC) from C57BL/6J mice were injected beneath the ovarian bursa of syngeneic adult female mice. These were compared to phosphate-buffered saline (PBS) injected controls (PBS-control, n=24). Tumors were allowed to progress for either 40 or 80 days. After EOC injections, half of the mice received 250 nmol/kg body weight SkQ1 in their drinking water (EOC-40-SkQ1, n=12; EOC-80-SkQ1, n=30), while the rest received standard water (EOC-40, n=12; EOC-80, n=30).

Animal Care and Tumor Injection

Cell Culture. Spontaneously transformed murine ovarian epithelial cells (ID8), donated by Drs. K. Roby and P. Terranova from Kansas State University, were cultured in Dulbecco's Modified Eagle Medium (DMEM) supplemented with 10% Fetal Bovine Serum (FBS) and 1% antibiotic/antimycotic.

Animals and Tumor Implantation. Female C57BL/6 mice, aged 10 and 16 weeks, were implanted with ID8 cells to establish an orthotopic, syngeneic mouse model of EOC. Dr. Jim Petrik at the University of Guelph, Ontario, Canada, performed all tumor injections following the methodology previously outlined by *Ogilvie et al.* (2023). Under isoflurane anesthesia, a dorsal incision was made, and $1.0x10^6$ ID8 cells suspended in 5 µl PBS were injected directly beneath the bursa of the left ovary. Control mice underwent an identical procedure but received a 5 µl

injection of PBS without cancer cells. The mice were observed for 2 weeks before being transferred to the animal facility at York University.

To differentiate between pre-cachexia and cachexia models, tumors were allowed to develop for either 40 or 80 days, respectively. Tumors were allowed to develop for the specified durations, with endpoints set at 21-23 weeks of age to prevent age-related changes in muscle mass.

Weekly measurements of food and water intake were recorded until the endpoint, while body weights were initially measured weekly for 45 days, then daily due to the rapid deterioration in the animals' condition. Mice displaying severe distress, undergoing more than five abdominal paracentesis procedures (up to 20 ml ascites), or experiencing >15% body weight loss were euthanized promptly.

SkQ1 Administration. Immediately after tumor implantation, mice in the SkQ1 groups received SkQ1 (Cayman Chemical, 19891, dissolved in a 1:1 ethanol and water solution) in their drinking water (250 nmol/kg body weight/day) until the endpoint[93,94]. Mice were estimated to weigh 25g on average and drink 5 mL/day, resulting in a 1.25 nmol/mL concentration of SkQ1. The ethanol concentration in the drinking water was approximately 0.0008%, derived from a 50 mg/mL 1:1 ethanol stock. Non-SkQ1 groups received regular drinking water, as the ethanol concentration was negligible (0.008%).

Abdominal Paracentesis. Primary tumors emerged approximately 8.5 weeks post-injection of EOC ID8 cells, followed by ascites development, resembling stage III EOC. Mice with significant ascites underwent abdominal paracentesis using a 3-gauge needle under isoflurane anesthesia to alleviate discomfort and ensure proper functioning of nearby organs.

Surgical Procedures. Mice were euthanized under isoflurane, and various tissues, including the quadriceps, gastrocnemius, tibialis anterior, extensor digitorum longus, plantaris,

soleus, heart, spleen, kidneys, liver, lungs, tumor, and inguinal fat, were collected. Muscle tissues, spleen, tumor, and inguinal fat were weighed, and all tissues were snap-frozen in liquid nitrogen and stored at -80°C. The red portions of the gastrocnemius muscles were excised and similarly snap-frozen. For half of the animals, the white gastrocnemius (WG) was divided: one piece was used for bioenergetic assays, while the other was used for sub-cellular fractionation and saved for future studies. For the second half of mice per group, one WG was flash-frozen, and the other was OCT-embedded. Due to the lower n size of the 40-day cancer groups, half of one gastrocnemius was used for bioenergetics, while the other half was OCT-embedded. The other gastrocnemius was used for western blotting. A similar approach was used for the quadriceps muscle, with two quadriceps utilized for sub-cellular fractionation, one snap-frozen, and the other embedded in OCT.

Mitochondrial Bioenergetic Assessments

Preparation of permeabilized muscle fibres. Preparation of permeabilized muscle fibre bundles (pmfb) and H_2O_2 analysis was performed as previously established in our lab[10,95,96]. Briefly, WG was immediately placed in BIOPS comprising (mM) 50 MES Hydrate, 7.23 K_2EGTA, 2.77 CaK_2EGTA, 20 imidazole, 0.5 dithiothreitol, 20 taurine, 5.77 Na_2ATP, 15 Na_2PCr, and 6.56 $MgCl_2$.6 H2O (pH 7.1) following removal. Under 10x magnification, WG was trimmed of fat and connective tissue, and divided into 9 smaller bundles (8 for H_2O_2 analysis and 1 for calcium retention capacity). All bundles were made from the centre of the white gastrocnemius muscle and gently separated along the longitudinal axis.

Bundles were then treated with 40 μg/ml saponin in BIOPS on a rotor for 30 minutes at 4 °C (permeabilization). For bundles intended for mH_2O_2 emission measurement related to Complex I, II, and pyruvate dehydrogenase complex, an additional treatment with 35 μM 2,4-

dinitrochlorobenzene (CDNB) was applied during the permeabilization step. This step served to deplete glutathione, enabling detectable rates of mH_2O_2.

Following permeabilization, bundles were divided into 2 groups: 1) bundles intended for mitochondrial H_2O_2 emission were placed in buffer Z comprising (in mM) 105 K-MES, 30 KCl, 10 KH_2PO_4, 5 $MgCl_2 \cdot 6H_2O$, 1 EGTA and 5 mg/mL BSA (pH 7.4) on a rotator at 4 °C for 15 minutes. 2) bundles intended for calcium retention capacity were placed in 1 mM EGTA in Buffer Y comprising (mM) 250 sucrose, 10 Tris-HCl, 20 Tris-base, 10 KH_2PO_4, 0.5 mg/ml BSA (pH 7.2) on a rotator for 10 minutes at 4 °C. Subsequently, CRC bundles were transferred to a second wash of Buffer Y with 10 μM Blebbistatin (BLEB, to prevent ATP induced muscle contraction) on a rotor at 4 °C for a minimum of 10 minutes until measurements were initiated.

Mitochondrial H_2O_2 Emission (mH_2O_2). H_2O_2 was determined fluorometrically (QuantaMaster 40, HORIBA Scientific, Edison, NJ, USA) in a quartz cuvette with continuous stirring at 37 °C, in 1 ml Buffer Z supplemented with 10 μM Amplex Ultra Red, 0.5 U/mL horseradish peroxidase, 1 mM EGTA, 40 U/mL Cu/Zn-SOD1, 5 μM BLEB, and 20 mM Cr. Site specific induction of H_2O_2 was measured through the addition of either 10 mM Pyruvate and 2 mM malate (NADH, complex I), 10 mM succinate ($FADH_2$, complex I via reverse electron flux from complex II) or 2.5 μM Antimycin A (Complex III). Additionally, using 0.5 μM rotenone, a complex I inhibitor, with 10 mM pyruvate, electron slip specific to pyruvate dehydrogenase complex was also measured in CDNB-treated fibres. Following the induction of state II mH_2O_2 by complex I and II substrates, ADP was titrated progressively attenuate mH_2O_2. The rate of mH_2O_2 emission was be calculated from the slope (F/min) of a standard curve established with the same reaction conditions and normalized to fibre bundle dry weight.

Mitochondrial Calcium Retention Capacity (CRC). CRC was determined fluorometrically (QuantaMaster 80, HORIBA Scientific, Edison, NJ, USA) in a quartz cuvette with continuous stirring at 37 °C. Prior to the initiation of each experiment, the cuvette was placed on a stir plate with 500 µl water and 10 mM EGTA. The water was then aspirated from the cuvette but not rinsed, leaving the EGTA coating on the cuvette walls to chelate any residual Ca^{2+} in the assay buffer. Background fluorescence was obtained following the addition of 5 mM glutamate, 2mM malate, 25 µM ATP and the pmfb to 300 µl CRC buffer comprising 1 µM Calcium Green-5N (Invitrogen), 20 mM creatine, 40 µM EGTA, 5 µM BLEB, 2 µM thapsigargin in Buffer Y. Calcium uptake was then initiated by a single 8 nmol pulse of $CaCl_2$. Subsequent 4 nmol pulses of $CaCl_2$ were added until mitochondrial permeability transition pore (mPTP) opening was evident. Three 0.5 mM pulses of $CaCl_2$ was then added to saturate the fluorophore and establish a fluorescence maximum (Fmax). Changes to free Ca^{2+} in the cuvette during mitochondrial Ca^{2+} uptake were calculated using the known K_d for Calcium Green-5N and the equations established for calculating free ion concentrations using ion sensitive fluorophores.

Upon completion of mH_2O_2 and CRC experiments, the fibres were rinsed in deionized H_2O, lyophilized in a freeze-dryer (Labconco, Kansas City, MO, USA) for > 4 hours and weighed on a microbalance (Sartorius Cubis Microbalance, Gottingen, Germany).

Validating Necroptosis Antibodies

It was crucial to verify the reliability of the purchased necroptosis antibodies in muscle tissue due to the scarcity of literature on this cell death mechanism in skeletal muscle. Initially, we induced necroptosis in C2C12 myoblasts, donated by Dr. Olasunkanme Adegoke from York University, using a well-established cell culture necroptosis model[86,97]. Additionally, RIPK3 knockout (KO) gastrocnemius and quadriceps muscles, donated by Dr. Zhu-Xu Zhang from

Western University, were used as negative controls. We also used gastrocnemius and quadriceps muscles from our D2.mdx bank for an additional positive control, as recent literature has demonstrated necroptosis in Duchenne Muscular Dystrophy (DMD) mice.

C2C12 treatment. C2C12 cells were maintained in growth medium (GM) consisting of DMEM, 10% FBS and 1% penicillin/streptomycin.C2C12 myoblasts underwent treatment with TNF-a to activate the cell death mechanisms. Additionally, a pan-caspase inhibitor z-VAD-FMK and caspase-8 specific inhibitor z-IETD-FMK were used to prevent inhibit caspases and thus prevent apoptosis. Finally, to induce necroptosis, BV6, a general inhibitor of proteins that ubiquitinate RIPK1 was employed, to allow RIPK1 to dissociate from complex I (fig. 3). Briefly, C2C12 myoblasts, seeded on 6-well culture plates, were exposed to a combination of 10 nM/ml TNF-α (T, Peprotech), 1 μM BV6 (B, APEXBIO), 20 μM z-Vad-FMK (Z, APEXBIO), and 20 μM z-IETD-FMK (I, APEXBIO). C2C12 cells were assessed at various time points following TBZI treatment, and at both low-dose (10 nM/ml) and high-dose (100 nM/ml) TNF-α concentrations to optimize the necroptosis model. It was determined that 10 nM/ml TNF-α, assessed 24 hours following TBZI treatment, yielded the greatest positive results for necroptosis proteins, as evidenced by Western blot analysis.

After the treatment period, cells were harvested, homogenized, and subjected to Western blot analysis to confirm the presence and reliability of necroptosis-related proteins.

Western Blotting

An aliquot of frozen Quadriceps and WG were homogenized in ice cold homogenization buffer comprising (in mM): 10 Tris-HCl, 150 NaCl, 1 EDTA, 1 EGTA, 2.5 $Na_4O_7P_2$, and 1 Na_3VO_4, 1% Triton X-100, 1:200 protease and phosphatase inhibitors (MilliporeSigma, pH 7.0) using a polytron homogenizer at low speed.

Protein concentrations of homogenized tissues were determined using Bicinchoninic acid assay (BCA, Life Technologies, Carlsbad, CA, USA). 15-60 μg of denatured and reduced protein was subjected to 8-12% gradient SDS-PAGE followed by transfer to low-fluorescence polyvinylidene difluoride membrane (LF PVDF, BIORAD). Membranes were blocked with LICOR Odyssey TBS Blocking Buffer (LI-COR) and immunoblotted 24-48 hours (4°C) with antibodies specific for each protein. The following primary antibodies will be used to detect necroptosis: RIPK1 and phospho-RIPK1 (Cell Signalling, 79 kDa,1:500 and 1:250), RIPK3 (ProSci Inc., 53 kDa, 1:500), MLKL (Abcepta, 54 kDa, 1:500), phospo-RIPK3 and phospho-MLKL (Abcam, 53 and 54 kDa, 1:250 and 1:250). A rodent OXPHOS antibody cocktail was sued to detect electron transport chain protein subunits (Abcam, 1:250): ATP5A (complex V, 55 kDa), UQCRC2 (Complex III, 48 kDa), MTCO1v (Complex IV, 40 kDa), SDHB (Complex II, 30 kDa) and NDUFB8 (Complex I, 20 kDa).

After incubation in primary antibodies, membranes were subjected to three 5-minute washes in TBS-Tween followed by 1-hour incubation at room temperature with an infrared fluorescent secondary antibody (LI-COR, IRDYE 680RD goat-anti-mouse and goat-anti-rabbit) at a previously optimized dilution (1:20,000). Immunoreactive proteins will be detected using infrared imaging (LI-COR CLx; LICOR) and subsequently quantified via densitometry using ImageJ (NIH). All images were normalized to Amido Black total protein stain (MilliporeSigma).

Caspase Activity

WG muscles were homogenized as above in the absence of protease inhibitors. Samples were incubated at room temperature for 2 hours with 20μM Ac-DEVD-AFC (Alexis Biochemicals) for caspase-3 or Ac-LEHD-AFC (Alexis Biochemicals) for caspase-9 in assay buffer (20 mM HEPES pH 7.4, 10 mM DTT, and 10% glycerol). Fluorescence was measured at

room temperature using a Cytation 5 Imaging Multi-Mode Reader (BioTek) with excitation and emission wavelengths at 400 and 505 nm respectively for AFC substrates (i.e., Caspase-3 and Caspase-9). The activity assay was normalized to protein concentration of samples (BCA assay) and expressed as fold changes in fluorescence.

Immunofluorescence

Sample Preparation. Quadriceps and full gastrocnemius muscles embedded in O.C.T medium (Thermo Fisher Scientific) were cut into 10 μm sections with a cryostat (HM525 NX, Thermo Fisher Scientific) at -20 °C. Cryosections were used for immunofluorescence analysis.

Immunofluorescence Analysis. Muscle fiber type analysis followed the methodology described by *Delfinis et al. (2022)*, allowing determination of fiber-type-specific atrophy. All primary antibodies will were purchased from the Developmental Studies Hybridoma Bank (University of Iowa), and secondary antibodies will be purchased from Invitrogen, Thermo Fisher Scientific. Briefly, slides were blocked with 5% goat serum (MilliporeSigma) in PBS for 1 hour at room temperature. Next, slides were incubated with primary antibodies against MHC I (BA-F8; 1:25), MHC IIA (SC-71; 1:1,000), and MHC IIB (BF-F3; 1:50) for 2 hours at room temperature. Slides underwent three 5-minute PBS washes and incubated with secondary antibodies (MHC I; Alexa Fluor 350 IgG2b; 1:1,000) (MHC IIa; Alexa Fluor 488 IgG1; 1:1,000) (MHC IIb; Alexa Fluor 568 IgM; 1:1,000) for 1 hour at room temperature. Following incubation, slides were washed thrice more in PBS for 5-minutes per wash and mounted with ProLong antifade reagent (Life Technologies, Thermo Fisher Scientific).

Images were acquired after 24 hours through the AOMF facility at University of Toronto. A total of 30–40 muscle fibers per fiber type were selected randomly throughout the cross section

and traced with ImageJ software to assess cross-sectional area and minimal-feret diameter. Muscle fibers exhibiting a black appearance were classified as MHC IIX.

Statistics

Results are expressed as mean +/- SEM. The level of significance was established at $p < 0.05$ for all statistics. Before statistical analyses, outliers were omitted in accordance with ROUT testing (Q = 0.5%) and then tested for normality using a D'Agostino–Pearson omnibus normality test. For data that passed normality, standard one-way ANOVAs were performed. For data that did not pass normality, the non-parametric Kruskal-Wallis test was used. Data with two independent values that did not pass normality were first log transformed then analyzed using a standard two-way ANOVA. The results presented in **Fig.7** are non transformed data, for transformed data refer to **SFig. 4**. Post-Hoc analyses were performed for data that depicted significance using the two-stage step-up method of Benjamini, Krieger, and Yekutieli to adjust for false discovery rate. The purpose of this study was to investigate the effect of ovarian cancer progression and the effect of SkQ1 treatment on skeletal muscle. Thus, the following comparisons were not conducted: EOC-40 vs EOC-80-SkQ1, and EOC-40-SkQ1 and EOC-80. The Mantel-Cox test was used to compute a curve comparison of survival data ($p < 0.05$). All Statistical analyses were performed on Graphpad Prism 10 (La Jolla, CA, USA). Corresponding statistical tests are provided in figure legends.

CHAPTER 5. RESULTS

SkQ1 does not prevent ovarian cancer-induced body weight and fat loss, nor does it influence survivability.

ID8 epithelial ovarian cancer (EOC) cells were injected directly beneath the ovarian bursa of syngeneic female mice and compared to PBS-injected sham mice (**Fig. 4A**). EOC tumors were allowed to grow for 40 and 80 days. Half of the EOC-injected mice in both the 40- and 80-day groups received the mitochondria targeting antioxidant SkQ1 in their drinking water. Mice exhibiting more than 15% body weight loss or undergoing five abdominal paracentesis procedures (~20 mL) were immediately sacrificed, which occurred only in the late-stage (80-day) tumor-bearing groups. There were no significant differences in the survival rates between the EOC-80-SkQ1 group and the normal drinking water group (**Fig. 4C**).

Body weights were reduced at 80 days in EOC tumor-bearing mice, with no changes observed due to SkQ1 treatment (**Fig. 4B, D, E).** This decrease in body weight was accompanied by reductions in inguinal fat pads at 80 days, again with no effect from SkQ1 treatment (**Fig. 4F**). Spleens were measured at endpoint as an indicator of inflammation. Although the average spleen weight was elevated in the 80-day cancer groups, it was not statistically different from the control group (**Fig. 4G**).

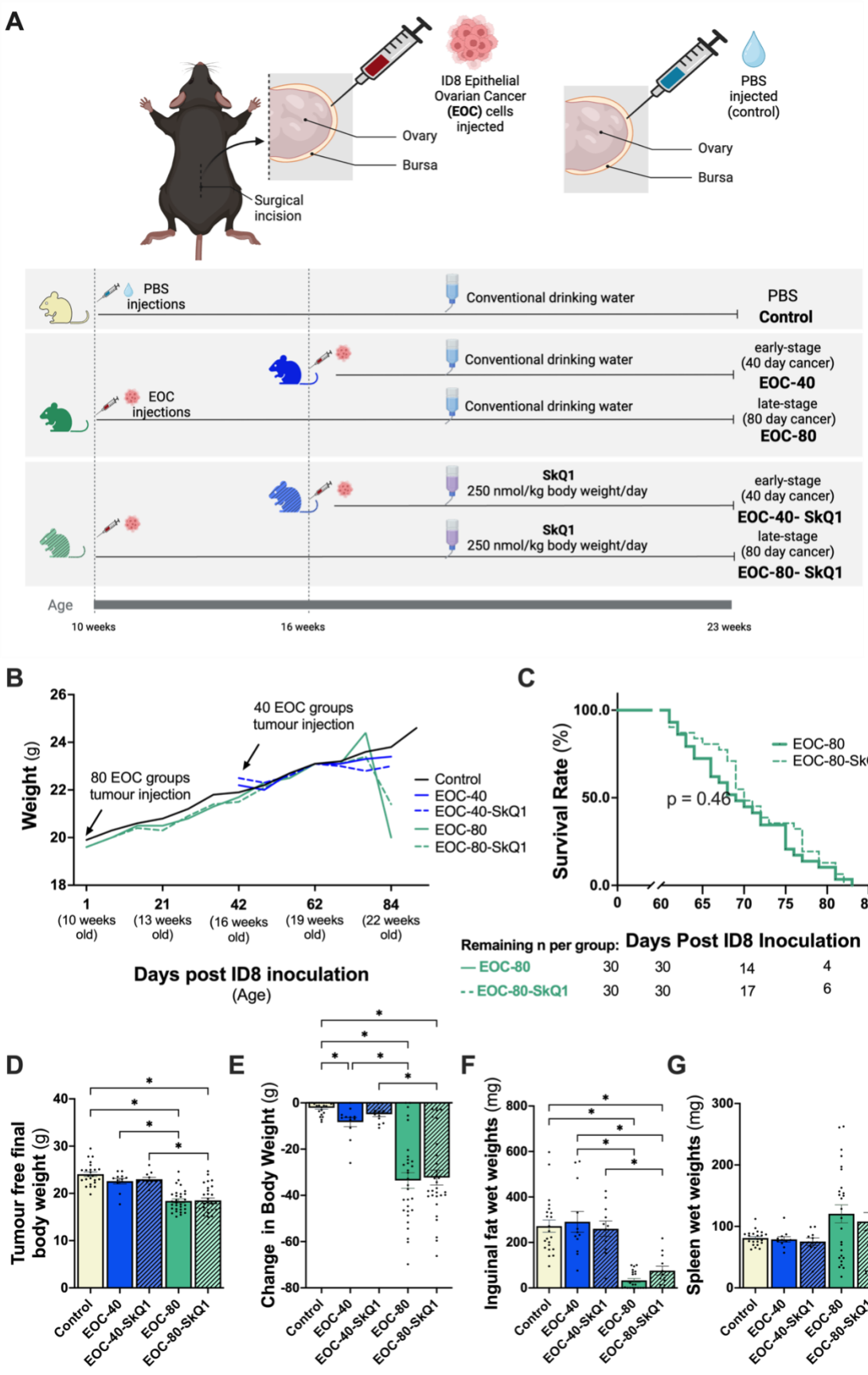
A
ID8 Epithelial Ovarian Cancer (EOC) cells injected
Ovary
Bursa
Surgical incision
PBS injected (control)
Ovary
Bursa
PBS injections
Conventional drinking water
PBS
Control
EOC injections
Conventional drinking water
early-stage (40 day cancer)
EOC-40
Conventional drinking water
late-stage (80 day cancer)
EOC-80
SkQ1
250 nmol/kg body weight/day
early-stage (40 day cancer)
EOC-40- SkQ1
SkQ1
250 nmol/kg body weight/day
late-stage (80 day cancer)
EOC-80- SkQ1
Age
10 weeks
16 weeks
23 weeks
B
Weight (g)
40 EOC groups tumour injection
80 EOC groups tumour injection
Control
EOC-40
EOC-40-SkQ1
EOC-80
EOC-80-SkQ1
1 (10 weeks old)
21 (13 weeks old)
42 (16 weeks old)
62 (19 weeks old)
84 (22 weeks old)
Days post ID8 inoculation (Age)
C
Survival Rate (%)
EOC-80
EOC-80-SkQ1
p = 0.46
Days Post ID8 Inoculation
Remaining n per group:
EOC-80 30 30 14 4 0
EOC-80-SkQ1 30 30 17 6 0
D
Tumour free final body weight (g)
E
Change in Body Weight (g)
F
Inguinal fat wet weights (mg)
G
Spleen wet weights (mg)
Control
EOC-40
EOC-40-SkQ1
EOC-80
EOC-80-SkQ1

Figure 4. The effects of ovarian cancer progression and SkQ1 treatment on body weight, survival, and adipose tissue. A) Study design. Transformed murine ovarian surface (ID8) epithelial cells (EOC) from C57BL/6J mice were injected beneath the ovarian bursa of syngeneic adult female mice and compared to PBS-injected controls (PBS-control, n=24). Tumors progressed for 40 and 80 days. Following EOC injections, half the mice received the mitochondrial-targeting antioxidant, SkQ1 in drinking water (EOC-40-SkQ1 n=12, EOC-80-SkQ1 n=30), while the rest received standard water (EOC-40 n=12, EOC-80 n=30). **B)** Timeline of average bodyweight per group post tumour and PBS injections**. C)** Survival rate of EOC-80 and EOC-80-SkQ1 groups. **D)** Tumour free final body weight and **E)** difference between peak and final body weights per group (peak body weight – final body weight). **F)** Inguinal fat wet weights at endpoint. **G)** Spleen wet weights at endpoint. n=12-30 per group. Survival curve analysis in **C** was performed using the Mantel-Cox survival test. Analyses for **D-G** were conducted using either a standard one-way ANOVA or Kruskal-Wallis test, depending on whether data was normally distributed. These were followed by a two-step step-up method of Benjamini, Krieger, and Yukutieli for post-hoc analysis. Results represent mean ± SEM. ***** = $p < 0.05$.

SkQ1 does not affect tumour growth nor ascites fluid development.

Primary ovarian tumors (at the original site of EOC injection) were excised and weighed at the endpoint. As expected, the primary tumors were significantly larger at 80 days post-EOC injection. (**Fig. 5A**). Mice in the 80-day cancer group developed ascites fluid, necessitating an average of 2.5 abdominal paracentesis procedures, resulting in approximately 10 mL of ascites fluid removed per group (**Fig. 5B-D**). SkQ1 did not induce any changes in tumour size, ascites fluid development or metastasis of EOC cells to the diaphragm (**SFig. 1**)

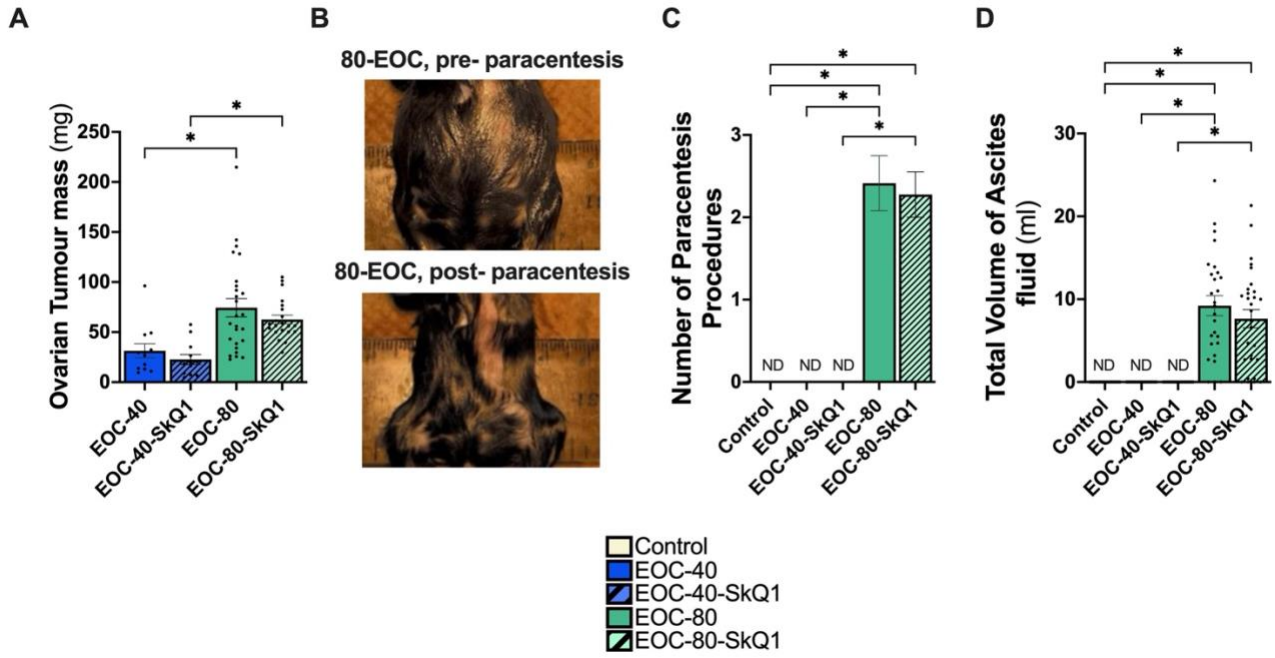

Figure 5. The effect of SkQ1 on primary tumour growth and ascites fluid development. A) Primary ovarian tumour mass at endpoint. **B)** Abdomen size prior to and post ascites fluid removal via paracentesis procedure. **C)** Average number of paracentesis procedures per mouse. **D)** Total volume of Ascites fluid removed per mouse. n= 12-26. **ND:** None detected, these groups did not develop ascites. Analyses for **A, C, and D** were conducted using either a standard one-way ANOVA or Kruskal-Wallis test, depending on whether data was normally distributed. These were followed by a two-step step-up method of Benjamini, Krieger, and Yukutieli for post-hoc analysis. Results represent mean ± SEM. ***** = $p<0.05$.

SkQ1 does not prevent ovarian cancer-induced skeletal muscle atrophy.

To further characterize our model, we measured hindlimb muscle wet weights at endpoint as an index of atrophy. Hindlimb muscle wet weights were generally reduced in both 80-day EOC groups, with the exception of the soleus muscle, where there was a transient increase in muscle wet weights in the 40-day EOC groups followed by a decrease in the 80-day groups (**Fig. 6A**). There were no differences between the SkQ1 and normal drinking water groups.

The gastrocnemius muscle was stained for myosin heavy chain (MHC) isoforms to examine fiber-specific changes (**Fig. 6B**). Cross-sectional area (CSA) of type IIb fibers significantly decreased in all cancer groups, and this effect was maintained when all fiber types were pooled together, indicating that the average fiber size per group was lower in the EOC groups (**Fig. 6C and D**). Minimal Feret Diameter (MFD) was also measured as a second indicator of fiber-specific changes. Similar to CSA, MFD of type IIb fibers decreased in all cancer groups (**Fig. 6E**). However, this effect was not observed when all fiber types were pooled together (**Fig. 6F**).

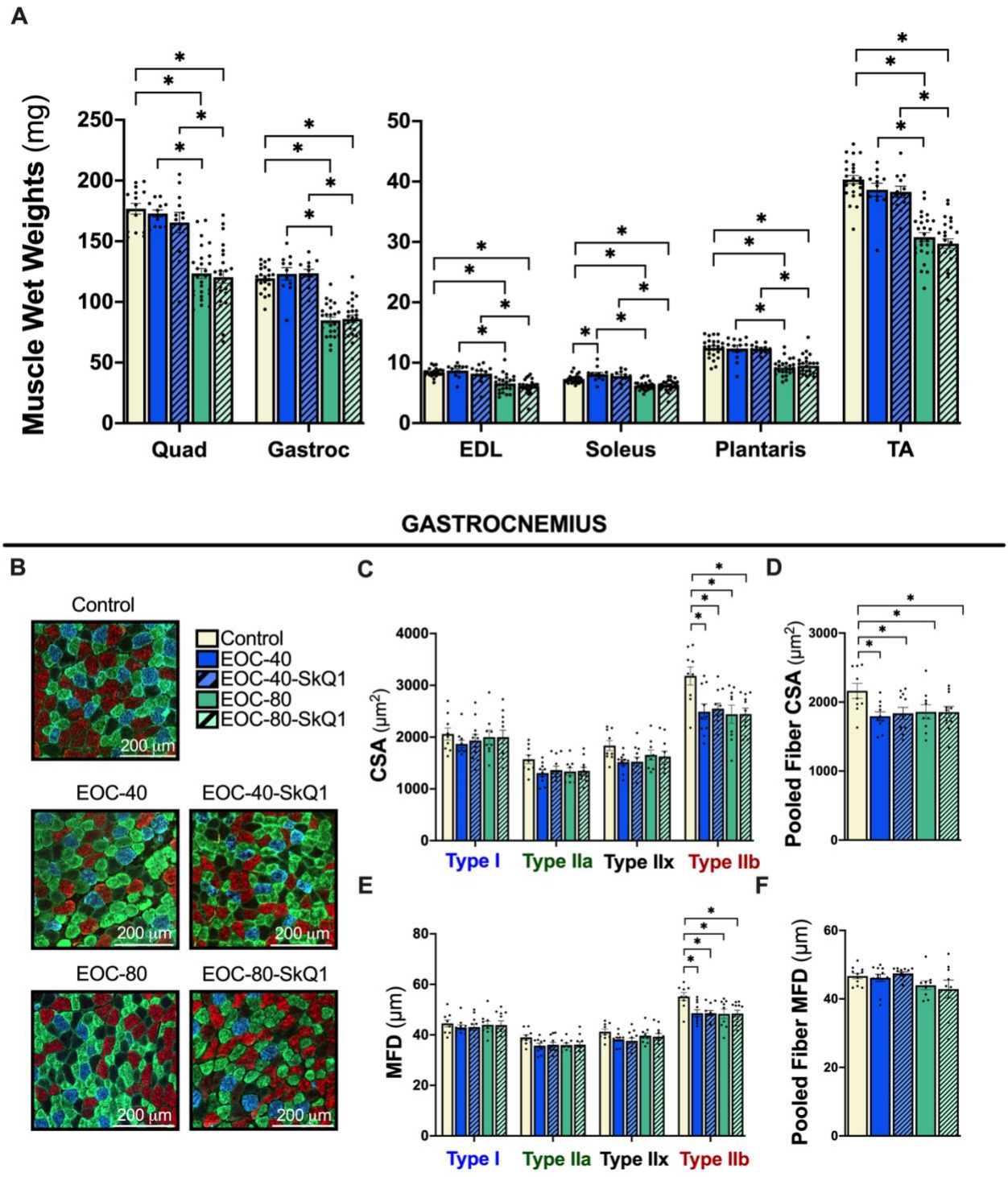
A
Muscle Wet Weights (mg)
Quad
Gastroc
EDL
Soleus
Plantaris
TA
GASTROCNEMIUS
B
Control
EOC-40
EOC-40-SkQ1
EOC-80
EOC-80-SkQ1
200 µm
C
CSA (µm²)
Type I
Type IIa
Type IIx
Type IIb
D
Pooled Fiber CSA (µm²)
E
MFD (µm)
F
Pooled Fiber MFD (µm)

Figure 6. Evaluation of endpoint skeletal muscle wet weights and gastrocnemius fiber type atrophy with ovarian cancer progression. A) Hindlimb muscle wet weights at endpoint. **B)** Representative images of gastrocnemius cross-sections. n= 12 - 26. Blue corresponds to type I fibers, green: type IIa, black: type IIx, and red: type IIb fibers. **C)** Cross-sectional area (CSA) of gastrocnemius muscle fibers stained for myosin-heavy chain (MHC) isoforms, n=9 -12. **D)** Pooled gastrocnemius muscle fiber CSA, n=9 -12 **E)** Minimal-feret diameter (MFD) of gastrocnemius muscle fibers stained for myosin-heavy chain (MHC) isoforms and **F)** pooled MFD of gastrocnemius fibers, n=9 -12. **QUAD**: quadriceps, **Gastroc**: Gastrocnemius, **EDL**: Extensor Digitorum Longus, **TA**: Tibialis Anterior. Analyses for **A, C, D, E and F** were conducted using either a standard one-way ANOVA or Kruskal-Wallis test, depending on whether data was normally distributed. These were followed by a two-step step-up method of Benjamini, Krieger, and Yukutieli for post-hoc analysis. Results represent mean ± SEM. ***** = $p < 0.05$.

SkQ1 rescued complex I and II protein content and ameliorated ovarian cancer-induced mitochondrial H_2O_2 (ROS) emission in mixed gastrocnemius muscles of 80-day EOC mice.

Electron transport chain complex content (specific subunits) was measured as an indirect indicator of mitochondrial quantity. Protein content of complexes I and II decreased in the EOC-80 group compared to the EOC-40 group, and this decrease remained evident when protein content of all complexes was pooled (**Fig. 7B**). However, this decrease in Complex I and II was not observed in the EOC-80-SkQ1 group compared to the EOC-40-SkQ1 group. Furthermore, the average protein content per complex in the EOC-80-SkQ1 group was comparable to Control protein content, suggesting that SkQ1 helps preserve Complex I and II quantity.

We then assessed mH_2O_2 emission using various substrates and inhibitors to identify changes in mH_2O_2 emission at specific sites. Complex I-supported (NADH supplied via pyruvate and malate) maximal H_2O_2 emission did not change with EOC or SkQ1 administration (**Fig. 7C, SFig. 3A**). ADP was then titrated to assess changes in mH_2O_2 during oxidative phosphorylation (OXPHOS). Interestingly, mH_2O_2 emission was heightened in both 80-day EOC groups compared to control and their earlier 40-day counterparts, suggesting ADP is less effective at suppressing H_2O_2 emission at late-stage EOC (**SFig. 3B**). Notably, normalization of H_2O_2 data to ETC content

revealed a significant decrease in EOC-80-SkQ1 compared to EOC-80, indicating that EOC-80-SkQ better attenuates H_2O_2 emission (**Fig. 7D**).

To further decipher whether the changes in H_2O_2 emission during OXPHOS were due to ETC sensitivity versus starting maximal H_2O_2 emission, absolute H_2O_2 emission (+ADP) during OXPHOS was normalized to maximal mH2O2 emission (-ADP) and expressed as a percentage. The same pattern held, with 80-day EOC groups exhibiting heightened H_2O_2 emission, which appeared to be attenuated by SkQ1 (**Fig. 7E**). A further pattern emerged regarding responsiveness to ADP, with EOC-40-SkQ1 producing more H_2O_2 compared to EOC-40.

Complex II-supported ($FADH_2$ supplied via succinate) maximal and absolute H_2O_2 emission during OXPHOS (via reverse electron flow) yielded the same results (**SFig. 3C-D, Fig. 7F-H**). H_2O_2 emission from the pyruvate dehydrogenase complex (rotenone and pyruvate) did not change with ovarian cancer progression or SkQ1(**SFig. 3E**). Similarly, H_2O_2 emission from Complex III to the intermembrane space (Antimycin A) also did not change with ovarian cancer progression or SkQ1 (**SFig. 3F**).

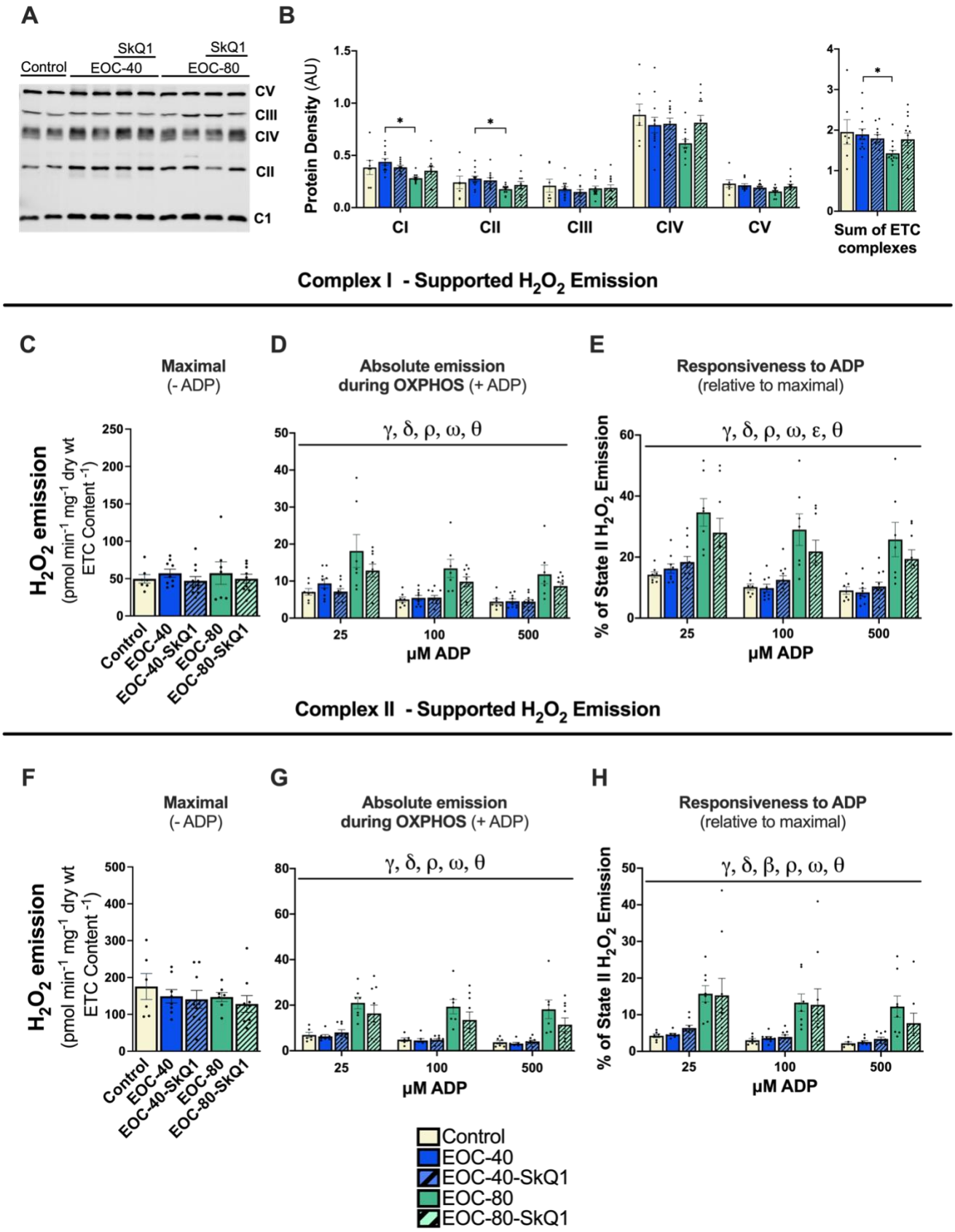
A
Control
SkQ1
EOC-40
SkQ1
EOC-80
CV
CIII
CIV
CII
C1
B
Protein Density (AU)
CI
CII
CIII
CIV
CV
Sum of ETC complexes
Complex I - Supported H2O2 Emission
C
Maximal
(- ADP)
H2O2 emission
(pmol min-1 mg-1 dry wt
ETC Content -1)
Control
EOC-40
EOC-40-SkQ1
EOC-80
EOC-80-SkQ1
D
Absolute emission
during OXPHOS (+ ADP)
γ, δ, ρ, ω, θ
μM ADP
E
Responsiveness to ADP
(relative to maximal)
γ, δ, ρ, ω, ε, θ
% of State II H2O2 Emission
μM ADP
Complex II - Supported H2O2 Emission
F
Maximal
(- ADP)
H2O2 emission
(pmol min-1 mg-1 dry wt
ETC Content -1)
Control
EOC-40
EOC-40-SkQ1
EOC-80
EOC-80-SkQ1
G
Absolute emission
during OXPHOS (+ ADP)
γ, δ, ρ, ω, θ
μM ADP
H
Responsiveness to ADP
(relative to maximal)
γ, δ, β, ρ, ω, θ
% of State II H2O2 Emission
μM ADP
Control
EOC-40
EOC-40-SkQ1
EOC-80
EOC-80-SkQ1

Figure 7. Changes in ETC content and Complex I- and II-supported H_2O_2 emission in white gastrocnemius of EOC-bearing mice subjected to either SkQ1 or normal drinking water. A) Representative western blot of ETC complex proteins in mixed gastrocnemius. **B)** Protein density of electron transport chain (ETC) complexes in the mixed gastrocnemius, n=7-13. **C)** Complex I -supported (NADH supplied via pyruvate and malate) maximal H_2O_2 emission normalized to ETC content. n= 7-11. **D)** Complex I -supported and ADP stimulated absolute H_2O_2 emission during oxidative phosphorylation (OXPHOS) normalized to ETC content. **E)** Responsiveness of ETC to ADP (absolute H_2O_2 emission as a percentage of maximal). **F)** Complex II -supported ($FADH_2$ supplied via succinate) maximal H_2O_2 emission normalized to ETC content. **G)** Complex II-supported and ADP stimulated absolute H_2O_2 emission during OXPHOS normalized to ETC content. **H)** Responsiveness of ETC to ADP (absolute H_2O_2 emission as a percentage of maximal). n= 7-11. **CI**: Complex I, **CII**: Complex II, **CIII**: Complex III, **CIV**: Complex IV, **CV**: Complex V, **ETC**: Electron Transport Chain, **H_2O_2**: Hydrogen Peroxide. Analyses for **B, C, F** were conducted using either a standard one-way ANOVA or Kruskal-Wallis test, depending on whether data was normally distributed. Analyses for **D**, **E**, **G** and **H** were conducted using a standard two-way ANOVA. These were followed by a two-step step-up method of Benjamini, Krieger, and Yukutieli for post-hoc analysis. Results represent mean $\pm$ SEM. α = $p < 0.05$ Control vs EOC-40, β = $p < 0.05$ Control vs EOC-40-SkQ1, γ = $p < 0.05$ Control vs EOC-80, δ = < 0.05 Control vs EOC-80-SkQ1, ε = $p < 0.05$ EOC-40 vs EOC-40-SkQ1, θ = $p < 0.05$ EOC-80 vs EOC-80-SkQ1, ρ = $p < 0.05$ EOC-40 vs EOC-80, ω = EOC-40-SkQ1 vs EOC-80-SkQ1.

Ovarian cancer progressions leads to greater susceptibility to calcium-stress induced mPT and increased caspase-3/-9 activity in white gastrocnemius fibers.

Mitochondrial permeability transition (mPT) was induced via calcium stress in white gastrocnemius fibers to assess the mitochondria's ability to withstand calcium stress (calcium retention capacity) and their susceptibility to mPT. There were no differences in calcium retention capacity among any of the groups (**Fig. 8B**). However, the susceptibility of fibers to undergo mPT increased with ovarian cancer progression, with a greater number of fibers undergoing mPT in the 80-day EOC groups compared to control, indicating that ovarian cancer makes WG fibers more prone to mPT (**Fig. 8C**).

Caspase-9 and -3 activity increased 2.5-fold in the 40-day EOC groups and remained elevated in the EOC-80 group (**Fig. 8D-E**). Notably, in the EOC-80-SkQ1 group, caspase-9 and -3 activity decreased by approximately 1-fold, reaching levels comparable to Control caspase

activity. This suggests that SkQ1 helps mitigate the increased caspase activity associated with EOC progression.

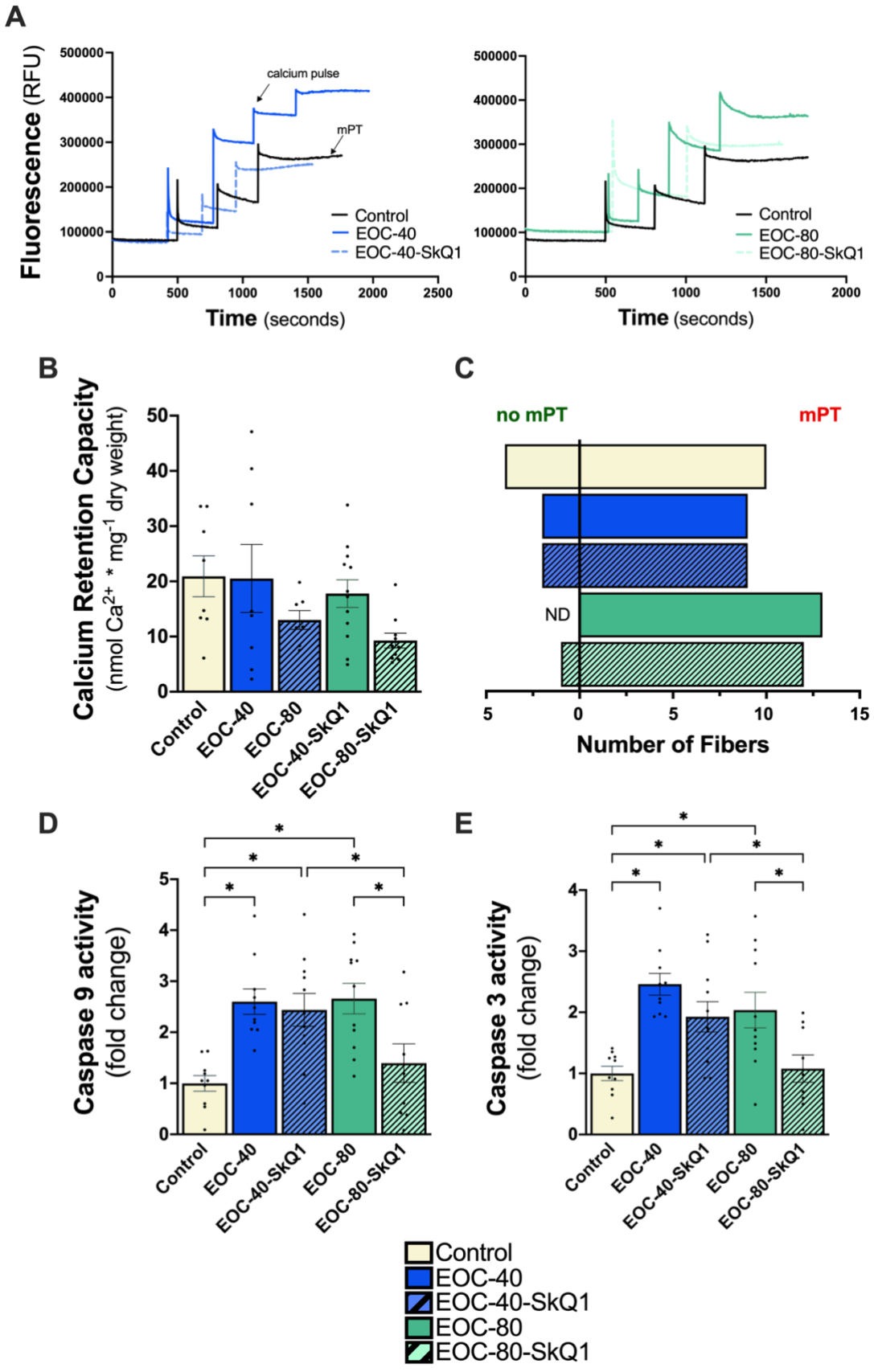
A
Fluorescence (RFU)
500000
400000
300000
200000
100000
0
calcium pulse
mPT
Control
EOC-40
EOC-40-SkQ1
0
500
1000
1500
2000
2500
Time (seconds)
Control
EOC-80
EOC-80-SkQ1
Time (seconds)
B
Calcium Retention Capacity
(nmol Ca2+ * mg-1 dry weight)
50
40
30
20
10
0
Control
EOC-40
EOC-80
EOC-40-SkQ1
EOC-80-SkQ1
C
no mPT
mPT
ND
5
0
5
10
15
Number of Fibers
D
Caspase 9 activity
(fold change)
5
4
3
2
1
0
*
Control
EOC-40
EOC-40-SkQ1
EOC-80
EOC-80-SkQ1
E
Caspase 3 activity
(fold change)
4
3
2
1
0
*
Control
EOC-40
EOC-40-SkQ1
EOC-80
EOC-80-SkQ1
Control
EOC-40
EOC-40-SkQ1
EOC-80
EOC-80-SkQ1

Figure 8. Calcium-stress induced mPT and caspase-9/-3 activity in white gastrocnemius muscles of EOC- tumour bearing mice subjected to either SkQ1 or normal drinking water. **A)** Representative traces of calcium titrations and induction of mitochondrial permeability transition (mPT) in white gastrocnemius muscles. **B)** Calcium retention capacity of white gastrocnemius fibers, n=9-13. **C)** Incidence of calcium-stress induced mPT in mixed gastrocnemius fibers (right side) vs fibers that did not exhibit mPT (left side), n=9-13. **D)** Caspase-9- and **E)** caspase-3-fold change in activity, n=9-11. **ND**: none detected. Analyses for **B, D, and E** were conducted using either a standard one-way ANOVA or Kruskal-Wallis test, depending on whether data was normally distributed. These were followed by a two-step step-up method of Benjamini, Krieger, and Yukutieli for post-hoc analysis. Results represent mean ± SEM. ***** = $p < 0.05$.

The capacity for white gastrocnemius muscle to undergo necroptosis is heightened during early ovarian cancer progression.

Protein content of total RIPK1, RIPK3, and MLKL, as well as their phosphorylated counterparts, were measured as markers of necroptosis. First, the accuracy of necroptosis antibodies was assessed using positive (C2C12 model of necroptosis, DMD tissue) and negative (RIPK3 KO tissue) controls (**SFig. 5-7**).

Total RIPK1 protein content increased in 40-day EOC groups compared to control, followed by a decrease in 80-day EOC groups compared to 40-day EOC groups, though not to control levels (**Fig. 9A**). Assessment of phosphorylated RIPK1 did not yield detectable bands in any group, leaving uncertainty about whether the increased RIPK1 total protein at 40 days corresponds to heightened activation (via phosphorylation) (**Fig. 9B**). Nevertheless, the capacity for RIPK1 activation appears heightened at 40 days with EOC.

Divergent results were observed for RIPK3 and MLKL compared to RIPK1. Total RIPK3 showed no changes among any of the groups, with a decrease in the EOC-80-SkQ1 group compared to EOC-40-SkQ1 (**Fig. 9D**). Phosphorylated RIPK3 decreased in the EOC-80 group compared to control and EOC-40, but this effect was lost when normalized to total RIPK3 content, indicating no significant differences among the groups (**Fig. 9E-F**).

For MLKL, both total and phosphorylated protein content decreased in the EOC-80-SkQ1 group compared to the EOC-40-SkQ1 group, though no differences were observed with the control group (**Fig. 9G-H**). This decrease persisted when phosphorylated MLKL was normalized to total MLKL content, suggesting a consistent reduction in MLKL activation in the EOC-80-SkQ1 group (**Fig. 9I**).

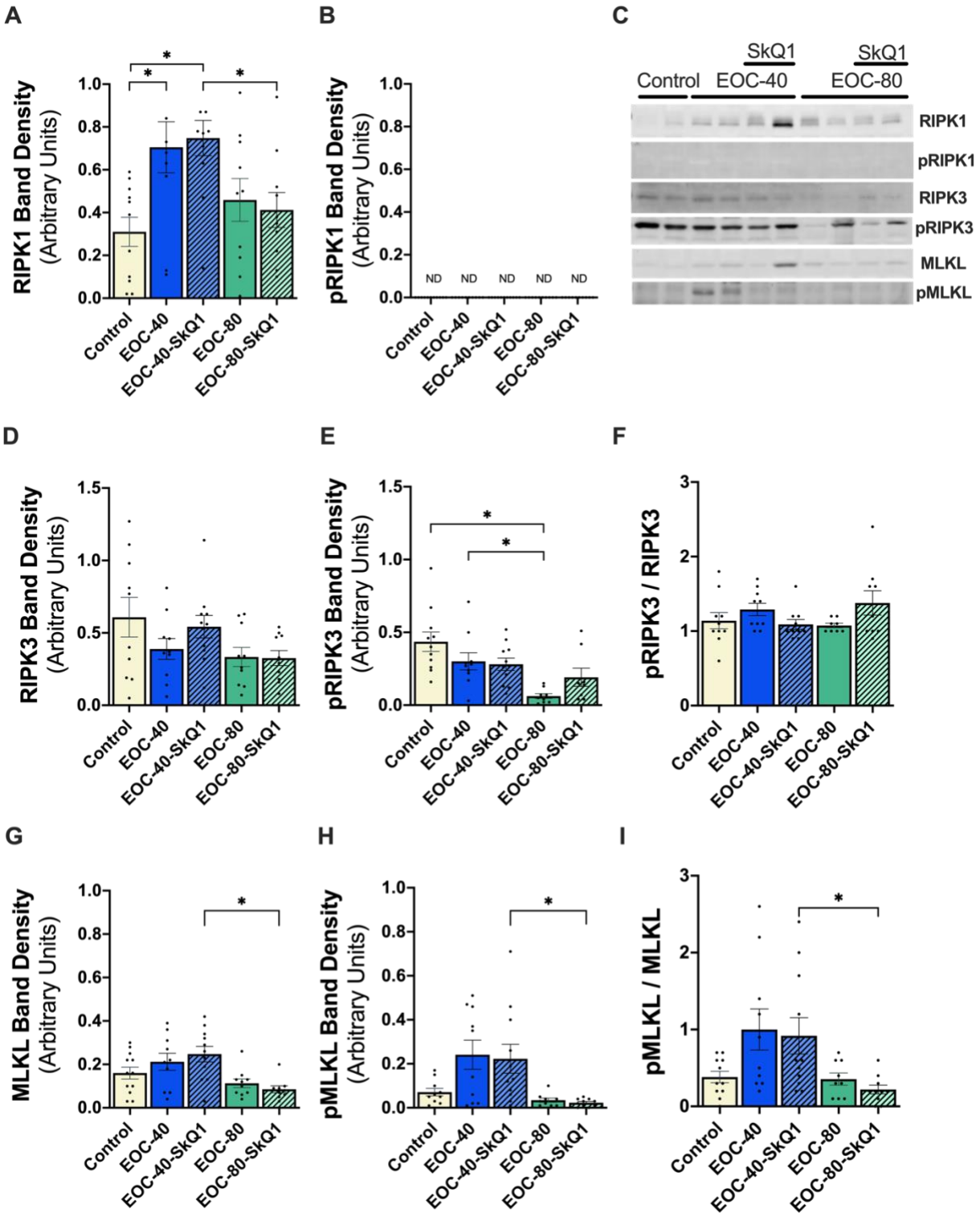
A
RIPK1 Band Density
(Arbitrary Units)
B
pRIPK1 Band Density
(Arbitrary Units)
ND
C
SkQ1
SkQ1
Control
EOC-40
EOC-80
RIPK1
pRIPK1
RIPK3
pRIPK3
MLKL
pMLKL
D
RIPK3 Band Density
(Arbitrary Units)
E
pRIPK3 Band Density
(Arbitrary Units)
F
pRIPK3 / RIPK3
G
MLKL Band Density
(Arbitrary Units)
H
pMLKL Band Density
(Arbitrary Units)
I
pMLKL / MLKL
Control
EOC-40
EOC-40-SkQ1
EOC-80
EOC-80-SkQ1

Figure 9. Assessment of necroptosis markers in white gastrocnemius muscles of EOC-tumour bearing mice subjected to either SkQ1 or normal drinking water. A) Total RIPK1 and **B)** phosphorylated- RIPK1 protein content in the white gastrocnemius muscle. **C)** Representative western blot of RIPK1, RIPK3, MLKL and their phosphorylated counterparts in white gastrocnemius muscle. **D)** Total RIPK3 and **E)** phosphorylated RIPK3 protein content in white gastrocnemius**. F)** phosphorylated RIPK3 normalized to total RIPK3 protein content**. G)** Total MLKL and **H)** phosphorylated protein content in white gastrocnemius muscle. **I)** phosphorylated MLKL normalized to total MLKL protein content. **RIPK1**: Receptor Interacting Serine/Threonine Protein Kinase 1, **RIPK3**: Receptor Interacting Serine/Threonine Protein Kinase 3, **MLKL**: Mixed-Lineage Kinase Domain-Like Protein, **pRIPK1**: phosphorylated RIPK1, **pRIPK3**: phosphorylated RIPK3, **pMLKL**: phosphorylated MLKL. **ND**: none detected. Analyses for **A**, **B**, **D**, **E**, **F**, **G** and **H** were conducted using either a standard one-way ANOVA or Kruskal-Wallis test, depending on whether data was normally distributed. These were followed by a two-step step-up method of Benjamini, Krieger, and Yukutieli for post-hoc analysis. Results represent mean $\pm$ SEM. ***** = $p < 0.05$.

CHAPTER 6. DISCUSSION

Cancer-induced cachexia significantly worsens the prognosis and quality of life for cancer patients, leading to a higher percentage of cancer-related deaths[5,6]. Due to its multifaceted nature, there is currently no standard treatment for cancer cachexia, necessitating further investigation into all plausible mechanisms underlying the syndrome[98]. Recent literature has highlighted the involvement of mitochondrial reactive oxygen species (mROS) in cancer cachexia, presenting a new avenue for exploration[9,10,50]. In this study, we assessed the role of mitochondrial hydrogen peroxide (mH_2O_2)-mediated cell death pathways—apoptosis and necroptosis—in regulating skeletal muscle mass during ovarian cancer progression. We employed an orthotopic epithelial ovarian cancer (EOC) model, which closely mimics human EOC development and metastasis[9,50]. EOC-mice were assessed at two time points, 40 days, and 80 days, to discern a timeline of changes in mH_2O_2 emission and activation of cell death pathways. Additionally, half of the EOC-tumor-bearing mice were treated with the commercially available mitochondrial-targeting antioxidant SkQ1. This treatment aimed to determine whether preventing EOC-induced mH_2O_2 emission could downregulate apoptosis and necroptosis, thereby rescuing cancer-induced atrophy and elucidating whether these cell death pathways are mechanisms driving atrophy. We hypothesized that increased mH_2O_2 with cancer progression induces apoptosis and necroptosis within myofibers, contributing to observed atrophy. Furthermore, administration of the mitochondrial-targeting antioxidant SkQ1 was expected to attenuate mH_2O_2 emission, mitigate apoptosis and necroptosis, and ultimately prevent atrophy.

First, the EOC model was characterized, revealing that EOC primary tumors grew as expected, with the 80-day EOC groups exhibiting larger tumors than the 40-day EOC groups. Additionally, the 80-day EOC mice developed ascites fluid, indicative of stage III ovarian cancer

in humans, and showed evidence of metastasis to the diaphragm, confirming that the EOC model successfully emulated human ovarian cancer. SkQ1 treatment did not affect primary tumor size, ascites development, metastasis, or overall survival, underscoring its potential benefit for skeletal muscle preservation during cancer without promoting tumor growth.

The 80-day EOC groups exhibited significant body weight loss and a reduction in inguinal fat pads, irrespective of SkQ1 treatment. Similarly, hindlimb muscle wet weights decreased in these groups, with no observable differences attributed to SkQ1 intervention. These findings confirm that the mice were cachectic by 80 days post-cancer induction. However, the absence of SkQ1-induced improvements in morphometric data contrasts with existing literature, where mitochondrial therapeutics have been shown to enhance body weight and muscle mass in pre-clinical cancer models[12–14]. These discrepancies may stem from the specific use of SkQ1 as opposed to other mitochondrial therapeutics like MitoQ and SS-31, as well as differences in cancer models, such as the C26 colorectal model versus the EOC model employed in this study.

The gastrocnemius muscle, primarily composed of type IIb fibers not present in human skeletal muscle, was chosen for this study for several reasons[99]. First, majority of apoptosis and necroptosis literature has utilized the gastrocnemius muscle, allowing for direct comparison with other studies. Second, the muscle needed to be large enough to accommodate all assays, facilitating better correlation of findings. Therefore, the discussion below is based on changes observed in the gastrocnemius muscle.

Evidence of gastrocnemius atrophy by 40-days post EOC injection.

The gold standard for assessing muscle atrophy in rodent models is the measurement of changes in muscle cross-sectional area (CSA)[100]. In this study, muscle cross-sections were stained for myosin heavy chain isoforms (MHCI, IIa, IIx, and IIb), and changes in CSA and minimum

Feret's diameter (MFD) were measured. The CSA of type IIb fibers decreased in all EOC groups, leading to an overall reduction in pooled myofiber CSA, indicating generalized atrophy in gastrocnemius fibers during EOC development. Additionally, Type IIb MFD decreased in all EOC groups, although this effect was not observed when all fiber types were pooled together. The discrepancy between pooled CSA and MFD may be due to less pronounced differences in fiber-type-specific MFDs among the groups.

MFD represents the closest possible distance between two parallel borders of the fibers. Thus, consistent pooled MFD among the groups despite changes in CSA suggests that myofibers may be atrophying by altering shape, such that the closest possible distance between two parallel borders of the fibers remains consistent. Analysis of myofiber aspect ratio, the ratio of the Minimum to the Maximum Feret Diameter, may elucidate changes in the overall shape and elongation of myofibers in future studies. Nonetheless, the present data suggest that there was general myofiber atrophy in the gastrocnemius muscles of 40-day EOC-tumor bearing mice, which persisted in 80-day tumor-bearing mice.

SkQ1 Mitigates Late-Stage EOC-Induced Reductions in Complex I and II in White Gastrocnemius.

Electron transport chain (ETC) complexes were quantified in the white gastrocnemius by measuring highly conserved subunits of each complex as an index of overall mitochondrial content. In the 80-day EOC group, protein content of complexes I and II decreased compared to the 40-day EOC group. These reductions were not observed in the 80-day EOC-SkQ1 group; instead, protein levels of complexes I and II in the EOC-80-SkQ1 group were comparable to those in the control group. This suggests that SkQ1 preserves the content of complexes I and II, specifically the NDUFB8 and SDHB subunits. The damaging effect of mROS on mitochondrial

DNA (mtDNA) is well-documented. However, since NDUFB8 and SDHB are nuclear-encoded proteins, mROS-induced mtDNA damage is not a plausible cause for the observed decrease in complexes I and II content[101,102]. Thus, though speculative, the reduction in complexes I and II observed in this study may be attributed to alterations in transcription at the nucleus, or issues in the packaging and delivery of these proteins to the mitochondria. Although this study is not equipped to pursue this topic further, it presents an interesting direction for future research.

SkQ1 attenuates* mH_2O_2 *emission in late-stage EOC white gastrocnemius.

H_2O_2 emission was assessed at specific sites within the mitochondria to identify alterations in ROS emission during cancer progression. Both complex I- and II-supported maximal H_2O_2 emissions remained unchanged across all groups. However, when ADP was titrated to create a more physiologically relevant environment for ROS generation (during oxidative phosphorylation), absolute H_2O_2 emission increased in both 80-day EOC groups compared to the control and their 40-day EOC counterparts. This suggests that ADP was less effective in suppressing electron leak and subsequent H_2O_2 emission in the 80-day EOC groups. Next, H_2O_2 data was normalized to mitochondrial content which revealed that EOC-80 mitochondria produced more H_2O_2 than EOC-80-SkQ1 mitochondria, suggesting that SkQ1 attenuated H_2O_2 production, albeit not to control levels.

These findings persist when absolute emission is expressed as a percentage of maximal emission, revealing that the heightened ROS levels in both 80-day groups are due to the electron transport chain's (ETC) responsiveness or sensitivity to ADP rather than initial H_2O_2 emission levels. The increased sensitivity to ADP in the EOC-80-SkQ1 group, compared to EOC-80, appears linked to the higher complex I and II protein content in EOC-80-SkQ1. Thus, the ability

of EOC-80-SkQ1 to attenuate H_2O_2 emission seems attributable to the preservation of complex I and II rather than SkQ1's direct antioxidant effects.

It remains unclear how EOC-80 mitochondria exhibited heightened H_2O_2 emission despite having lower levels of complex I and II. However, the inverse relationship between complex I content and H_2O_2 emission observed in this study has also been noted in complex I deficient models[103]. It is possible that complexes I and II are working harder to prevent the accumulation of substrates at these complexes and ADP at complex V, which could make the ETC more 'leaky' and prone to increased ROS production.

Interpretation of the H_2O_2 data from this study requires careful consideration. Firstly, although mitochondria in both the EOC-80 and EOC-80-SkQ1 groups emitted more H_2O_2 than control mitochondria, it remains uncertain whether this heightened emission has broad enough effects in vivo to induce significant myofiber oxidative damage. Secondly, skeletal muscles consist of distinct mitochondrial populations: subsarcolemmal (beneath the sarcolemma) and intermyofibrillar (between contractile filaments)[34]. Consequently, it is unclear if both mitochondrial populations exhibited increased ROS emission and whether proteins near the sarcolemma or myofibrils were differentially affected. Lastly, the H_2O_2 data from this study diverges from previous research, where H_2O_2 emission preceded or coincided with lower CSA[9,10,104]. This discrepancy may be attributed to the use of different models and the assessment of different skeletal muscles, as prior studies have identified heterogeneous mitochondrial responses in muscle to cancer progression.

Capacity for myofiber apoptosis increases during early-stage EOC and persists into late stage EOC.

Classical apoptosis involves a network of interconnected pathways[25]. This study specifically examines mitochondrial permeability transition (mPT) induced by mitochondrial-derived hydrogen peroxide (mH2O2), followed by apoptosome formation and caspase-3 activation, which collectively execute the apoptotic process. mPT acts as a critical gateway for the release of pro-apoptotic factors such as cytochrome *c* from the mitochondria[29,59]. Heightened mH_2O_2 emission triggers mPT and has been documented in skeletal muscle atrophy models, including denervation and aging[33,105,106]. To assess the occurrence of mPT in vivo, pmfb were subjected to incremental calcium stress as a functional assay. The results showed no differences in the calcium concentration required to induce mPT (calcium retention capacity) among the groups. However, the number of pmfb experiencing mPT increased with EOC progression. As previously mentioned, the 80-day EOC groups exhibited heightened H_2O_2 emission, which promotes mPT, thus explaining the increased number of muscle fibers undergoing mPT as EOC progressed.

Caspase-9 and caspase-3 activities were measured to further elucidate the apoptotic pathways involved. Classically, activation of caspase-9 is attributed to escape of cytochrome *c* from mitochondria and subsequent formation of the apoptosome, comprising cytochrome *c,* APAF-1 and procaspase-9[25]. Thereby, any changes in caspase-9 activity are linked to release of cytochrome *c* to the cytosol from the mitochondria. This study observed a 2.5-fold increase in caspase-9 activity in both EOC-40 groups, which remained elevated in EOC-80, indicating apoptosome formation. Although speculative, since calcium-stress-induced mPT showed no differences among the groups, cytochrome *c* escape and subsequent procaspase-9 activation may have occurred through mitochondrial outer membrane permeabilization (MOMP) rather than mPT.

This is supported by previous literature, which identified increased BAX to Bcl2 protein ratio, a marker of MOMP induction, in C26 colorectal cachectic mice[81,107].

Procaspase-3, cleaved and activated by caspase-9 and caspase-8, also showed increased activity in both EOC-40 groups, remaining elevated in EOC-80. The similar pattern between caspase-9 and caspase-3 activity suggests that caspase-3 activation may primarily result from caspase-9 activity, as a larger increase would be expected if both caspase-9 and -8 were involved. Notably, caspase-9 and -3 activities were heightened in both 40-day EOC groups, which exhibited lower cross-sectional area (CSA). While this does not denote causation, it suggests that caspase-9 and -3 activities are associated with early EOC-induced atrophy, preceding changes in H_2O_2 emission.

Interestingly, the EOC-80-SkQ1 group exhibited decreased caspase-9 and -3 activities, coinciding with reduced H_2O_2 emission. This implies that the regulation of caspase-3 and -9 activities may be linked to H_2O_2 at later EOC stages. Although elevated caspase-3 and -9 activities suggest an increased capacity for apoptosis in the white gastrocnemius muscle, it cannot be conclusively stated that apoptosis occurred. Additionally, caspase-3 activity is believed to convert myofibril proteins into substrates for the ubiquitin-proteasome system (UPS), which is consistently activated in animal models of cancer-cachexia[19,24,80,108]. Thus, an additional mechanism of atrophy in this study may be caspase-3-activated UPS.

Capacity for myofiber necroptosis increases during early-stage EOC and gradually decreases by late stage EOC.

Recent literature on the regulated cell death pathway necroptosis in skeletal muscle diseases has suggested this pathway as a regulator of cancer-induced muscle atrophy. Necroptosis involves a series of phosphorylation events from RIPK1 to RIPK3 and MLKL, leading to MLKL

oligomerization on the plasma membrane and cellular leakage[25]. RIPK3 has been demonstrated to interact with mitochondria and enhance H_2O_2 emission, which in turn oxidizes cysteine residues on RIPK1 inducing its autophosphorylation, thereby establishing a positive feedback loop[39,40]. To investigate necroptosis as a mechanism of EOC-induced atrophy, markers of necroptosis were assessed in the white gastrocnemius tissue.

Analysis of RIPK1 total protein levels revealed an increase in the EOC-40 groups, which subsequently decreased in the EOC-80 groups. However, RIPK1 phosphorylation was undetectable across all groups, which may be attributed to limitations of the antibody used rather than a true absence of phosphorylation. The antibody was validated using a C2C12 necroptosis model and dystrophin-deficient (DMD) tissue, both known to exhibit necroptosis according to existing literature[44,86]. While the antibody detected phosphorylation in C2C12 cells, it failed to do so in DMD quadriceps and gastrocnemius tissues, suggesting its insufficient sensitivity for detecting RIPK1 phosphorylation in skeletal muscle. Despite this, the elevated total RIPK1 protein levels in the EOC-40 groups imply an increased capacity for necroptosis in gastrocnemius fibers. It is important to note that RIPK1 is a key regulator in multiple pathways, including apoptosis, necroptosis, and NF-κB signaling[25,70]. Consequently, an increase in RIPK1 protein content could potentially enhance activity in any of these pathways. The observed decrease in RIPK1 content in the EOC-80 groups may be due to either reduced synthesis or increased cleavage of RIPK1, influenced by the formation of cell death complexes (complex IIa or IIb) in response to extrinsic stimuli.

RIPK3 and MLKL present a contrasting pattern compared to RIPK1. While the total protein content of RIPK3 remained unchanged across all groups, a notable decrease in RIPK3 phosphorylation was observed in the EOC-80 group relative to the control and EOC-40 groups.

However, this difference in phosphorylated RIPK3 disappeared when normalized to total RIPK3 content. In contrast, significant reductions in both total and phosphorylated MLKL were evident in the EOC-80-SkQ1 group compared to the EOC-40-SkQ1 group, which persisted even after normalizing phosphorylated MLKL to total protein content.

Previous studies on bone marrow-derived macrophages and mouse embryonic fibroblasts have demonstrated that RIPK3 and MLKL are consistently expressed within cells, with their phosphorylation occurring in a sequential, time-dependent manner: MLKL phosphorylation follows RIPK3 phosphorylation, which in turn follows RIPK1 phosphorylation[109,110]. The observed depletion of total MLKL protein with tumor progression, in contrast to control, appears to be a distinctive feature of cancer-induced muscle atrophy. Moreover, the initial increase in total RIPK1 at 40 days post-EOC onset, followed by a gradual decline in both MLKL content and phosphorylation as EOC progresses, contrasts existing literature. This pattern suggests that these markers may have been elevated even earlier than 40 days with EOC and that they decline as EOC progresses, presenting a compelling avenue for future research.

Given that mH_2O_2 can oxidize several cysteines on RIPK1, promoting its autophosphorylation and subsequent necrosome formation, it was anticipated that markers of necroptosis and their activation would be elevated during heightened H_2O_2 emission, with SkQ1 reducing this effect[40]. However, elevated necroptosis activation via phosphorylation of RIPK1, RIPK3, and MLKL was not observed at 80 days with EOC, nor did SkQ1 attenuate the phosphorylation of these markers despite reducing H_2O_2 emission. The lack of effect of H_2O_2 on necroptosis markers at 80 days with EOC may be attributed to the lower total expression of these proteins. Additionally, the unique morphology of skeletal muscle and the distinct mitochondrial

locations might have contributed, as RIPK1 may not have been physically close enough to the mitochondria for H_2O_2 to oxidize it.

CHAPTER 7. CONCLUSION AND FUTURE DIRECTIONS

With the identification of novel regulated cell death pathways in skeletal muscle diseases and the observation of increased mitochondrial ROS emission in cancer-induced muscle atrophy, we aimed to explore mROS-regulated cell death pathways, particularly apoptosis and necroptosis, as mechanisms driving skeletal muscle atrophy during cancer progression[5,6,32,36,37]. We initially hypothesized that enhanced mH_2O_2 emission associated with cancer progression induces apoptosis and necroptosis within myofibers, contributing to the observed muscle atrophy. Furthermore, we proposed that administering the mitochondrial-targeting antioxidant SkQ1 would reduce mH_2O_2 emission, thereby attenuating regulated cell death pathways and preventing atrophy.

To our knowledge, this is the first study to evaluate the commercially available mitochondrial-targeting antioxidant SkQ1 as a treatment for cancer-induced muscle atrophy. Surprisingly, we observed that myofiber cross-sectional area (CSA) decreased before any significant changes in mH_2O_2 emission, which contrasts with existing literature where elevated mH_2O_2 emission typically coincides with or precedes muscle atrophy[5,6,37]. Consequently, despite SkQ1's beneficial effects on mH_2O_2 emission, it did not mitigate the reduction in myofiber CSA, diverging from previous findings[7–9]. The discrepancies between our results and earlier studies may be attributed to differences in the specific skeletal muscles investigated, the cancer models used, and the ROS antioxidants and inhibitors applied. Future research should focus on assessing the efficacy of various mitochondrial therapeutics in cancer-induced atrophy, using consistent muscle and cancer models for comparative analysis.

This study is notable for being among the few to investigate apoptosis and the first to examine necroptosis in the skeletal muscle of cancer cachectic mice. We observed increased levels of both apoptosis markers (mPT, caspase-9, and caspase-3 activity) and necroptosis markers

(RIPK1, RIPK3, MLKL, and their phosphorylated forms) during early-stage EOC, which coincided with a reduction in myofiber cross-sectional area (CSA). Interestingly, while markers of necroptosis decreased from 40 to 80 days of EOC, markers of apoptosis remained elevated. This persistent activation of apoptosis may contribute to the downregulation of necroptosis markers, given the mutually exclusive nature of these cell death pathways. Although this study lays important groundwork for understanding regulated cell death (RCD) mechanisms in cancer-induced muscle atrophy, it does not fully ascertain whether these RCD pathways are executed in the white gastrocnemius. Future research should expand on this foundation by exploring additional RCD pathways, such as ferroptosis and pyroptosis, and by investigating earlier time points in tumor progression[38,39]. It is also crucial to investigate the terminal events associated with each RCD pathway to accurately determine myofiber commitment to either processes. This study was limited in this regard, as commonly used assays, such as TUNEL staining, do not differentiate between apoptosis and necroptosis[40].

In response to the growing demand for more orthotopic cancer models, this study represents the first evaluation of a mitochondrial ROS therapeutic within such a model. Although this study concentrated on muscle mass preservation by SkQ1, it did not assess impact on muscle functionality. Thus, a critical future direction is to evaluate the effect of SkQ1 on muscle function during tumour-development.

Cancer-induced muscle loss, or cachexia, significantly impairs quality of life, exacerbates prognosis, and diminishes treatment efficacy, contributing to approximately 30% of cancer-related deaths worldwide[2,41]. Despite its high prevalence, affecting around 70% of cancer patients, cachexia lacks a standardized care approach due to its complex nature. Therefore, it is essential and urgent to investigate all potential mechanisms underlying cancer-induced atrophy to develop

novel therapeutic strategies. This study provides a crucial foundation for future research into regulated cell death pathways as mechanisms of cancer-induced atrophy.

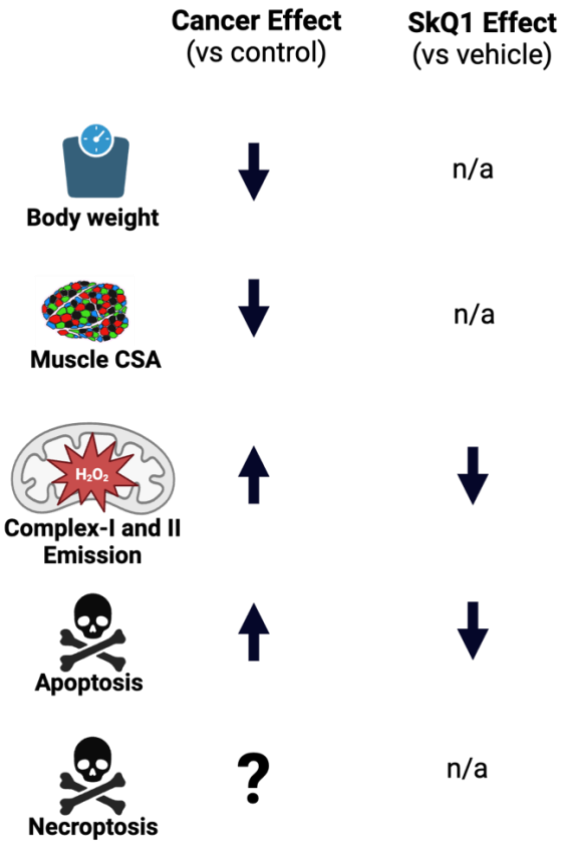

Figure 10. Summary of findings. "↑" represents increase, "↓" represents decrease, "?" represents inconclusive findings, n/a represents no changes due to SkQ1.

REFERENCES

1. Martin, L. *et al.* Cancer cachexia in the age of obesity: Skeletal muscle depletion is a powerful prognostic factor, independent of body mass index. *Journal of Clinical Oncology* **31**, 1539–1547 (2013).
2. Fearon, K. *et al.* Definition and classification of cancer cachexia: an international consensus. *Lancet Oncol* **12**, 489–495 (2011).
3. Aust, S. *et al.* Skeletal Muscle Depletion and Markers for Cancer Cachexia Are Strong Prognostic Factors in Epithelial Ovarian Cancer. *PLoS One* **10**, e0140403 (2015).
4. Cheong, I. Y. *et al.* Functional loss in daily activity in ovarian cancer patients undergoing chemotherapy. *Arch Gynecol Obstet* **299**, 1063–1069 (2019).
5. Poisson, J. *et al.* Prevalence and prognostic impact of cachexia among older patients with cancer: a nationwide cross-sectional survey (NutriAgeCancer). *J Cachexia Sarcopenia Muscle* **12**, 1477 (2021).
6. Prado, C. M. M. *et al.* Sarcopenia as a determinant of chemotherapy toxicity and time to tumor progression in metastatic breast cancer patients receiving capecitabine treatment. *Clinical Cancer Research* **15**, 2920–2926 (2009).
7. Van Vledder, M. G. *et al.* Body composition and outcome in patients undergoing resection of colorectal liver metastases. *Br J Surg* **99**, 550–557 (2012).
8. Fearon, K. C. H., Glass, D. J. & Guttridge, D. C. Cancer Cachexia: Mediators, Signaling, and Metabolic Pathways. *Cell Metab* **16**, 153–166 (2012).
9. Delfinis, L. J. *et al.* Muscle weakness and mitochondrial stress occur before severe metastasis in a novel mouse model of ovarian cancer cachexia. *Mol Metab* **86**, 101976 (2024).
10. Delfinis, L. J. *et al.* Muscle weakness precedes atrophy during cancer cachexia and is linked to muscle-specific mitochondrial stress. *JCI Insight* (2022) doi:10.1172/JCI.INSIGHT.155147.
11. Brown, J. L. *et al.* Mitochondrial degeneration precedes the development of muscle atrophy in progression of cancer cachexia in tumour-bearing mice. *J Cachexia Sarcopenia Muscle* **8**, 926 (2017).
12. Smuder, A. J. *et al.* Pharmacological targeting of mitochondrial function and reactive oxygen species production prevents colon 26 cancer-induced cardiorespiratory muscle weakness. *Oncotarget* **11**, 3502 (2020).
13. Ballarò, R. *et al.* Targeting Mitochondria by SS-31 Ameliorates the Whole Body Energy Status in Cancer- and Chemotherapy-Induced Cachexia. *Cancers 2021, Vol. 13, Page 850* **13**, 850 (2021).
14. Pin, F., Huot, J. R. & Bonetto, A. The Mitochondria-Targeting Agent MitoQ Improves Muscle Atrophy, Weakness and Oxidative Metabolism in C26 Tumor-Bearing Mice. *Front Cell Dev Biol* **10**, 861622 (2022).
15. Min, K. *et al.* Mitochondrial-targeted antioxidants protect skeletal muscle against immobilization-induced muscle atrophy. *J Appl Physiol* **111**, 1459–1466 (2011).
16. Powers, S. K. *et al.* Mitochondria-targeted antioxidants protect against mechanical ventilation-induced diaphragm weakness. *Crit Care Med* **39**, 1749–1759 (2011).
17. Lian, D., Chen, M. M., Wu, H., Deng, S. & Hu, X. The Role of Oxidative Stress in Skeletal Muscle Myogenesis and Muscle Disease. *Antioxidants* **11**, (2022).

18. Bock, F. J. & Tait, S. W. G. Mitochondria as multifaceted regulators of cell death. *Nature Reviews Molecular Cell Biology 2019 21:2* **21**, 85–100 (2019).
19. White, J. P. *et al.* The Regulation of Skeletal Muscle Protein Turnover during the Progression of Cancer Cachexia in the ApcMin/+ Mouse. *PLoS One* **6**, e24650 (2011).
20. Murton, A. J. *et al.* Consequences of Late-Stage Non–Small-Cell Lung Cancer Cachexia on Muscle Metabolic Processes. *Clin Lung Cancer* **18**, e1–e11 (2017).
21. Schmitt, T. L. *et al.* Activity of the Akt-dependent anabolic and catabolic pathways in muscle and liver samples in cancer-related cachexia. *J Mol Med* **85**, 647–654 (2007).
22. D'Orlando, C. *et al.* Gastric cancer does not affect the expression of atrophy-related genes in human skeletal muscle. *Muscle Nerve* **49**, 528–533 (2014).
23. Puig-Vilanova, E. *et al.* Oxidative stress, redox signaling pathways, and autophagy in cachectic muscles of male patients with advanced COPD and lung cancer. *Free Radic Biol Med* **79**, 91–108 (2015).
24. Nissinen, T. A. *et al.* Treating cachexia using soluble ACVR2B improves survival, alters mTOR localization, and attenuates liver and spleen responses. *J Cachexia Sarcopenia Muscle* **9**, 514–529 (2018).
25. Galluzzi, L. *et al.* Molecular mechanisms of cell death: recommendations of the Nomenclature Committee on Cell Death 2018. *Cell Death & Differentiation 2018 25:3* **25**, 486–541 (2018).
26. Lerner, L. *et al.* MAP3K11/GDF15 axis is a critical driver of cancer cachexia. *J Cachexia Sarcopenia Muscle* **7**, 467–482 (2016).
27. Lerner, L. *et al.* Plasma growth differentiation factor 15 is associated with weight loss and mortality in cancer patients. *J Cachexia Sarcopenia Muscle* **6**, 317–324 (2015).
28. Bonetto, A. *et al.* STAT3 Activation in Skeletal Muscle Links Muscle Wasting and the Acute Phase Response in Cancer Cachexia. *PLoS One* **6**, e22538 (2011).
29. Bonora, M., Giorgi, C. & Pinton, P. Molecular mechanisms and consequences of mitochondrial permeability transition. *Nature Reviews Molecular Cell Biology 2021 23:4* **23**, 266–285 (2021).
30. Schwartz, L. M. Skeletal Muscles Do Not Undergo Apoptosis During Either Atrophy or Programmed Cell Death-Revisiting the Myonuclear Domain Hypothesis. *Front Physiol* **9**, (2018).
31. McMillan, E. M. & Quadrilatero, J. Differential apoptosis-related protein expression, mitochondrial properties, proteolytic enzyme activity, and DNA fragmentation between skeletal muscles. *Am J Physiol Regul Integr Comp Physiol* **300**, 531–543 (2011).
32. Dam, A. D., Mitchell, A. S., Rush, J. W. E. & Quadrilatero, J. Elevated skeletal muscle apoptotic signaling following glutathione depletion. *Apoptosis* **17**, 48–60 (2012).
33. Skinner, S. K. *et al.* Mitochondrial Permeability Transition Causes Mitochondrial Reactive Oxygen Species- and Caspase 3-Dependent Atrophy of Single Adult Mouse Skeletal Muscle Fibers. *Cells* **10**, (2021).
34. Adhihetty, P. J., Ljubicic, V. & Hood, D. A. Effect of chronic contractile activity on SS and IMF mitochondrial apoptotic susceptibility in skeletal muscle. *Am J Physiol Endocrinol Metab* **292**, 748–755 (2007).
35. de Castro, G. S. *et al.* Human Cachexia Induces Changes in Mitochondria, Autophagy and Apoptosis in the Skeletal Muscle. *Cancers (Basel)* **11**, (2019).
36. Busquets, S. *et al.* Apoptosis is present in skeletal muscle of cachectic gastro-intestinal cancer patients. *Clinical Nutrition* **26**, 614–618 (2007).

37. Khoury, M. K., Gupta, K., Franco, S. R. & Liu, B. Necroptosis in the Pathophysiology of Disease. *American Journal of Pathology* vol. 190 272–285 Preprint at https://doi.org/10.1016/j.ajpath.2019.10.012 (2020).
38. Chu, Q., Gu, X., Zheng, Q., Wang, J. & Zhu, H. Mitochondrial Mechanisms of Apoptosis and Necroptosis in Liver Diseases. *Analytical Cellular Pathology* **2021**, (2021).
39. Yang, Z. *et al.* RIP3 targets pyruvate dehydrogenase complex to increase aerobic respiration in TNF-induced necroptosis. *Nature Cell Biology 2018 20:2* **20**, 186–197 (2018).
40. Zhang, Y. *et al.* RIP1 autophosphorylation is promoted by mitochondrial ROS and is essential for RIP3 recruitment into necrosome. *Nat Commun* **8**, (2017).
41. Morgan, M. J. & Kim, Y. S. Roles of RIPK3 in necroptosis, cell signaling, and disease. *Experimental & Molecular Medicine 2022 54:10* **54**, 1695–1704 (2022).
42. Newton, K. *et al.* Activity of protein kinase RIPK3 determines whether cells die by necroptosis or apoptosis. *Science (1979)* **343**, 1357–1360 (2014).
43. Kamiya, M. *et al.* Targeting necroptosis in muscle fibers ameliorates inflammatory myopathies. *Nat Commun* **13**, (2022).
44. Morgan, J. E. *et al.* Necroptosis mediates myofibre death in dystrophin-deficient mice. *Nature Communications 2018 9:1* **9**, 1–10 (2018).
45. Dubuisson, N. *et al.* The Adiponectin Receptor Agonist, ALY688: A Promising Therapeutic for Fibrosis in the Dystrophic Muscle. *Cells* **12**, (2023).
46. Peng, Q. L. *et al.* Contribution of Necroptosis to Myofiber Death in Idiopathic Inflammatory Myopathies. *Arthritis & Rheumatology* **74**, 1048–1058 (2022).
47. Li, L., Wazir, J., Huang, Z., Wang, Y. & Wang, H. A Comprehensive Review of Animal Models for Cancer Cachexia: Implications for Translational Research. *Genes Dis* 101080 (2023) doi:10.1016/J.GENDIS.2023.101080.
48. Deboer, M. D. Animal models of anorexia and cachexia. *Expert Opin Drug Discov* **4**, 1145 (2009).
49. Luan, Y. *et al.* Development of ovarian tumour causes significant loss of muscle and adipose tissue: a novel mouse model for cancer cachexia study. *J Cachexia Sarcopenia Muscle* **13**, 1289 (2022).
50. Ogilvie, L. M. *et al.* Cardiac atrophy, dysfunction, and metabolic impairments: a cancer-induced heart failure phenotype. *bioRxiv* 2023.09.30.560250 (2023) doi:10.1101/2023.09.30.560250.
51. Martin, A., Gallot, Y. S. & Freyssenet, D. Molecular mechanisms of cancer cachexia-related loss of skeletal muscle mass: data analysis from preclinical and clinical studies. *J Cachexia Sarcopenia Muscle* **14**, 1150 (2023).
52. Murphy, K. T., Struk, A., MalcontentiéWilson, C., Christophi, C. & Lynch, G. S. Physiological characterization of a mouse model of cachexia in colorectal liver metastases. *Am J Physiol Regul Integr Comp Physiol* **304**, 854–864 (2013).
53. Setiawan, T. *et al.* Cancer cachexia: molecular mechanisms and treatment strategies. *Journal of Hematology & Oncology 2023 16:1* **16**, 1–26 (2023).
54. Williams, J. P. *et al.* Effect of tumor burden and subsequent surgical resection on skeletal muscle mass and protein turnover in colorectal cancer patients. *Am J Clin Nutr* **96**, 1064–1070 (2012).
55. Tiidus, P. M., Tupling, A. R., Houston, M. E. & Houston, M. E. Biochemistry primer for exercise science. 299 (2012).

56. Sies, H. & Jones, D. P. Reactive oxygen species (ROS) as pleiotropic physiological signalling agents. *Nature Reviews Molecular Cell Biology 2020 21:7* **21**, 363–383 (2020).
57. Brand, M. D. The sites and topology of mitochondrial superoxide production. *Exp Gerontol* **45**, 466–472 (2010).
58. Suh, D. H., Kim, M. K., Kim, H. S., Chung, H. H. & Song, Y. S. Mitochondrial permeability transition pore as a selective target for anti-cancer therapy. *Front Oncol* **3**, (2013).
59. Rasola, A. & Bernardi, P. Mitochondrial permeability transition in Ca(2+)-dependent apoptosis and necrosis. *Cell Calcium* **50**, 222–233 (2011).
60. Kinnally, K. W. & Antonsson, B. A tale of two mitochondrial channels, MAC and PTP, in apoptosis. *Apoptosis* **12**, 857–868 (2007).
61. Bernardi, S. *et al.* Sex Differences in Proatherogenic Cytokine Levels. *Int J Mol Sci* **21**, (2020).
62. Jiang, Q. *et al.* Mitochondria-Targeted Antioxidants: A Step towards Disease Treatment. *Oxid Med Cell Longev* **2020**, (2020).
63. Zhu, Y. *et al.* SS-31, a Mitochondria-Targeting Peptide, Ameliorates Kidney Disease. *Oxid Med Cell Longev* **2022**, (2022).
64. Ježek, J., Engstová, H. & Ježek, P. Antioxidant mechanism of mitochondria-targeted plastoquinone SkQ1 is suppressed in aglycemic HepG2 cells dependent on oxidative phosphorylation. *Biochimica et Biophysica Acta (BBA) - Bioenergetics* **1858**, 750–762 (2017).
65. Titova, E. *et al.* Mitochondria-targeted antioxidant SkQ1 suppresses fibrosarcoma and rhabdomyosarcoma tumour cell growth. *Cell Cycle* **17**, 1797–1811 (2018).
66. Agapova, L. S. *et al.* Mitochondria-targeted plastoquinone derivatives as tools to interrupt execution of the aging program. 3. Inhibitory effect of SkQ1 on tumor development from p53-deficient cells. *Biochemistry (Moscow)* **73**, 1300–1316 (2008).
67. Dobrowolny, G. *et al.* Skeletal Muscle Is a Primary Target of SOD1G93A-Mediated Toxicity (DOI:10.1016/j.cmet.2008.09.002). *Cell Metab* **9**, 110 (2009).
68. Sethi, J. K. & Hotamisligil, G. S. Metabolic Messengers: tumour necrosis factor. *Nature Metabolism 2021 3:10* **3**, 1302–1312 (2021).
69. Jang, D. I. *et al.* The Role of Tumor Necrosis Factor Alpha (TNF-α) in Autoimmune Disease and Current TNF-α Inhibitors in Therapeutics. *Int J Mol Sci* **22**, 1–16 (2021).
70. Roberts, J. Z., Crawford, N. & Longley, D. B. The role of Ubiquitination in Apoptosis and Necroptosis. *Cell Death Differ* **29**, 272 (2022).
71. Fink, S. L. & Cookson, B. T. Apoptosis, Pyroptosis, and Necrosis: Mechanistic Description of Dead and Dying Eukaryotic Cells. *Infect Immun* **73**, 1907 (2005).
72. McIlwain, D. R., Berger, T. & Mak, T. W. Caspase Functions in Cell Death and Disease. *Cold Spring Harb Perspect Biol* **5**, 1–28 (2013).
73. Qian, S. *et al.* The role of BCL-2 family proteins in regulating apoptosis and cancer therapy. *Front Oncol* **12**, (2022).
74. Korsmeyer, S. J. *et al.* Pro-apoptotic cascade activates BID, which oligomerizes BAK or BAX into pores that result in the release of cytochrome c. *Cell Death & Differentiation 2000 7:12* **7**, 1166–1173 (2000).
75. Murphy, K. M., Ranganathan, V., Farnsworth, M. L., Kavallaris, M. & Lock, R. B. Bcl-2 inhibits Bax translocation from cytosol to mitochondria during drug-induced apoptosis of human tumor cells. *Cell Death & Differentiation 2000 7:1* **7**, 102–111 (2000).

76. Kim, J. J., Lee, S. B., Park, J. K. & Yoo, Y. D. TNF-α-induced ROS production triggering apoptosis is directly linked to Romo1 and Bcl-XL. *Cell Death & Differentiation 2010 17:9* **17**, 1420–1434 (2010).
77. Renatus, M., Stennicke, H. R., Scott, F. L., Liddington, R. C. & Salvesen, G. S. Dimer formation drives the activation of the cell death protease caspase 9. *Proceedings of the National Academy of Sciences* **98**, 14250–14255 (2001).
78. Würstle, M. L., Laussmann, M. A. & Rehm, M. The central role of initiator caspase-9 in apoptosis signal transduction and the regulation of its activation and activity on the apoptosome. *Exp Cell Res* **318**, 1213–1220 (2012).
79. Spangenburg, E. E. & Booth, F. W. Molecular regulation of individual skeletal muscle fibre types. *Acta Physiol Scand* **178**, 413–424 (2003).
80. Du, J. *et al.* Activation of caspase-3 is an initial step triggering accelerated muscle proteolysis in catabolic conditions. *J Clin Invest* **113**, 115 (2004).
81. Baltgalvis, K. A. *et al.* Activity level, apoptosis, and development of cachexia in Apc Min/+ mice. *J Appl Physiol* **109**, 1155–1161 (2010).
82. Belizário, J. E., Lorite, M. J. & Tisdale, M. J. Cleavage of caspases-1, -3, -6, -8 and -9 substrates by proteases in skeletal muscles from mice undergoing cancer cachexia. *British Journal of Cancer 2001 84:8* **84**, 1135–1140 (2001).
83. Samson, A. L. *et al.* MLKL trafficking and accumulation at the plasma membrane control the kinetics and threshold for necroptosis. *Nat Commun* **11**, (2020).
84. Rodriguez, D. A. *et al.* Characterization of RIPK3-mediated phosphorylation of the activation loop of MLKL during necroptosis. *Cell Death Differ* **23**, 76 (2016).
85. Wang, H. *et al.* Mixed lineage kinase domain-like protein MLKL causes necrotic membrane disruption upon phosphorylation by RIP3. *Mol Cell* **54**, 133–146 (2014).
86. Kim, T. Y., Kang, J. H., Lee, S. Bin, Kang, T. B. & Lee, K. H. Down-regulation of pro-necroptotic molecules blunts necroptosis during myogenesis. *Biochem Biophys Res Commun* **557**, 33–39 (2021).
87. Peng, Q. L. *et al.* Contribution of Necroptosis to Myofiber Death in Idiopathic Inflammatory Myopathies. *Arthritis & Rheumatology* **74**, 1048–1058 (2022).
88. Brown, J. L. *et al.* Mitochondrial degeneration precedes the development of muscle atrophy in progression of cancer cachexia in tumour-bearing mice. *J Cachexia Sarcopenia Muscle* **8**, 926 (2017).
89. Wang, S. *et al.* The regulatory role and therapeutic application of pyroptosis in musculoskeletal diseases. *Cell Death Discovery 2022 8:1* **8**, 1–17 (2022).
90. Halle, J. L. *et al.* Tissue-specific dysregulation of mitochondrial respiratory capacity and coupling control in colon-26 tumor-induced cachexia. *Am J Physiol Regul Integr Comp Physiol* **317**, R68–R82 (2019).
91. Brown, J. L. *et al.* Mitochondrial degeneration precedes the development of muscle atrophy in progression of cancer cachexia in tumour-bearing mice. *J Cachexia Sarcopenia Muscle* **8**, 926 (2017).
92. Tomasin, R. *et al.* Metastasis and cachexia: alongside in clinics, but not so in animal models. *J Cachexia Sarcopenia Muscle* **10**, 1183–1194 (2019).
93. Anisimov, V. N. *et al.* Effects of the mitochondria-targeted antioxidant SkQ1 on lifespan of rodents. *Aging (Albany NY)* **3**, 1110 (2011).

94. Fedorov, A. V. *et al.* Mitochondria-Targeted Antioxidant SkQ1 Prevents the Development of Experimental Colitis in Mice and Impairment of the Barrier Function of the Intestinal Epithelium. *Cells* **11**, (2022).
95. Bellissimo, C. A. *et al.* Mitochondrial creatine sensitivity is lost in the D2.mdx model of Duchenne muscular dystrophy and rescued by the mitochondrial-enhancing compound Olesoxime. *Am J Physiol Cell Physiol* **324**, C1141–C1157 (2023).
96. Hughes, M. C. *et al.* Early myopathy in Duchenne muscular dystrophy is associated with elevated mitochondrial H2 O2 emission during impaired oxidative phosphorylation. *J Cachexia Sarcopenia Muscle* **10**, 643–661 (2019).
97. Gan, I. *et al.* Mitochondrial permeability regulates cardiac endothelial cell necroptosis and cardiac allograft rejection. *American Journal of Transplantation* **19**, 686–698 (2019).
98. Roeland, E. J. *et al.* Management of cancer cachexia: ASCO guideline. *Journal of Clinical Oncology* **38**, 2438–2453 (2020).
99. Bloemberg, D. & Quadrilatero, J. Rapid determination of myosin heavy chain expression in rat, mouse, and human skeletal muscle using multicolor immunofluorescence analysis. *PLoS One* **7**, (2012).
100. Stokes, T. *et al.* Methodological considerations for and validation of the ultrasonographic determination of human skeletal muscle hypertrophy and atrophy. *Physiol Rep* **9**, (2021).
101. Bezawork-Geleta, A., Rohlena, J., Dong, L., Pacak, K. & Neuzil, J. Mitochondrial Complex II: At the Crossroads. *Trends Biochem Sci* **42**, 312 (2017).
102. Agip, A. N. A. *et al.* Cryo-EM structures of complex I from mouse heart mitochondria in two biochemically defined states. *Nature Structural & Molecular Biology 2018 25:7* **25**, 548–556 (2018).
103. Verkaart, S. *et al.* Superoxide production is inversely related to complex I activity in inherited complex I deficiency. *Biochimica et Biophysica Acta (BBA) - Molecular Basis of Disease* **1772**, 373–381 (2007).
104. Brown, J. L. *et al.* Mitochondrial degeneration precedes the development of muscle atrophy in progression of cancer cachexia in tumour-bearing mice. *J Cachexia Sarcopenia Muscle* **8**, 926 (2017).
105. Hepple, R. T. Impact of aging on mitochondrial function in cardiac and skeletal muscle. *Free Radic Biol Med* **98**, 177–186 (2016).
106. Csukly, K. *et al.* Muscle denervation promotes opening of the permeability transition pore and increases the expression of cyclophilin D. *Journal of Physiology* **574**, 319–327 (2006).
107. Wang, Q. *et al.* Combined treatment of carfilzomib and z-VAD-fmk inhibits skeletal proteolysis and apoptosis and ameliorates cancer cachexia. *Medical Oncology* **32**, 1–10 (2015).
108. Wang, X. H. *et al.* Caspase-3 cleaves specific 19 S proteasome subunits in skeletal muscle stimulating proteasome activity. *Journal of Biological Chemistry* **285**, 21249–21257 (2010).
109. Meng, L., Jin, W. & Wang, X. RIP3-mediated necrotic cell death accelerates systematic inflammation and mortality. *Proc Natl Acad Sci U S A* **112**, 11007–11012 (2015).
110. Yoon, S., Kovalenko, A., Bogdanov, K. & Wallach, D. MLKL, the Protein that Mediates Necroptosis, Also Regulates Endosomal Trafficking and Extracellular Vesicle Generation. *Immunity* **47**, 51-65.e7 (2017).

111. Bertheloot, D., Latz, E. & Franklin, B. S. Necroptosis, pyroptosis and apoptosis: an intricate game of cell death. *Cell Mol Immunol* **18**, 1106–21 (2021).
112. Kari, S. *et al.* Programmed cell death detection methods: a systematic review and a categorical comparison. *Apoptosis* **27**, 482 (2022).
113. Fearon, K. C. H., Glass, D. J. & Guttridge, D. C. Cell Metabolism Review Cancer Cachexia: Mediators, Signaling, and Metabolic Pathways. (2012) doi:10.1016/j.cmet.2012.06.011.

SUPPLEMENTAL FIGURES

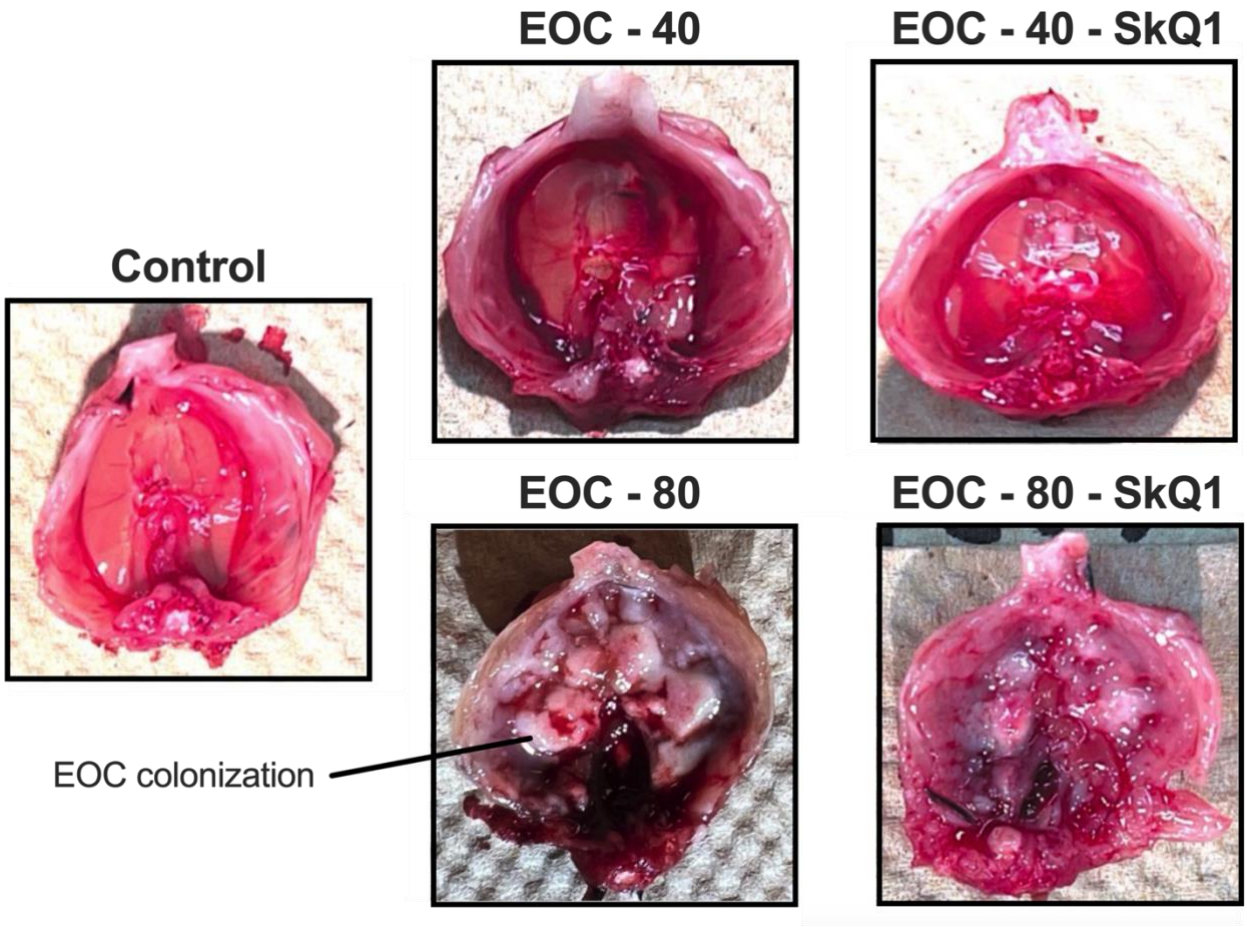

Supplemental Figure 1. Inferior view of diaphragm muscle from ovarian tumour bearing mice. White areas on the diaphragm are populations of invading EOC cells.

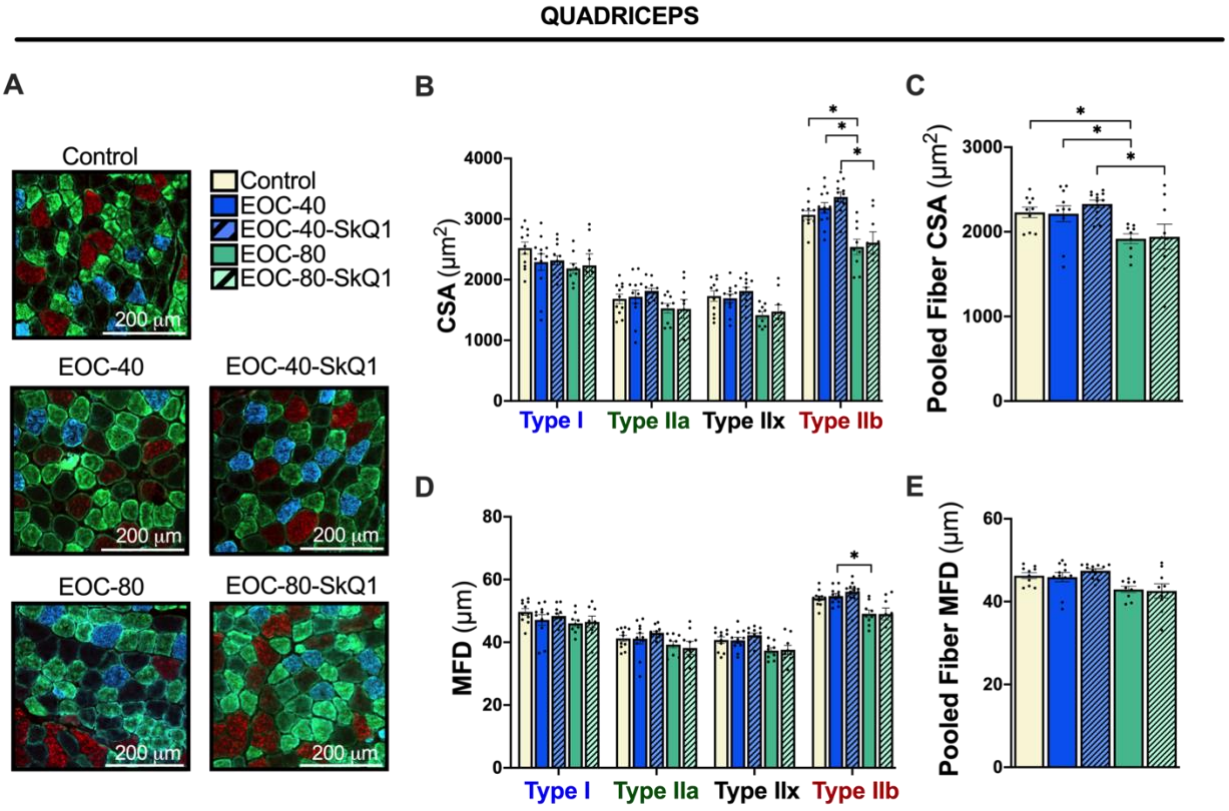

Supplemental Figure 2. Quadricep atrophy with EOC progression. A) Representative images of quadricep cross-sections stained for myosin heavy chain (MHC) isoforms. Blue corresponds to type I fibers, green: type IIa, black: type IIx, and red: type IIb fibers. n= 12 – 26. **B)** Cross-sectional area (CSA) of quadriceps muscle fibers, n=9 -12. **C)** Pooled quadriceps muscle fiber CSA. n=9-12. **D)** Minimal-feret diameter (MFD) of quadriceps muscle fibers and **E)** pooled MFD of quadriceps fibers. n = 9-12. Analyses for **B**, **C**, **D**, and **E** were conducted using either a standard one-way ANOVA or Kruskal-Wallis test, depending on whether data was normally distributed. These were followed by a two-step step-up method of Benjamini, Krieger, and Yukutieli for post-hoc analysis. Results represent mean ± SEM. ***** = $p < 0.05$.

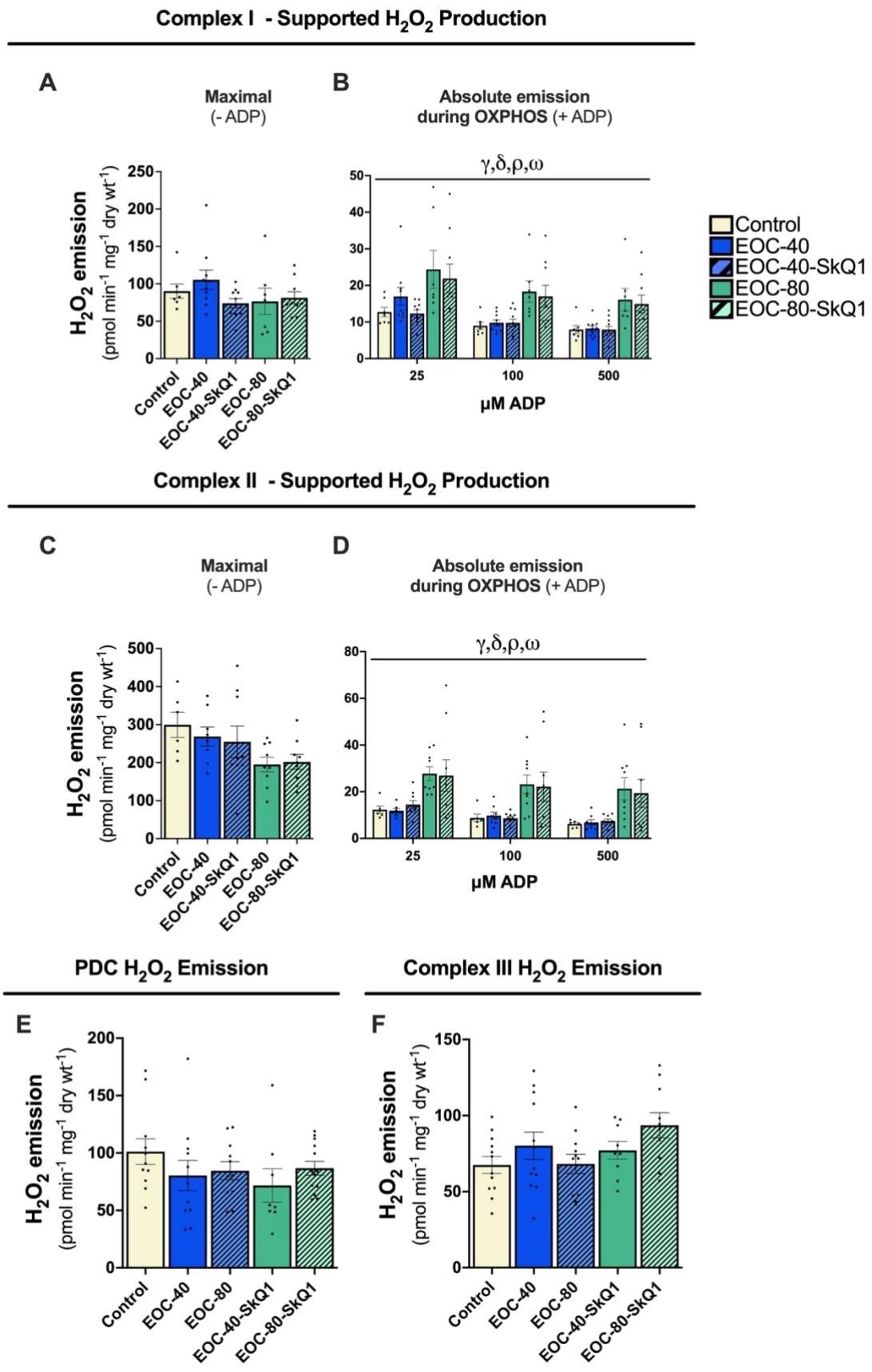
Complex I - Supported H_2O_2 Production
A
Maximal
(- ADP)
H_2O_2 emission
(pmol min^{-1} mg^{-1} dry wt^{-1})
Control
EOC-40
EOC-40-SkQ1
EOC-80
EOC-80-SkQ1
B
Absolute emission
during OXPHOS (+ ADP)
γ,δ,ρ,ω
25
100
500
μM ADP
Complex II - Supported H_2O_2 Production
C
Maximal
(- ADP)
D
Absolute emission
during OXPHOS (+ ADP)
PDC H_2O_2 Emission
E
Complex III H_2O_2 Emission
F

Supplemental Figure 3. Site-specific mH_2O_2 emission in the white gastrocnemius of EOC-tumour bearing mice subjected to either SkQ1 or normal drinking water. A) Complex I-supported (pyruvate and malate) maximal H_2O_2 emission. **B)** Complex I supported and ADP-stimulated absolute H_2O_2 emission, n= 7-11. **C)** Complex II-supported (succinate) maximal H_2O_2 emission. **D)** Complex II supported and ADP-stimulated absolute H_2O_2 emission, n= 7-11. **E)** Pyruvate dehydrogenase complex-derived (pyruvate and rotenone) maximal H_2O_2 emission, n= 8-13. **F)** Complex III derived (Antimycin A) maximal mH_2O_2 emission. n = 10-12. **H_2O_2**: Hydrogen Peroxide. Analyses for **A**, **C**, **E** and **F** were conducted using either a standard one-way ANOVA or Kruskal-Wallis test, depending on whether data was normally distributed. Analyses for **B** and **D** were conducted using a standard two-way ANOVA. Analyses were followed by a two-step step-up method of Benjamini, Krieger, and Yukutieli for post-hoc analysis. Results represent mean ± SEM. γ = $p < 0.05$ Control vs EOC-80, δ = < 0.05 Control vs EOC-80-SkQ1, ρ = $p < 0.05$ EOC-40 vs EOC-80, ω = EOC-40-SkQ1 vs EOC-80-SkQ1.

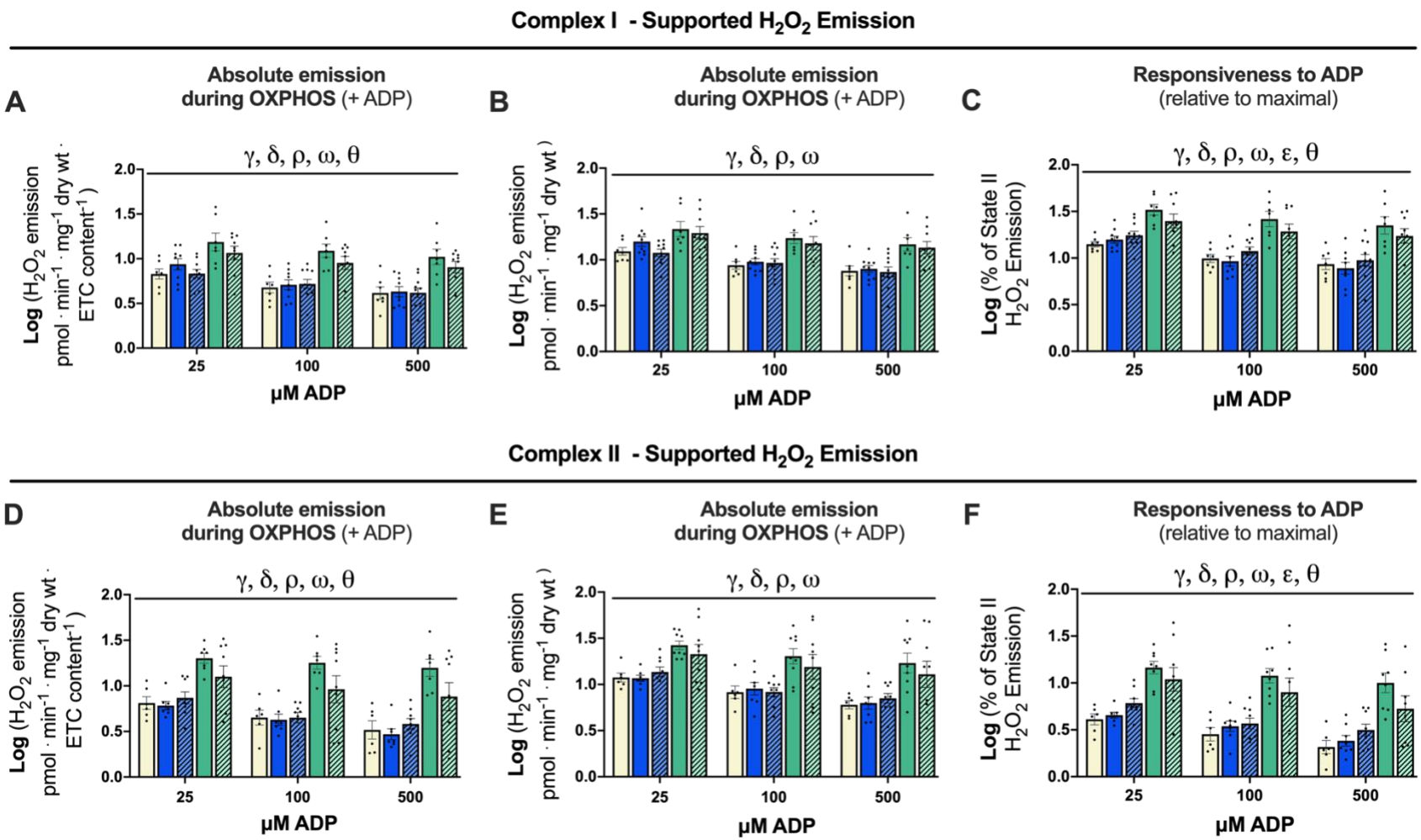
Complex I - Supported H_2O_2 Emission
A
Absolute emission during OXPHOS (+ ADP)
γ, δ, ρ, ω, θ
Log (H_2O_2 emission pmol · min^{-1} · mg^{-1} dry wt · ETC content^{-1})
μM ADP
B
Absolute emission during OXPHOS (+ ADP)
γ, δ, ρ, ω
Log (H_2O_2 emission pmol · min^{-1} · mg^{-1} dry wt)
μM ADP
C
Responsiveness to ADP (relative to maximal)
γ, δ, ρ, ω, ε, θ
Log (% of State II H_2O_2 Emission)
μM ADP
Complex II - Supported H_2O_2 Emission
D
Absolute emission during OXPHOS (+ ADP)
γ, δ, ρ, ω, θ
Log (H_2O_2 emission pmol · min^{-1} · mg^{-1} dry wt · ETC content^{-1})
μM ADP
E
Absolute emission during OXPHOS (+ ADP)
γ, δ, ρ, ω
Log (H_2O_2 emission pmol · min^{-1} · mg^{-1} dry wt)
μM ADP
F
Responsiveness to ADP (relative to maximal)
γ, δ, ρ, ω, ε, θ
Log (% of State II H_2O_2 Emission)
μM ADP

Supplemental Figure 4. Log transformed H_2O_2 emission data. **A)** Complex-I supported and ADP stimulated absolute mH_2O_2 emission normalized to ETC content. **B)** Complex-I supported and ADP stimulated absolute mH_2O_2 emission. **C)** Responsiveness of ETC to ADP (maximal / absolute *100). **D)** Complex-II supported and ADP stimulated absolute mH_2O_2 emission normalized to ETC content. **E)** Complex-II supported and ADP stimulated absolute mH_2O_2 emission. **F)** Responsiveness of ETC to ADP (maximal / absolute *100). All data were non-normally distributed and were first log-transformed, then analyzed using a standard two-way ANOVA. Analyses were followed by a two-step step-up method of Benjamini, Krieger, and Yukutieli for post-hoc analysis. Results represent mean $\pm$ SEM. α = $p < 0.05$ Control vs EOC-40, β = $p < 0.05$ Control vs EOC-40-SkQ1, γ = $p < 0.05$ Control vs EOC-80, δ = < 0.05 Control vs EOC-80-SkQ1, ε = $p < 0.05$ EOC-40 vs EOC-40-SkQ1, θ = $p < 0.05$ EOC-80 vs EOC-80-SkQ1, ρ = $p < 0.05$ EOC-40 vs EOC-80, ω = EOC-40-SkQ1 vs EOC-80-SkQ1.

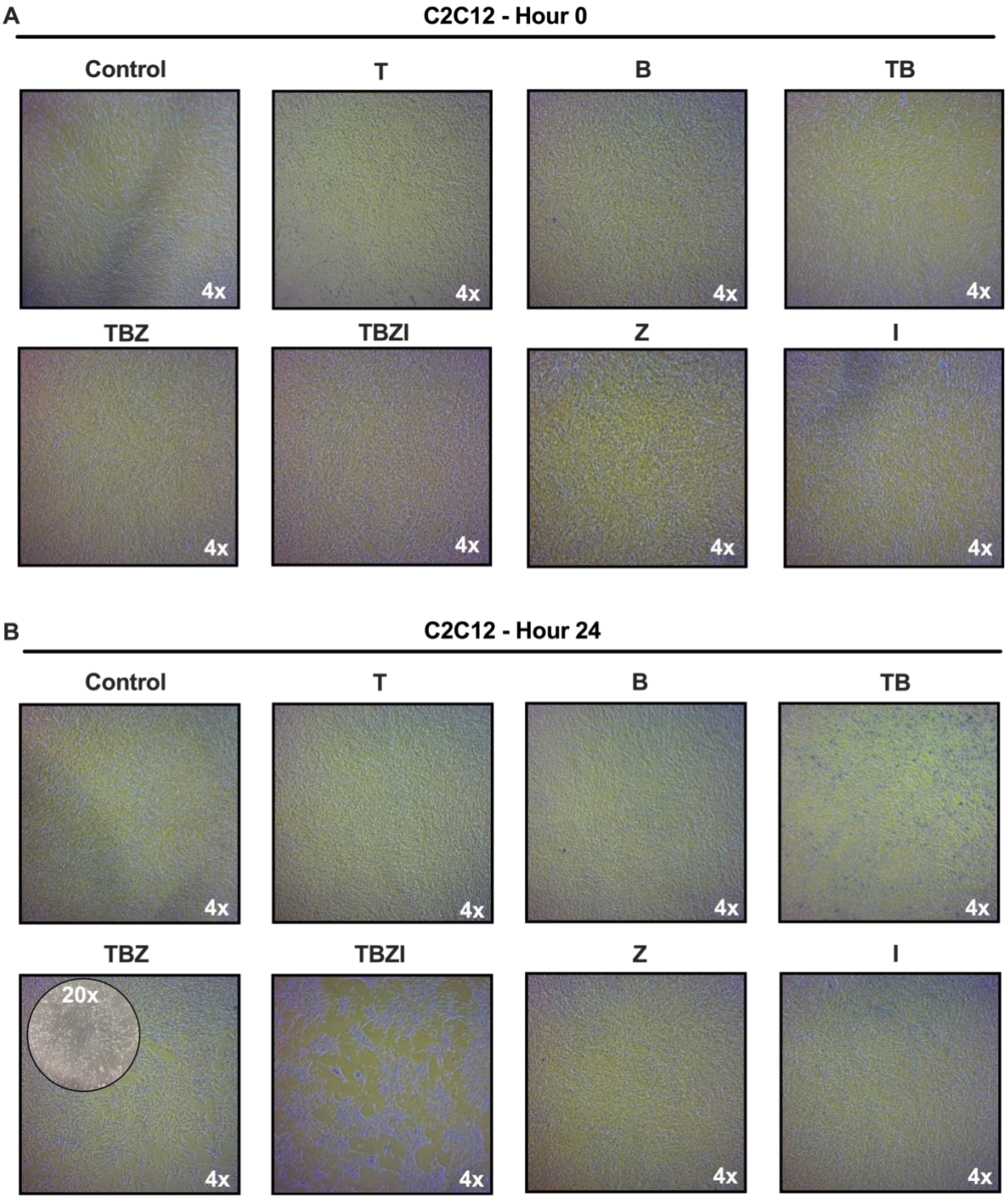

Supplemental Figure 5. C2C12 myoblasts pre (hour 0) and post (hour 24) combination of TNF-α (T), B (BV6), z-VAD-FMK (Z) and z-IEDT-FMK (I) treatment. **A)** Images of C2C12 plates captured at 4x magnification prior to TBZI treatment. **B)** Images of C2C12 plates captured at 4x magnification 24 hours post TBZI treatment. BSA (T vehicle) and DMSO (BZI Vehicle) plates not shown.

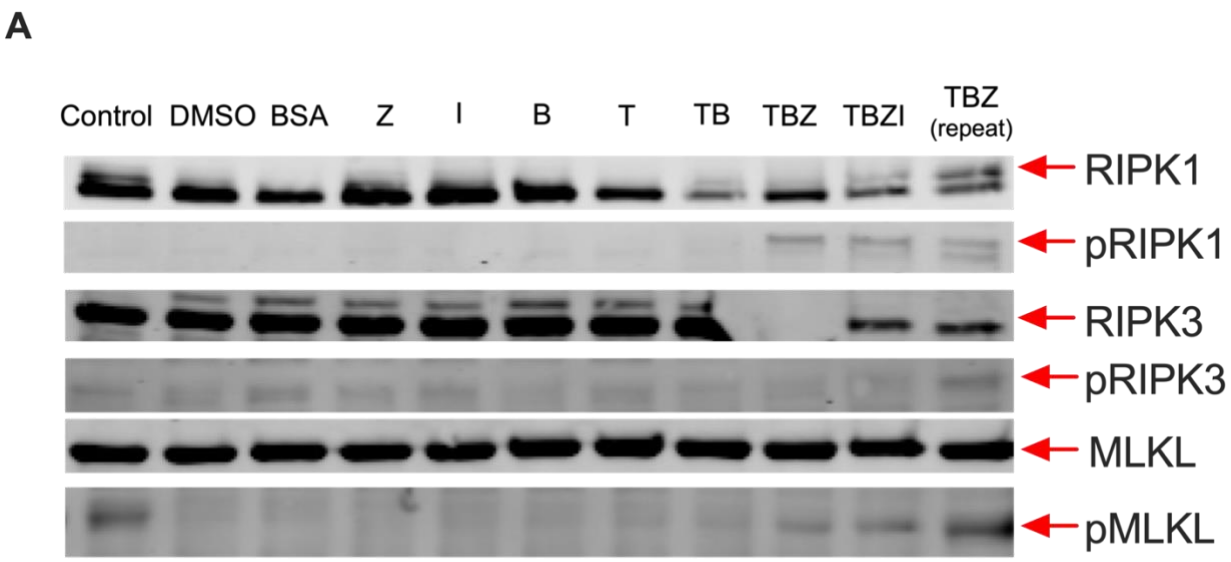

Supplemental Figure 6. **Western blots of C2C12s treated with different combinations of TBZI. RIPK1**: Receptor Interacting Serine/Threonine Protein Kinase 1, **RIPK3**: Receptor Interacting Serine/Threonine Protein Kinase 3, **MLKL**: Mixed-Lineage Kinase Domain-Like Protein, **pRIPK1**: phosphorylated RIPK1, **pRIPK3**: phosphorylated RIPK3, **pMLKL**: phosphorylated MLKL.

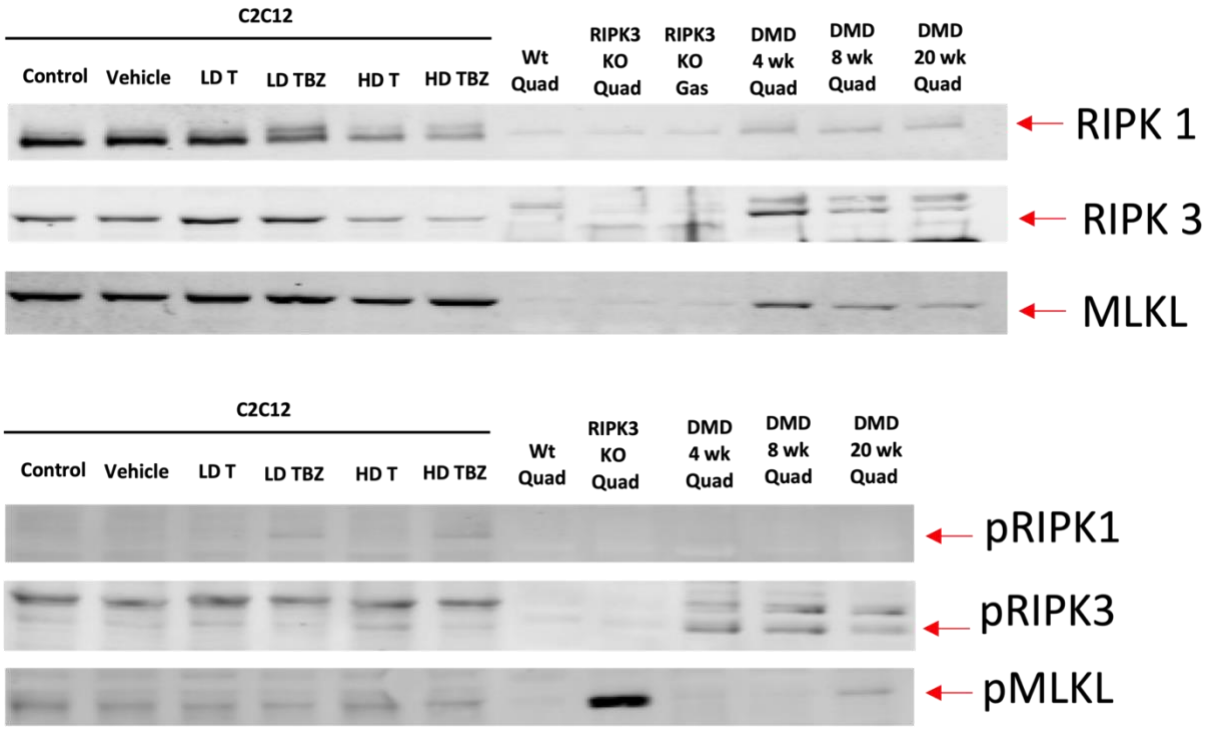

Supplemental Figure 7. Western blots of C2C12s treated with different combinations of TBZI, wild-type quadriceps, RIPK3 KO quadriceps and gastrocnemius, and quadriceps from D2.mdx mice at different ages. Vehicle: BSA (TNF-α vehicle) and DMSO (BV6 and z-Vad-FMK vehicle). **LD T:** low dose TNF-α. **LD TBZ**: low dose TNF-α, BV6 and z-Vad-FMK. **HD T:** high dose TNF-α. **HD TBZ**: high dose TNF-a, BV6 and z-Vad-FMK. **Wt**: wild-type. **RIPK3 KO**: RIPK3 knockout. **DMD**: Duchenne muscular dystrophy. **Quad**: quadriceps. **Gas**: gastrocnemius. **RIPK1**: Receptor Interacting Serine/Threonine Protein Kinase 1, **RIPK3**: Receptor Interacting Serine/Threonine Protein Kinase 3, **MLKL**: Mixed-Lineage Kinase Domain-Like Protein, **pRIPK1**: phosphorylated RIPK1, **pRIPK3**: phosphorylated RIPK3, **pMLKL**: phosphorylated MLKL.

APPENDIX A – DETAILED METHODS

A.1 TISSUE HOMOGENIZATION AND WESTERN BLOT

BUFFERS

Homogenization Buffer:

Amount	Reagent	Concentration	Molecular Weight
630.4mg	TRIS/HCL	20mM	157.60
1.752g	NaCl	150mM	58.44
74.48mg	EDTA	1mM	372.24
76.07mg	EGTA	1mM	380.35
223mg	$Na_4O_7P_2$	2.5mM	446.06
36.78mg	Na_3VO_4	1mM	183.91
2mL	Triton X-100	1%	

Homogenization Buffer for Westerns (From Steinberg):
https://www.ncbi.nlm.nih.gov/pmc/articles/PMC5579332/
For 200mL solution at pH 7.0 (on website for PhosSTOP - https://www.sigmaaldrich.com/catalog/product/roche/phossro?lang=en&region=CA&gclid=Cj0KCQiA2uH-BRCCARIsAEeef3l9MIvgRrOy6x8a6xoGZ8fNCJNFITUEZWEieSDZn6UT7iNxiES3PbwaAoUxEALw_wcB)

---

10 X Running Buffer:
Eg. for 1 L running buffer. Add the following ingredients then add ddH2O until you reach 1 L. Let it stir with stir bar.

	500 ml	1 L	2 L
Tris Base	15 g	30 g	60 g
Glycine	72 g	144 g	288 g
SDS	5 g	10 g	20 g

1 X Running Buffer: 10 X Running buffer 100 ml
dH_2O 900 ml

Trans-Blot Turbo 1x Transfer Buffer (Bio-Rad) 1L:

	1 L
5x Transfer Buffer	200mL
ddH_2O	600mL
Ethanol	200mL

---

10 X TBS (Tris Buffered Saline):

	500 ml	**1 L**
Tris Base	12.1 g	24.2 g
NaCl	40 g	80 g
Adjust to pH 7.6 with HCl		

1 X TBST:

	1 L	**2 L**
10 X TBS	100 ml	200 ml
ddH_2O	900 ml	1800 ml
Tween 20	1ml	2 ml

Note: Ensure solution is stirring when adding Tween

1.5M Tris-Base pH 8.8

	1 L
Tris-Base	g
ddH_2O	1000mL

Add KOH pellets or HCl to adjust pH as needed

1M Tris-Base pH 6.8

	1 L
Tris-Base	g
ddH_2O	1000 mL

Add KOH pellets or HCl to adjust pH as needed

Gel Composition

	Stacking	**Running**				
		5%	**6%**	**8%**	**10%**	**12%**
dH_2O	6.8 ml	11.4	10.6 ml	9.4 ml	8 ml	6.7 ml
1.5M Tris-Base, pH 8.8	***	5 ml	5 ml	5 ml	5 ml	5 ml
1M Tris-Base, pH 6.8	1.25 ml	***	***	***	***	***
30 % Acrylamide (in fridge)	1.70 ml	3.4 ml	4 ml	5.3 ml	6.7 ml	8 ml
10 % SDS	100 µl	200 µl	200 µl	200 µl	200 µl	200 µl
10 % APS	100 µl	200 µl	200 µl	200 µl	200 µl	200 µl
Temed	**20 µl**	**20 µl**	**20 µl**	**20 µl**	**20 µl**	**20 µl**

10% SDS

	1 mL
SDS	100 mg
ddH_2O	1000 uL

10% APS (need to make fresh every experiment)

	1 mL
APS (Ammonium Persulfate)	100 mg
ddH_2O	1000 uL

Amido Black De-stain

	1 L
Isopropanol	250 mL
ddH_2O	650 mL
Acetic Acid	100 mL

Amido Black 1x

	50 mL
Amido Black Staining Solution (2x)	25 mL
ddH_2O	25 mL

Blocking Buffer

- 20mL LiCOR Blocking solution

Primary

- Blocking Buffer (typically 7mL)
- Primary antibody (typically 1:1000 – 7uL)
- .1% Tween (typically 7uL)
- .01% SDS (typically 7uL)

Secondary

- LICOR Blocking Buffer (typically 20mL)
- Secondary antibody (typically 1:20,000 – 1 uL)
- .1% Tween (typically 20 uL)
- .01% SDS (typically 20 uL)

The secondary is light sensitive so wrap a 50 ml falcon tube with aluminum foil first.

PROTOCOL

Muscle Homogenization

1. Place muscle in metal dish filled with liquid nitrogen
2. Using pre chilled spatula chip piece of muscle of desired size
3. Using pre chilled forceps quickly place muscle on scale to get rough weight (do not wait for steady weight). While weighing, place forceps back in liquid nitrogen to remain cool
4. After getting weight, place muscle back in liquid nitrogen storage dewer until all samples have been weighed
5. Place muscle in desired volume of homogenization buffer that contains 10ug muscle:100ul Buffer. Make sure the buffer includes:
    a. 1 tablet/10mL PhosSTOP
    b. 1:200 Protease Inhibitors

NOTE: [this works best when you make a stock of homogenization buffer with PhosSTOP and protease inhibitor already diluted]

6. Fill 50mL beaker with ice and place Eppendorf with muscle securely in ice
7. Homogenize using tapered pestle for 3x10 seconds
8. Centrifuge at 800g for 10 minutes at 4°C
9. Save supernatant at -80°C

Protein Assay – BCA

1. Create standards by diluting BSA in homogenization buffer Standards (BSA):
   0 mg/mL (buffer)
   0.0625 mg/mL
   0.125 mg/mL
   0.25 mg/mL
   0.50 mg/mL
   1.00 mg/mL
2. Dilute 5 µL of each sample in 45 µL of homogenization buffer
3. Using a 96 well plate load in triplicates each standard and each sample
4. Add 190uL of mixed solution (50:1 Solution A:SolutionB) into each well of sample
   * Amount needed: (# of standards + # of unknowns) x (3 replicates) x (200uL)
5. Heat in oven for 30 minutes at 37°C

Western Blot

1. In 50mL falcon tubes make running gel and stacking gel (1 column makes 2 gels) **DO NOT ADD TEMED UNTIL READY TO LOAD**
2. Take 1 short plate and one spacer plate and clean both sides of glass with methanol and kimwipe
3. Place clean short plate on top of spacer place and place both in mounting apparatus, ensuring the edge of the plates are lined up against the bench top
4. Place plates in apparatus on foam piece in gel stand
5. Place 3 transfer pipettes and falcon tube with methanol close to gel stand
6. Add TEMED to running gel and invert falcon tube 1-2 times
7. Using transfer pipette, fill space between glass plates with running gel until solution reaches the top of the green doors
1. Using new transfer pipette add methanol to top of plate to create an even line along the top of the gel removing any bubbles
2. Let sit until remaining running gel has hardened in the falcon tube
3. Once gel has set, invert gel to remove any excess methanol
4. Add TEMED to stacking gel and invert 1-2 times
5. Using transfer pipette, add stacking gel to top of glass plates, use methanol transfer pipette to remove any bubbles
6. Add comb to top of gel and allow to set
7. Prepare diluted samples by combining sample, water and Laemmeli's buffer + 2-mercaptoehtanol (100 µl 2-mer: 900 µl Lam)
   a. **Example of dilution to load 50µg protein at a concentration of 1µg/ µl**

Sample	Corr Prot (ug/ul)	Aliquot (ug)	Sample (ul)	H20	4X Laem (1:9 2-Mercap)	Vol for 1 Well
C7.5-A	**4.599**	50	**10.9**	26.6	12.5	50

8. Boil samples at 95 °C for 5 minutes
    - DO NOT BOIL OXPHOS SAMPLES
9. Spin down samples for 5 seconds
10. Make 1X running buffer in 1000mL graduated cylinder
11. Remove combs from gels and place gels in gasket.
12. Place gasket with gels in tank and add 1X running buffer until it fills the top of gasket and tank.
13. Load wells with desired concentration of samples.
14. Run for desired time (40-75 minutes) at 160mV (or desired voltage)
15. Fill 2 plastic "biorad" dishes, one with methanol and one with transfer buffer
16. Place 2 transfer packs in dish of transfer buffer and place membrane in dish of methanol
17. After 2-3 minutes place first transfer pack on bottom of transfer case
18. Place membrane in transfer buffer for 10-15 seconds
19. Place membrane on top of transfer pack ensuring no air bubbles
20. Remove short plate from gel and place gel face down on membrane
21. Place second transfer pack on top of membrane
22. Using roller, roll from one side of transfer pack to the other to remove air bubbles
23. Hold firmly down in the middle of the transfer pack and remove excess liquid
24. Put lid on transfer case and run transfer (standard setting is 1.5mm gel for 10 minutes)
25. Following transfer remove membrane and place in dish with blocking buffer (50% Odyssey Blocking Buffer, 50% TBS) for 1 hour, rocking at room temperature
26. After 1 hour pour blocking buffer back into falcon tube (it can be resused) and add primary antibody
27. Place membrane in primary in fridge overnight, rocking
28. In the morning remove primary and pour back into falcon tube (can be resued)
29. Add TBST to dish and complete 3x5 minute TBST washes rocking at room temperature.
30. Add secondary antibody and leave rocking at room temperature for 1 hour
31. Remove secondary and place back in falcon tube (can be resused)
32. Complete 3 more 3x5 minute TBST washes
33. Detect using LiCOR Infrared Imager
34. Once imaging is complete, place membrane in biorad dish and shake for 3 minutes with Amido Black
35. Put amido black back in aluminum foil falcon tube and fill biorad dish with amido black destain and shake for 30 minutes.
36. Once membrane is dried, scan membrane for total protein.

TROUBLESHOOTING TIPS

White non-specific bands (LD)

- Ensure your blocking is fresh and NOT diluted
- Your secondary antibody concentration may be too high – try diluting. 1:40 000 is the highest you should probably go
- Do **NOT** include SDS in your primary

Blot not running straight (LD)

- Likely a leak in the electrode cassette. To avoid this be very diligent in refilling the electrode while the gel is running (every 5 minutes for the first 20 minutes). This issue never happens with 4 gels but tends to happen with 2.
- Make sure the wire is clean. There may be build-up of salts

A.2 ROS PROTOCOL

BUFFERS

BIOPS BUFFER (Extracellular)

Chemical	Stock Solution	Molecular Weight	Final Concentration	Addition to *2 Litre* Final Volume
CaK_2EGTA*	100mM		2.77mM	55.4mL
K_2EGTA*	100mM		7.23mM	144.6mL
Na_2ATP		551.1	5.77mM	6.41g
$MgCl_2 \cdot 6H_2O$		203.3	6.56mM	2.67g
Taurine		125.1	20mM	5.02g
Na_2Phosphocreatine		327.14	15mM	9.81g
Imidazole		68.1	20mM	2.72g
Dithiothreitol (DTT)		154.2	0.5mM	0.154g
MES Hydrate		195.2	50mM	19.52g

*__ALWAYS__ double check molecular weights for supplier-specific chemicals (n=m/M.W.)

BIOPS contains the following ion concentrations		**EXTRACELLULAR RANGE**
Ca^{2+} free	0.1uM	Rat: 7.6mM Mouse: 1.3mM
Mg^{2+} free	1mM	
Na^+	41mM	Human: 133-143mM
K^+	20mM	Human: 4.5mM
Cl^-	13mM	Rat: 160mM Mouse: 95-120mM
MgATP	5mM	
Ionic Strength	160mM	
Osmolality	295 mOsm	

*Ionic strength is the sum of all ions
*Buffers do not perfectly reflect extracellular conditions
*Species-specific extracellular ranges exist
*Ranges are expressed as mmol/L (refer to ion concentration summary chart)

CaK_2EGTA: Dissolve 2.002g of $CaCO_3$ in 100mM hot (80°C) solution of EGTA (7.608g of EGTA in 200mL ddH_2O). Add 2.3g of KOH and adjust pH to 7.0 using KOH. Freeze unused portions.

K_2EGTA: Dissolve 7.608g EGTA and 2.3g KOH into 200mL ddH_2O. Adjust pH to 7.0 using KOH. Freeze unused portions.

To make BIOPS:

1. Add approximately 1500mL of ddH_2O to 2000mL beaker

2. While constantly stirring add stock solutions of CaK_2EGTA and K_2EGTA
3. Weigh and add all powder chemicals
4. Adjust pH to 7.2 using KOH pellets
5. Using graduated cylinder, bring total volume to 2000mL
6. Filter and then aliquot into 50mL falcon tubes
7. Freeze falcon tubes

BUFFER Z (Intracellular)

Chemical	Molecular Weight	Final Concentration	Addition to *500mL* Final Volume
K-MES	233.33	105mM	12.26g
KCl	74.55	30mM	1.12g
KH_2PO_4	136.08	10mM	0.7g
$MgCl_2 \cdot 6H_2O$	203.3	5mM	0.51g
EGTA	380.35	1mM	0.19g
BSA		5mg/mL	2.5g

*__**ALWAYS**__ double check molecular weights for supplier-specific chemicals (n=m/M.W.)

Buffer Z contains the following ion concentrations		**INTRACELLULAR RANGE**
Ca^{2+}	0.0uM	Human: 30nM – 60nM SR: 5.7-20mmol/L Free Ca^{2+} in SR 0.2-0.5mM Rat: 7.76-11.11 ueq/g dry wt
Mg^{2+} (total, not free)	5mM	
Na^+	0.0mM	Human: 6-13mM Rat: 7.10-21.9mmol/L
K^+	145mM	Human: 130 – 164mmol/L Rat: 117 – 149mmol/L
Cl^-	40mM	Rat: 4.97-16.57mmol/L
PO_4^{3-}	10mM	
EGTA free	1mM	

*Buffers do not perfectly reflect extracellular conditions
*Species-specific intracellular ranges exist
*Ranges are expressed as mmol/L (refer to ion concentration summary chart)

To make Buffer Z:

1. Add approximately 400mL of ddH_2O to 1000mL beaker
2. Weigh and add all powder chemicals
3. Adjust pH to 7.2 using KOH pellets
4. Using graduated cylinder, bring total volume to 500mL

5. Filter and then aliquot into 50mL falcon tubes
6. Freeze falcon tubes

AMPLEX ULTRA RED
Total volume per experiment: 1000ul in Hellma 109.004F fluorescent cell
Total volume per black tube: 1030ul (recommend 1050 next time)

Stock A and B ingredients required:
5mM Amplex Ultra-Red (Invitrogen A36006)
5000 IU/ml Cu/Zn Superoxide dismutase (SOD1; Sigma S9697)
10mM Blebbistatin (BLEB; Cayman)
0.5M EGTA (aliquots in freezer)

Stock B additional ingredients:
20mM Creatine anhydrous

Final concentrations for both AUR Stock A and AUR Stock B:
10uM AUR
5uM BLEB
25U/ml Cu/Zn SOD1
1mM EGTA

Work fairly quickly given AUR and BLEB should not be stored on ice. Best to prepare with lights out in lab as AUR and BLEB are light sensitive.

Preparation of AUR stock B (20mm creatine):

Prepare 10uM AUR stock as in Stock A but with 20mM creatine anhydrous. Mix the following:
- 160.6 ml of Buffer Z.
- 421.19 mg creatine anhydrous
- 325ul of 5mM AUR
- 812.5ul of 5000 IU/ml SOD1
- 80.3ul of 10mM BLEB
- 325ul of 0.5M EGTA

Aliquot 1.025 ul in black tubes. Store @ -80°C.

BUFFER NOTES

BIOPS BUFFER
- BIOPS is designed to mimic the extracellular environment
- BIOPS should be a relaxing media to prevent basal sodium/potassium flux that stimulates electrical signals in muscle - this is the purpose of having high K^+ (K^+ counteracts action potentials)
- BIOPS prevents cell shrinkage or swelling

➔ Keep Ca^{2+} low and ATP available
➔ Keep it cold

- Saponin removes cell membrane ~ 15mins into permeabilization

CaK2EGTA

- Need some Ca^{2+}, but too much kills cell (calpain and caspase activation, mitochondrial swelling)
- If you do not have enough Ca^{2+}, you cannot prime all dehydrogenases and ETC (keep them active)
- PDH requires Ca^{2+} as an example to be activated ← Ca^{2+} binds PDP (pyruvate dehydrogenase phosphatase), not PDH itself
- SR may have lost their normal regulation, so we need EGTA to maintain low Ca^{2+}
- K^+ relaxes the fibres so they stay flaccid while you are separating (prevent spontaneous depolarization)
- EGTA is a cationic non-specific chelater – it can chelate Ca^{2+} and Mg^{2+}; binds divalent cations (that is why it cannot chelate Na^+ or K^+); EGTA has a higher affinity for chelating Ca^{2+} (prevents Ca^{2+} from going too high)
- EGTA buffers Ca^{2+} and keeps Free Ca^{2+} super low
- Mito can swell over time if you do not have EGTA to buffer Ca^{2+}
- Amount of Ca^{2+} and amount of EGTA determines Free Ca^{2+} (refer to sample calculation e.g. *McGuigan et al. Can. J. Physiol. Pharmacol.* 69:1733 – 1749, 1991)

Na2ATP

- Na^+ is exchanged with Mg^{2+} from $MgCl_2$ (ATP naturally binds to Mg^{2+} creating Mg•ATP in the buffer)
- ATP relaxes fiber in buffer – therefore, it relaxes myosin with ATP
- ATP supports metabolism while separating fibers in BIOPS
- BIOPS contains 41mM of Na^{2+}, which is less than the known extracellular ion concentration of 133-143mM – this may be to ensure that fibres are not excessively activated (remain somewhat relaxed) – see ion concentration chart in separate file

$MgCl_2$

- Mg^{2+} is needed for metabolism because it is required in the ETC for ATP production (cofactor for ATP synthase)
- Any enzyme that hydrolyzes or makes ATP needs Mg^{2+}
- EDTA preferentially chelates Mg^{2+} over Ca^{2+} (this is why EDTA is NOT added)

Taurine

- Sulphur-based, inert compound used to balance osmolarity; could be an antioxidant
- Cation chelater (keeps Ca^{2+} and Mg^{2+} in balance)

PCr

- Need it for energy production and phosphate shuttling mechanism between mitochondria and cytoplasm; keeps energy exchange higher
- PCr loss likely occurs during permeabilization, which requires addition to buffer

Imidazole ** might do many things

- Preservative and antioxidant that prevents bacterial growth in BIOPS and might inhibit contraction
- Potentially causes hyperpolarization of mitochondrial membrane

Dithiothreitol (DTT)

- Two thiols groups → very common antioxidant; if you do not have antioxidants, a lot of enzymes can form disulfide bonds and become inactivated by ROS
- Therefore, it must be at very low concentrations

2-(N-Morpholino) ethanesulfonic acid (MES) Hydrate

- Buffers protons and is a substitute for the natural in vivo bicarbonate buffer
- "S" refers to sulfonic acid, which buffer protons
- Acids exist in equilibrium as negative and positive. Therefore, sulfonic acids will buffer H+ as a natural part of their equilibrium

  MES effective pH range: 5.5-6.7

  HEPES pH range: 6.8-8.2 ← this may be more ideal

Cytoplasmic Ca^{2+} low, Mg^{2+} high

- This prevents Ca^{2+} induced mitochondrial swelling and ensures high Mg^{2+} for ATP synthase and ATPases throughout cell given Mg^{2+} is a cofactor for ATP
- Therefore, EGTA is used, not EDTA, to keep Ca^{2+} low and Mg^{2+} high (EGTA is a strong Ca^{2+} chelater and a weak Mg^{2+} chelater) – EDTA is the opposite
- Must prevent mitochondrial swelling (keep low Ca^{2+} so it does not die and need Mg^{2+} for metabolism while you are separating and permeabilizing fibres)
- Free Mg^{2+} is a calculation of what is left from $MgCl_2$ after being bound to ATP that was added to the buffer and chelated weakly by EGTA
- The same is true of Free Ca^{2+} and EGTA

Importance of total osmolarity

- Do not want to swell or shrink the cytoplasm and mitochondria while you are separating (osmolarity is anything that draws water)
- Calculated based on concentration of every component of the buffer – every component is water soluble (contributes to osmolarity), not just the salts
- Extracellular osmolarity is 295 mOsm, just like BIOPS buffer

Importance of total ionic strength

- Maintaining protein shapes throughout cell through ionic bonds
- Ionic strength is total ions in a cell

BUFFER Z

- Principles listed above for BIOPS are the same for Buffer Z, regarding $MgCl_2$, EGTA, BSA, KH_2PO_4 and MES
- Buffer Z is used for H_2O_2 emission because it does not contain any antioxidants or sucrose

BSA benefits:

1. Buffers protons;
2. Buffers FFA;
3. Buffers ROS (it is loaded with cysteines and histidines which can react with ROS to buffer it);
4. Contributes to osmolarity of cell

Special note: Potassium source

- BUFFER Z uses K-MES

Special note: Chloride (from KCl)

- Intracellular Cl^- is supraphysiological; this does not seem to affect respiration (see figure 1A of *Perry and Kane et al. Diabetes* 2013. Note Mitomed is similar to MiRO in figure)

- Cl^- above 30mM can cause mtCK to dissociate from inner membrane space according to Oroboros blue book. However, our lab still obtains good respiration and H_2O_2 with Cr compared to without

ROS STANDARD CURVE

1. H2O2 dilution (serial dilution)
   - H2O2 is light sensitive, keep in dark when possible.
   - 3% w/w H2O2 : 3 g H2O2 / 100 mL solution (1 mol H2O2 / 34.01 g) = 0.0882 mol H2O2 / .100 L = .882 mol H2O2 / 1 L = 0.882 M H2O2

     (1) 4310ul ddH2O + 100ul 3% w/w H2O2 >>>> 20mM H2O2

     (2) 3980ul ddH2O + 20ul 20mM H2O2 >>>>>> 100uM H2O2

     (3) 3200ul ddH2O + 800ul 100uM H2O2 >>>>> 20uM H2O2

     (4) 2000ul ddH2O + 2000ul 20uM H2O2 >>>>>> 10uM H2O2

     (5) 2000ul ddH2O + 2000ul 10uM H2O2 >>>>>> 5uM H2O2
2. Add your Amplex UltraRed, HRP, (oligomycin) and other substrates (G/M/S/G-3-P……) into the cuvatte as protocol
3. H2O2 titration ([final H2O2] depends on the final volume in the cuvate, which will vary depending on your protocol)

   Make sure to wipe out the outside of the pipet tip before adding into the cuvette.

If for 1000 ul Titrate very fast, 45-60 sec		If for 200ul Titrate very fast, 45-60 sec	
[H2O2] (µM)	Add (µl))	[H2O2] (µM)	Add (µl))
5	3.33	5	1.0
5	3.33	5	1.0
10	3.33	10	1.0
10	5	10	1.0
20	5	20	1.0
20	5	20	1.0
20	10	20	2.0

4. Repeat 3 times, Different experiment protocol run different standard curve

Generate Standard Curve: you will have 7 fluorescent intensity average points to generate Standard Curve. Check the highest fluorescent intensity (not including the spike) of most of the real experiment, pick up the first 4 to 7 points that the fluorescent intensity range just cover your highest flourescent intensity from experiment, sometimes, the 6^{th} and 7^{th} point should not be included in the Standard Curve if the intensity is too high. However, also have to test which of the 5-7 point standard curves give you a more reasonable data (especially, look at the very low ROS condition, if the result after applying the standard curve looks reasonable)

Permeabilized Fibre Preparation

Pre-surgery

1. For every fibre bundle you are going to make you will need one 0.5mL tube for wet weights one 1.5mL eppendorf tube for permeabilization and one 1.5mL tube for wash

* Keep all tubes and buffers on ice

2. In a 5mL tube, make 10mg/mL Saponin solution by dissolving a small amount of saponin in distilled water
    a. Vortex gently and place on rocker until ready for use
3. Fill all **permeabilization** tubes with 1.5mL of freshly thawed BIOPS, 40ug/mL saponin (6uL in 1.5mL BIOPS), and 6 uL CDNB for the appropriate tubes
4. Fill all **wash** tubes with 1.5mL freshly thawed BUFFER Y

Post-Surgery

1. Separate fibres in BIOPS as quickly and carefully as possible
    a. Remember to change ice block/ice pack frequently as buffer should never be allowed to warm up

Permeabilization

1. Add bundles to permeabilization tubes (the ones that have saponin) using forceps or a gel loading pipette tip
2. Place on nutator in the fridge for 30 minutes
    a. Make sure all Eppendorfs have the liquid mixing by ensuring that the air bubble is moving
    b. If air bubble appears stuck, invert Eppendorf 1-2 times to allow for movement and place back on nutator
3. After 30 minutes, transfer bundles to corresponding wash tubes using gel loading pipette tip
4. Place bundles in wash back on nutator in the fridge for 15 minutes
    a. Permeabilized bundles can remain in fridge in wash for up to 2 hours but will start to lose viability after that point so use bundles ASAP
5. After 15 minute wash proceed to “ROS protocol”

ROS PROTOCOL

SUCCINATE (Complex I reverse)

SLOT	Assay Buffer	Pre-experiment		Substrates		ADP		ADP		ADP	
1	20mM Creatine 1mL	**1U HRP** 2uL of 500U/mL Fibre	3 min	**10mM Succinate** 5uL of 2M	5 min	**25uM** 5uL of 5mM	2min	**100uM** 1.5uL of 50mM	2min	**500uM** 0.8uL of 500mM	2min
2	No Creatine 1mL										

PYRUVATE + MALATE (Complex I forward)

35uM CDNB (5uL of 10.5mM Stock)

SLOT	Assay Buffer	Pre-experiment		Substrates		ADP		ADP		ADP	
1	20mM Creatine 1mL	**1U HRP** 2uL of 500U/mL Fibre	3 min	**10mM Pyruvate** 5uL of 2M **2mM Malate** 2uL of 1M	1 min	**25uM** 5uL of 5mM	2min	**100uM** 1.5uL of 50mM	2min	**500uM** 0.8uL of 500mM	2min
2	No Creatine 1mL										

PYRUVATE + ROTENONE * OWN CUVETTE (For PDH complex)**

35uM CDNB (5uL of 10.5mM Stock)

SLOT	Assay Buffer	Pre-experiment		Substrates	
1	No Cr 1mL	**1U HRP** 2uL of 500U/mL **0.5uM Rotenone** 2uL of 250uM Fibre	**10MIN (In QM40)**	**10mM Pyruvate** 5uL of 2M	5 min
2	No Cr 1mL				

Antimycin A (for Complex III)

SLOT	Assay Buffer	Pre-experiment		Substrates	
1	No Cr 1mL	**1U HRP** 2uL of 500U/mL Fibre	3 min	**2.5uM** Antimycin 5uL of 0.5mM	**8 MIN**
2	No Cr 1mL				

** treat like succinate

H2O2 ANALYSIS

Phase 1: Export Traces

1. Go to the lab computer where H_2O_2 experiments were completed and open felix software
2. Open H_2O_2 file, right click protocol and click "export trace." Save all files in a folder and use a USB to transfer data over to a personal computer and back up data on One Drive (or any other location where you keep your data)
3. Once data is on personal computer where you wish to analyze, right click file you wish to analyze and click "export with excel.
4. Highlight first 4 rows and click delete.
5. All that should be remaining in the file is data in column A and column B. Column A will contain time data (independent variable) while column B will contain fluorescence intensity data (dependent variable), in other words the index of H_2O_2 emission. Copy all column A and column B data and paste it into the H_2O_2 analysis template

Phase 2: Setting up and understanding template sheet

1. Open H_2O_2 analysis template provided by a lab member and ensure the following criteria are met:

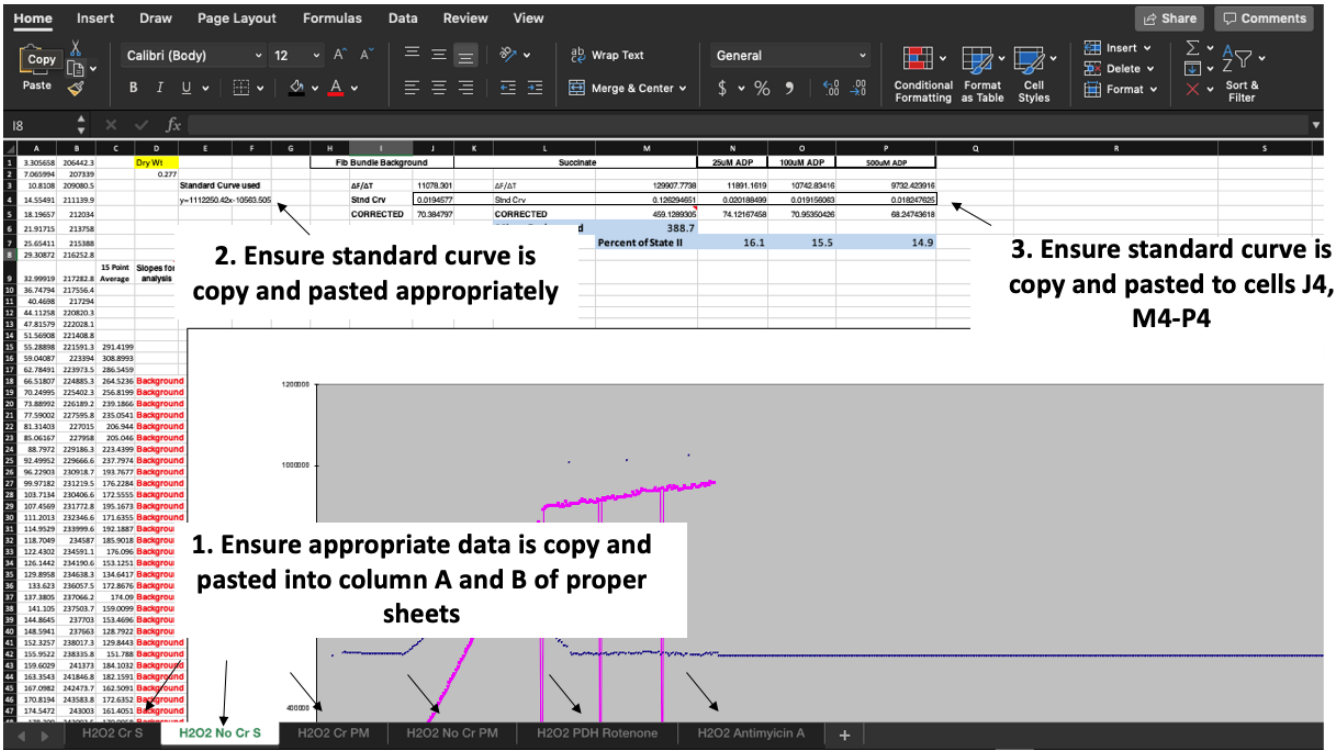

2. Once values are pasted into columns A and B the template will automatically create a 15 point or 10 point slope calculation in column C and generate a graph. See below for interpretation of data.

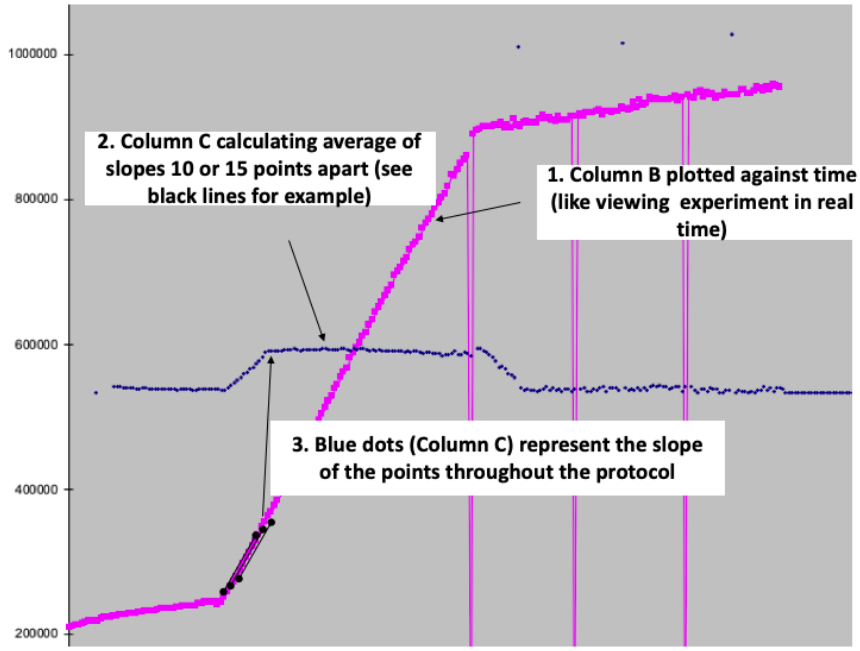

Phase 3: Analyze H_2O_2 Traces

Every protocol has slightly different patterns of H_2O_2 emission and therefore slightly different regions to be analyzed. Although different regions will be selected per protocol, the fundamental premise remains – **take large averages of max substrate emissions.** Some protocols can be a "judgment call" but this SOP will attempt to walk the reader through the best choices.

Succinate

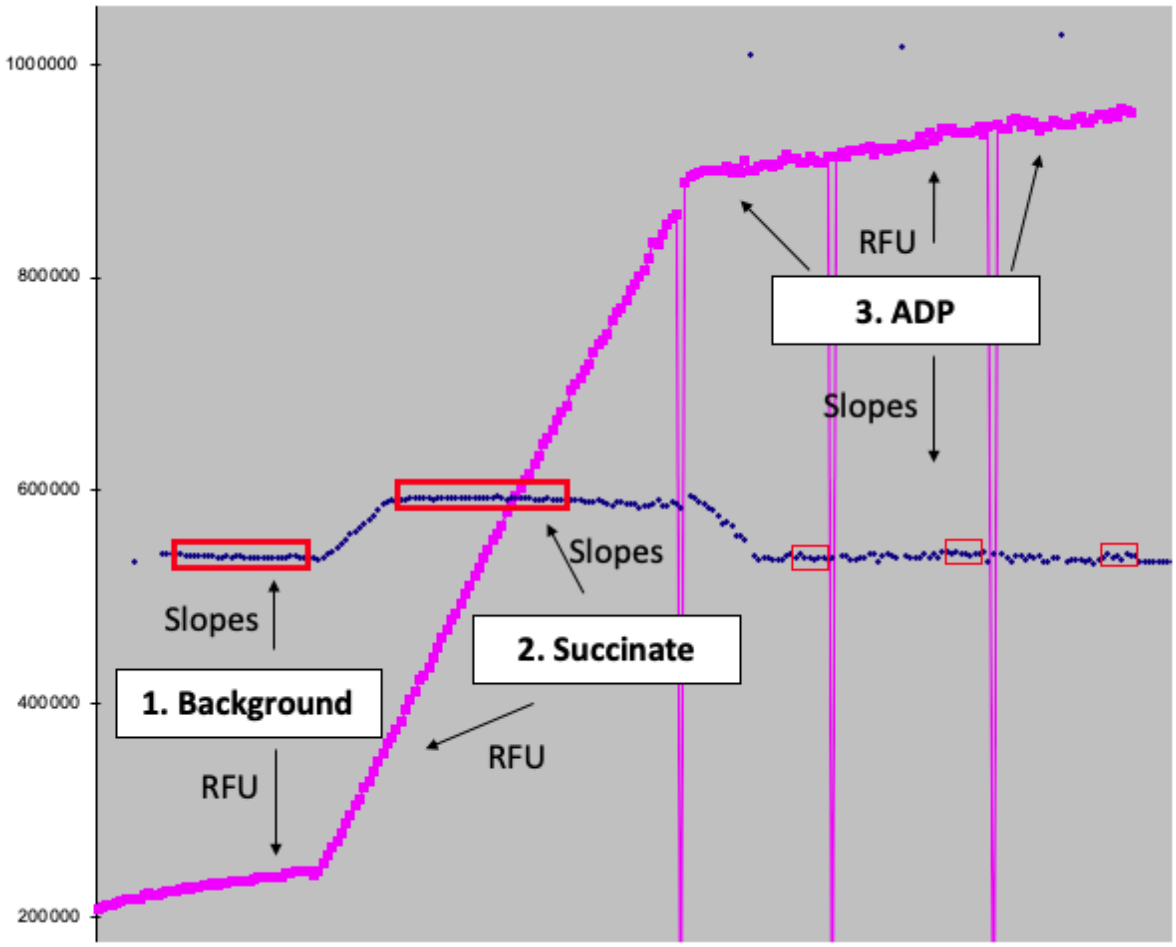

1. Background should be 2-3 minutes, succinate 5 minutes, ADP 2 minutes each
2. Make sure you are referencing column C to ensure you are measuring correct slopes calculated from RFU data (column B). **Be extra careful you are NOT averaging slopes of recording data from a previous titration.**
3. Data copied are in cells J5-P5 (corrected rates).

Pyruvate Malate

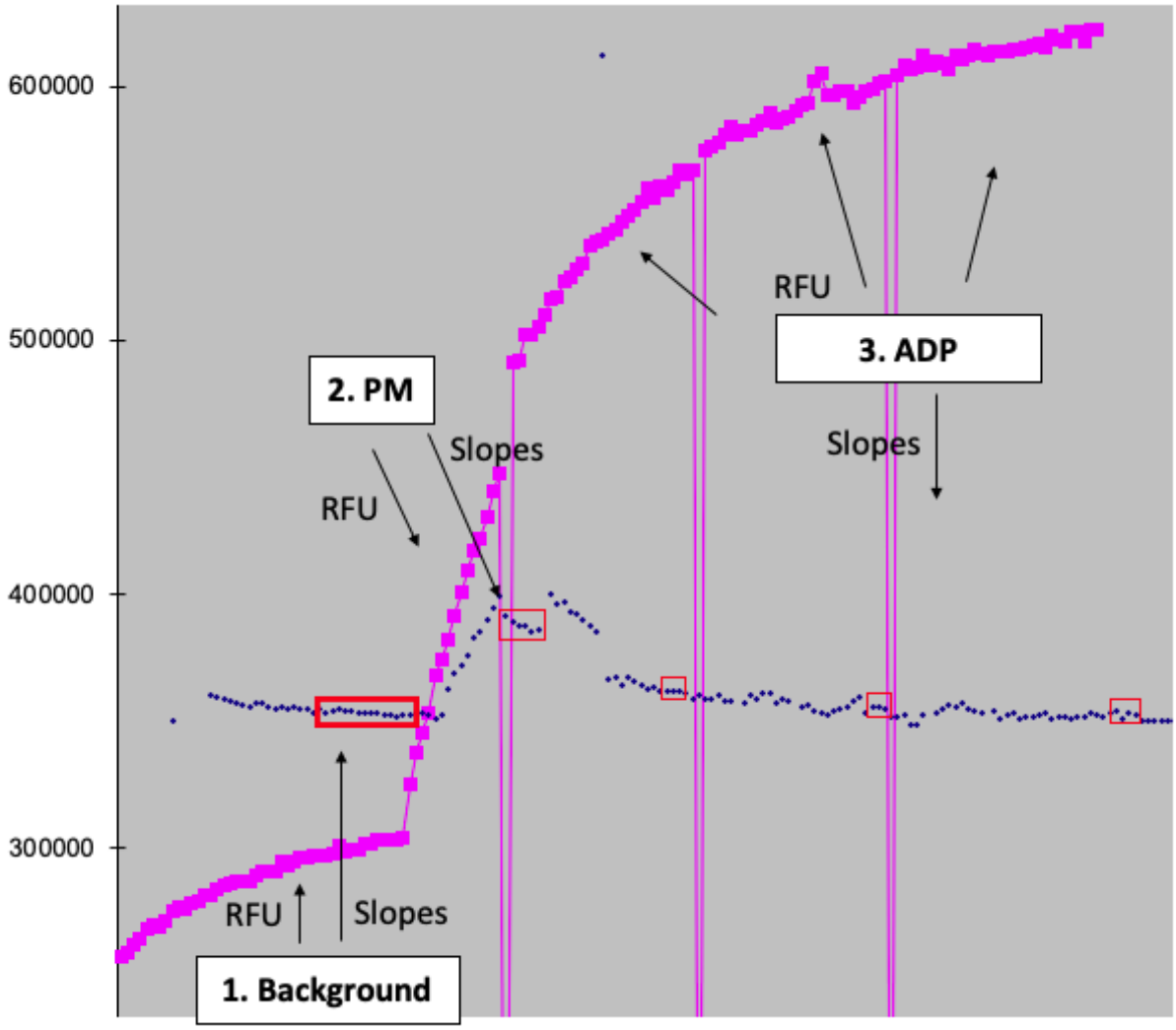

1. Background should be 2-3 minutes, PM 1 minute, ADP 2 minutes each
2. NOTE: PM is increasingly difficult because PM generates so much H_2O_2 that the longer the protocol runs, the more the fiber could be dying due to cell damage. This protocol requires a 1-minute titration and a narrow window to select for averages compared to succinate. **Be extra careful you are NOT averaging slopes of recording data from a previous titration.**
3. Data copied are in cells J5-P5 (corrected rates).

PDH Rotenone Inhibitor

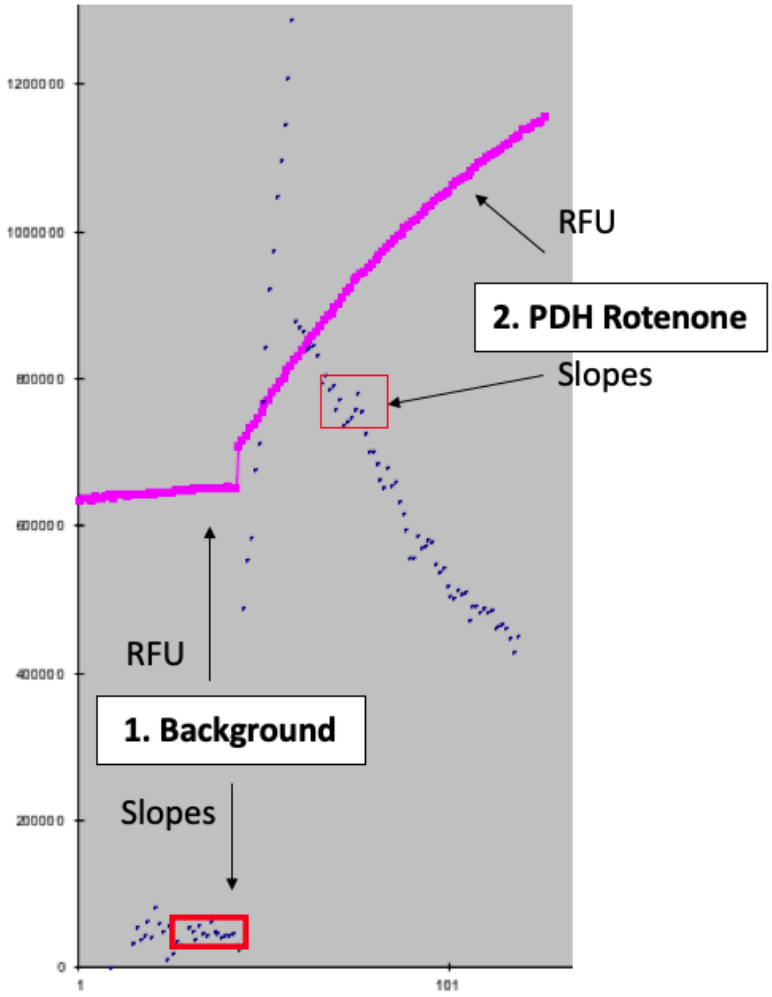

1. Rotenone should be titrated in the cuvette and the cuvette should sit in the fluorometer for 10 minutes. Then 3 minute background and 5 minute pyruvate.
2. PDH is challenging to identify the max rate as the blue dots seem to gradually descend. To pick the appropriate slopes, use slope of the first 40 seconds immediately after adding pyruvate.

Antimycin A

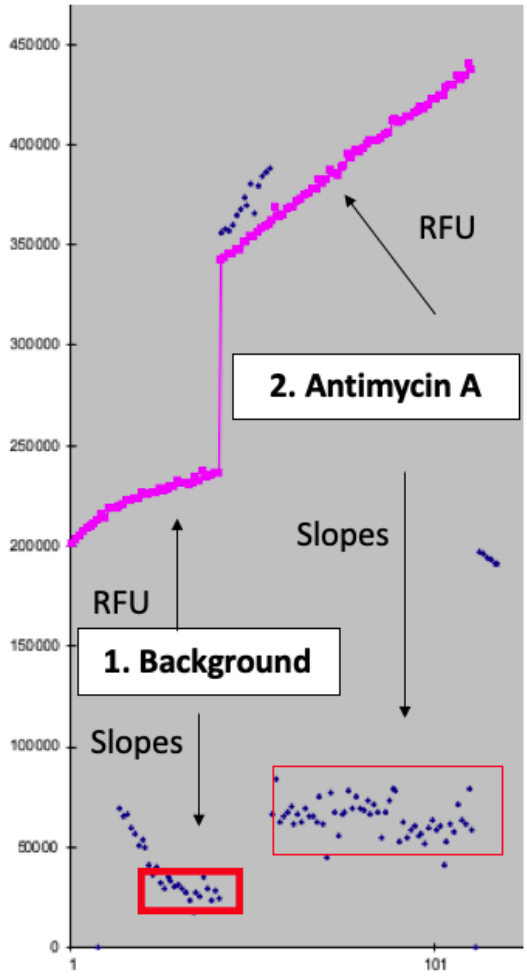

1. When Antimycin A is titrated, there consistently seems to be some autofluorescence that initiates a large increase in RFU. Ignore the values comparing background to Antimycin A as they are irrelevant.
2. **Be extra careful you are NOT averaging slopes of recording data from a previous titration.**
3. Use slope of first 40 seconds immediately after adding Antimycin A!!

NOTE: All graphs were generated using control mice from Luca's Cancer Cachexia thesis. All protocols may not look identical but general trend should be similar.

A.3 CALCIUM RETENTION CAPACITY PROTOCOL

BUFFERS:

BUFFER Y- pH 7.2

Chemical	Molecular Weight	Final Concentration	Addition to *500mL* final volume
Sucrose	342.3	250mM	42.78g
Tris-HCl	157.6	10mM	0.788g
Tris Base	121.14	20mM	1.21g
KH_2PO_4	136.1	10mM	0.68g
BSA	154.2	0.5mg/mL	0.25g

*<u>**ALWAYS**</u> double check molecular weights for supplier-specific chemicals (n=m/M.W.)

- filter once total volume is made
- store in fridge at 4°C – watch for any cloudiness evidence of bacterial growth and you will need to remake
- may require heat to dissolve everything

CRC Assay Buffer – with Creatine (NEW Composition)

Chemical	**Molecular Weight**	**Final Concentration**	**Addition to *120mL* final volume**
Buffer Y (freshly made)			120mL
Creatine	131.13	20mM	0.315g
EGTA		40uM	9.6uL of 0.5M
BLEB		5uM	60uL of 10mM
Calcium Green 5N*	1192.19	1uM	400uL of 0.3mM
Thapsigargin**	650.76	2uM	160uL of 1.5mM

* Dissolve 0.5mg CG5N in 1.398mL water

** 1mg vial, make 1mL, aliquot into 165uL stocks and freeze

- **Aliquot in 900uL aliquots**
- Max age of buffer should be 4 months old within study
-

Calcium Chloride Stocks (MW= 110.98 g/mol) (anhydrous)

Create a stock of 5mM & 50mM $CaCl_2$ dissolved in water and store in 50uL aliquots in freezer.

Procedure

* place cuvettes on stir plate and fill with ddH_2O and 10uL EGTA (0.5M stock) (minimum 10 mins between trials)

1. Harvest muscle and place in <u>ice cold</u> **BIOPS**
2. Separate fibres into bundles (SMALLER than those used for respiration & even more separated) ** always make a spare bundle for each muscle
3. Permeabilize for 30 minutes in BIOPS with 30ug/mL saponin
4. WASH 1: 10 minutes in 1.5mL Buffer Y + 1mM EGTA (3uL of 0.5M)

5. Turn on fluorometer to allow lamp to heat up
6. WASH 2: 10 minutes in 1.5mL Buffer Y + 10uM BLEB (1.5uL of 10mM BLEB) **be conscience of how long bundles are in fridge for (max viability 4 hours)
7. Aspirate out water from cuvette but DO NOT RINSE (keep cuvette lined with EGTA) & add necessary ingredients according to table below and fibre *keep dark
8. Select Calcium Uptake Assay Protocol on PTI Software. Make sure the following parameters are set:
    a. Excitation: 506
    b. Emission: 532
    c. Duration – 3000 seconds
    d. Slit Widths: Excitation 3nM
       Emission 3nM
    e. x-axis window: 2000 seconds
    f. y axis min and max: 200 000 and 500 000 ** this changes depending on strength of the bulb (newer bulbs may be closer 500 000 as the min)

Substrate	Stock Concentration	Addition to cuvette	Final Concentration in Cuvette
CRC Assay Buffer		300uL	
Glutamate	2M	1.5uL	10mM
Malate	1M	1.5uL	5mM
ADP	5mM	1.5uL	25 uM
Fibre ** make sure fibre is at the bottom of cuvette attached to stir bar**			
Collect 400 second background to establish "F-Min"			
$CaCl_2$	5mM	2.5uL	8nmol
Wait 5 minutes or until steady state			
$CaCl_2$	5mM	1.25uL	12nmol (4nmol pulse)
Wait 5 minutes in between pulses and continue pulsing until pore opens			
$CaCl_2$	50mM	3uL	0.5mM Pulse (F-Max)
Wait 3 minutes before final addition, this should establish F-Max but continue to titrate until flat line occurs and F-max is truly established			
$CaCl_2$	50mM	Continue 3uL as necessary until no further increase	0.5mM Pulse (F-Max)

* for each addition remove cuvette from holder and ensure fibre has not been disrupted
**Make sure y axis is no more than 300 000 units or you will miss opening
*** ensure that you have F-Max by continually titrating 50mM Ca^{2+} until no increase is observed
9. Remove bundle and save for freeze drying (if applicable)

BUFFER NOTES

Sucrose: weak anti-oxidant and also stabilizes membranes and contributes to physiological intracellular osmolarity. This buffer stems from isolated mitochondria experiments but membrane stability is thought not to be an issue in PmFB but the buffer persists
Tris-HCl & Tris Base: tris has two forms – base and HCl forms. Tris is a common biological buffer component that buffers protons. Tris stabilize amines and complexes with metal ions in solution- this may play a role in maintaining Ca^{2+} free and bound levels. The combination may be used to maintain pH- as tris base would increase pH and tris base could offset this.
KH_2PO_4: Phosphate buffer- buffers protons

BSA: weak anti-oxidant and also buffers protons
Buffer Y: Best to make this before you take components for CRC buffers out. Largest (volume) component of CRC buffer.
Creatine: allows for mtCK dependent respiration in combination with substrates added to cuvette. You need the addition of ADP to be truly considering mtCK's role in mPTP inhibition
EGTA: Ca^{2+} chelator
BLEB: contraction inhibitor
Calcium Green 5N: this is a membrane impermeant fluorophore that binds to Ca^{2+} unbound in the cytosol which is at equilibrium with the CRC buffer. When Ca^{2+} is titrated into the cuvette, an increase in fluorescence is observed as Ca^{2+} associates with the fluorophore. As Ca^{2+} is imported into the mitochondria, a decrease in fluorescence is observed as Ca^{2+} dissociates from the fluorophore.
Thapsigargin: SERCA inhibitor that forces Ca^{2+} into mitochondria and not SR but we may be ignoring any uptake by nucleus, etc.

CALCIUM RETENTION CAPACITY ASSAY ANALYSIS

Phase I: Exporting Data

1. Go to the lab computer where CRC experiments were completed and open Felix software
2. Open CRC file, right click labelled trace and click "export trace". These files will export as a .txt file that can be opened by excel. Save all files in a folder and use a USB to transfer data over to a personal computer and back up data on OneDrive (or any other location where you keep your data)

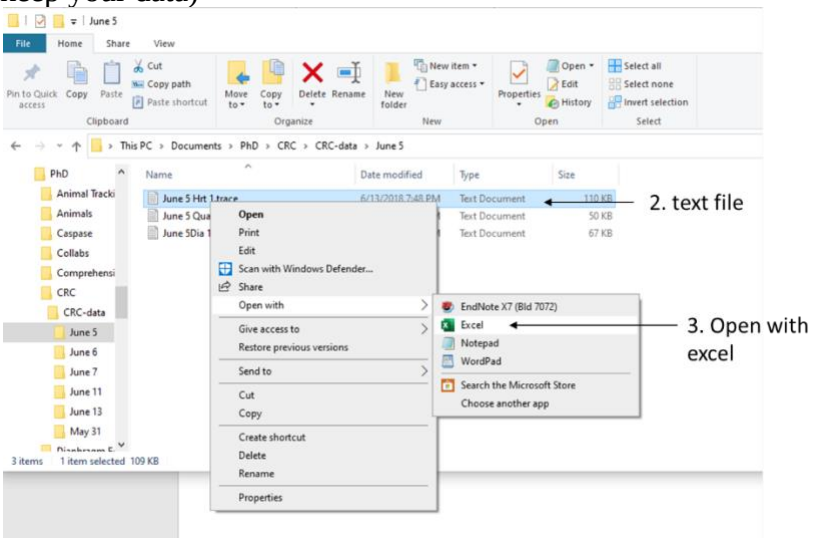

3. Once data is on personal computer where you wish to analyze, right click file you wish to analyze and click "open with excel".
4. Highlight first 4 rows and click delete.

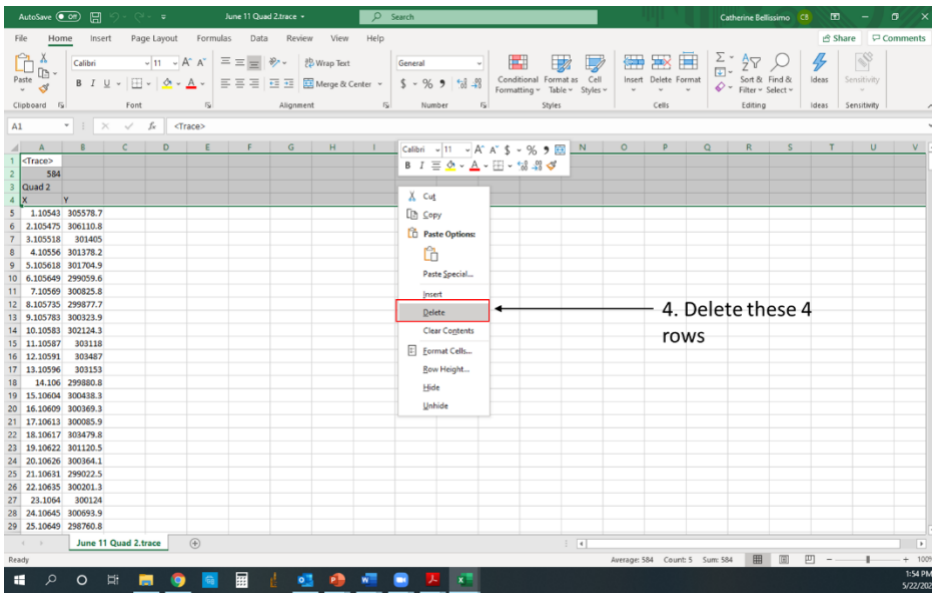

5.All that should be remaining in the file is data in column A and column B. Column A will contain time data (independent variable) while column B will contain fluorescence intensity data (dependent variable). Copy all column A and column B data and paste it into the CRC analysis template

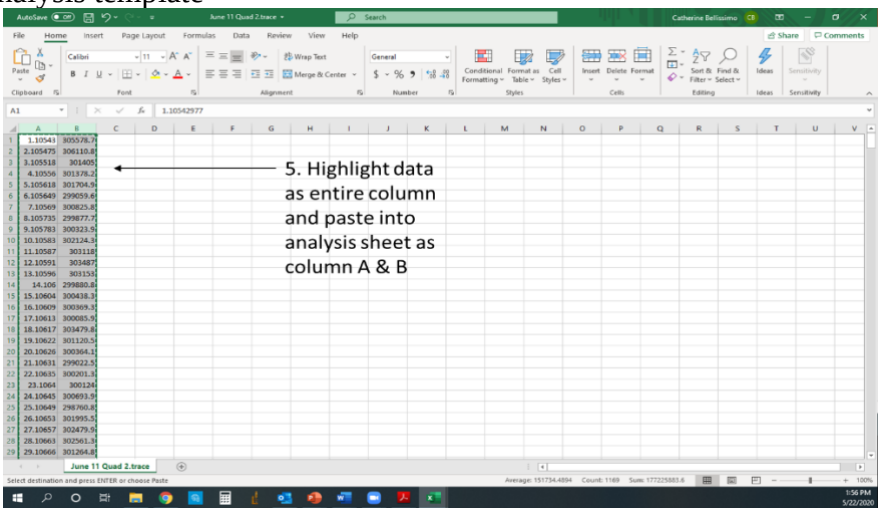

Phase 2: Analysis Template

1. Below is an example of the analysis template. On the left, you will see your imported data. It is very important to paste the data as a column and not as just data. This prevents any of the previous trace being included in you last trace.
2. In the center, you will see the area to insert your peaks and bottoms of the titrations of calcium. This area allows you to identify how much Ca^{2+} the mitochondria will uptake before mPTP is forced to open. Remember to delete the location of any previous peaks and bottoms from older titrations when performed your analyses. For example if you

only had 10 titrations before mPTP opened then you should delete the information in column E for any titrations below B10.

3. On the right, you will see your data graphed. If you do not see a complete image of your trace, then double check the x and y axes are at full scale. You can also check to see if all your data is graphed by clicking on your data and seeing if all your data has been highlighted.

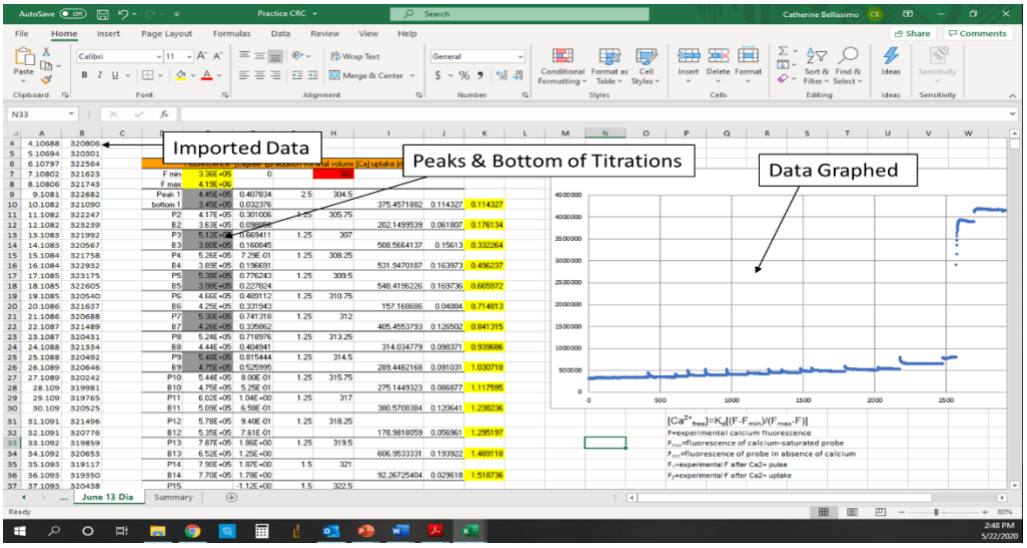

To determine either the free calcium concentration of a solution or the K_d of a single-wavelength calcium indicator, the following equation is used:

$$[Ca^{2+}]_{free} = K_d \left[\frac{F - F_{min}}{F_{max} - F} \right]$$

where F is the fluorescence of the indicator at experimental calcium levels, F_{min} is the fluorescence in the absence of calcium and F_{max} is the fluorescence of the calcium-saturated probe. The dissociation constant (K_d) is a measure of the affinity of the probe for calcium.

The CRC assay works based on the dissociation constant of Calcium Green 5N and identifying the peak and bottom of each titration to examine the difference which represents the amount of calcium taken by the mitochondria. Calcium Free is the concentration of calcium in the solution, Kd is the dissociation constant which is 14uM for Calcium Green 5N. F represents experimental calcium fluorescence of the pulse you are examining (peak and bottom are analyzed separately). F_{min} represents the fluorescence of the dye in the absence of calcium and F_{max} represents the fluorescence of the dye saturated by calcium. You can assess F_{min} and F_{max} by using the "=MIN(B:B)" and "=MAX(B:B)" excel functions respectively. But there are some specific considerations. If you see variability in these values please consult.

Phase 3: Understanding the Analysis Template

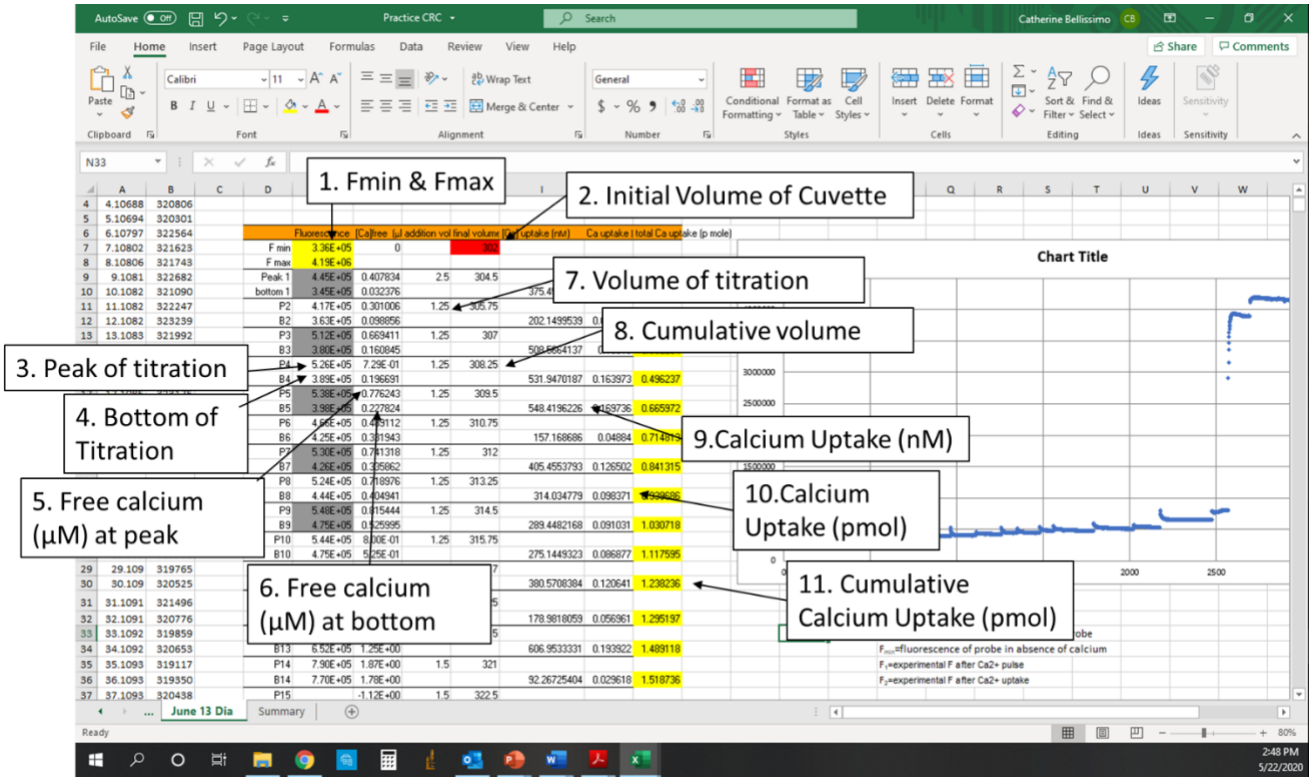

1. Fmin & Fmax: are unique points that need to be identified in each trace. You can assess F_{min} and F_{max} by using the "=MIN(B:B)" and "=MAX(B:B)" excel functions separately but double check these by hovering cursor on the minimum (a. in figure below in important points to consider) and maximum (b. in figure below) in the graph. See F_{min} and F_{max} in important points to consider for further discussion.
2. Initial Volume of Cuvette: this presents the volume of the cuvette at the beginning of the experiment prior to the addition of calcium in microliters. See CRC protocol for exact volumes but for most experiments the initial volume is 306µL (300µL of CRC buffer + 1.5µL of 1M malate + 1.5µL of 2M glutamate + 3µL of 5mM ADP).
3. Peak of Titration: First you will need to identify how many titrations you have (it is a good idea to keep a hard record to the number of titrations when performing the assay). Hover your cursor above the peak of a titration to identify the location of the value- record this number and repeat for all peaks. This is illustrated as b. in the figure below. You will need to consult the raw data on the left-hand side of the analysis template to make sure the values you record are the absolute maximum. Once you have confirmed the correct peak insert this B location into the E column. For example, if B323 has been identified as the 5th peak you would insert =B323 in cell E17.

4. Bottom of Titration: identify the (c. in figure below) bottom of each trace by hovering cursor over the approximate location. Record this number and verify with raw data that this is approximately the minimum. For example, if B410 has been identified as the 5th bottom you would insert =B410 in cell E18.
5. Free calcium at peak in µM: the peak value you recorded in column E is applied to the equation, where 14uM is the dissociation constant and F is the fluorescence you identified. The value calculated is expressed in µM.
$$[Ca^{2+}]_{free} = 14\mu M \times \frac{[F-F_{min}]}{[F_{max}-F]}$$
6. Free calcium at bottom in µM: the bottom volume recorded in the column E is applied to the above equation and converted into µM.
7. Volume of titration in µL: ensure that this value is the correct volume you titrated. For example, some occasions you will titrate 2.5µL in the first two titrations- ensure that this is reflected in your analysis.
8. Cumulative Volume in µL: the value above is added to initial volume in cuvette and all preceding titrations.
9. Calcium uptake (nM): the value from steps 5 and 6 are subtracted from each other (µM) and converted into nM (by multiply by 1000). This should always yield a positive number as peaks should have higher Calcium than bottom. If your value is negative consult the raw data and assess if you have correctly identified the peak and bottom.
10. Calcium uptake in pmol: the concentration of calcium uptake is converted into pmol by multiplying by the volume of the cuvette to Calcium uptake in nM and correcting to yield pmol as final units.
11. Cumulative calcium uptake in pmol: the preceding calcium uptakes are added together. Make sure that all titrations are being considered.

Important Points to Consider:

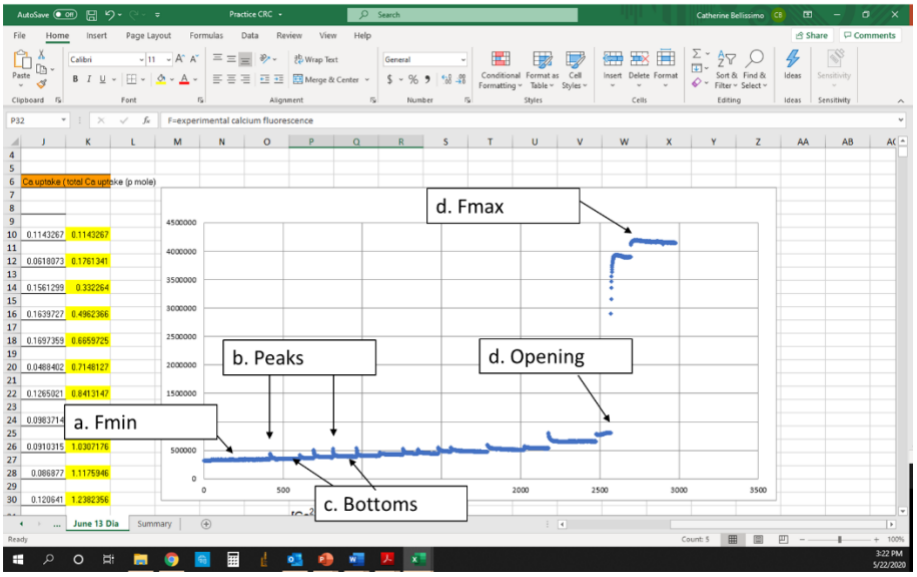

- Above is an example of the graph included in the analysis with major components of the analysis identified:
    - F_{min}: make sure that the value you select is from a steady state. If you are using the excel MIN function, ensure that this value makes sense. If you notice your background is continually increasing or decreasing, then you should manually select the F_{min}, as the value the =MIN selects would just be the lowest number. Make sure you do not have noisy background. Don't be afraid to tap down the cuvette to make sure the bundle adheres to stir bar.
    - F_{max}: you can use the =MAX function to identify your Fmax but ensure that you have effectively saturated the fluorophore when performing the assay. Continue to titrate 50mM $CaCl_2$ until no further increase in fluorescence is observed. If you notice F_{max} variability you can consult Chris about it. One option is to remove very large outliers in F_{max} data and then average all remaining F_{max} values. Once averaged this new value will get applied to all data to help reduce data variability.
    - Peaks: you can use the graph as a guide to identify your peaks. If necessary, consider altering the x and y axis on the graph (you can do this by right clicking on axis and clicking edit axis) to remove the Fmax. This will give you a clearer view of the peaks BUT ALWAYS CONSULT THE RAW DATA. You can also highlight the peaks on the raw data in column B. Two of the largest errors include inputting the wrong value location (ie B465 is peak but you right B645) or not completely removing previous data on a new analysis (ie you did not paste as a column and you have titrations from an older data set).
    - Bottoms: this represents the lowest fluorescent value in the titration. You should hover over the approximate lowest value but be considerate of noisy data and double check values with raw data.
    - Openings: openings of the mPTP are often very subtle and may be hard to identify. Always consult with more experienced lab mates if you are unsure if you have an opening. Additionally, you can allow the bundle to run longer until you see a clearer indication of opening or add an additional titration of calcium to prove the opening. If you have an opening the mitochondria will not uptake calcium and fluorescence

will just continue increase. Openings are not always sharp increases-see additional examples of subtle openings below:

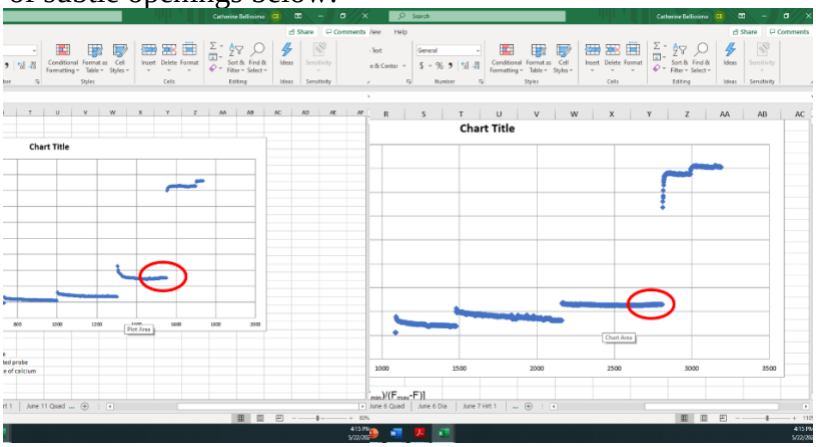

Important Points to Consider (Continued):

- Age of buffer & stock: within a study to reduce F_{max} variability use buffer within 4 months from making. You might be able to be push this to 6 months but to be safe and use within the 4month mark. Stock age might also be an issue. Fisher recommendation for shelf life and stability:
    - As a powder: if no expiration date is posted on the product label or vial label, it has a warranty period of 1 year from the date of shipment.
    - In a liquid: stable for approximately 6 months, stored frozen and protected from light. For longest stability, Calcium Green 5N (salt form) is best stored as a solid. If making up in water and you have access to a vacuum pump or SpeedVac, one may make up the solution in high purity water, make smaller aliquots in separate vials and for the vials not used, evaporate off the water to return the smaller aliquot back to solid form (do not use heat in the evaporation process).
- When making new batches of CRC buffer, test out the buffer (in triplicate) before actual study days. When testing, assess with and without fibre, checking both F_{min} and F_{max} to make sure these values are in range.

A.4 IMMUNOFLUORESCENCE (MYOSIN HEAVY CHAIN STAINING)

All section/slide incubations for this procedure are done at room temperature (RT), on the shaker, and with 50-100µL of solution (only large sections/areas require 100µL). Make sure slides are as flat/level as possible when they are in the incubation container. Also, when blotting slides, even though it is important to remove as much of the solution as possible, the Kimwipes will leave fabric fibers on the sections which show up very brightly blue on the microscope. So, avoid touching the pap pen area with the Kimwipe. Finally, make up antibody dilutions immediately before they are applied.

Set Up:

1. Container
    a. Put wet paper towel on top of lid covered by parafilm held up by tape (this ensures slides will not get dried out)
2. PBS
    a. 1 tablet/100mL of ddH_2O
    b. Filter and keep at room temperature

3. Blocking
    a. 10% Goat Serum kept in freezer – 400uL aliquots
        i. **If staining cocktail** - 1mL of blocker per slide
            1. 900uL PBS and 100uL goat Serum

4. Primary (make immediately before using)
    a. **Primary Cocktail** (leave on rocker away from light for 2 hours)
        i. MHCl (BA-F8) @ 1:25 – IgG2b: blue
        ii. MHCIIa (SC-71) @ 1:500 – IgG1: green
        iii. MHCIIb (BF-F3) @ 1:50 – IgM: red
        iv. MHCIIx → This will not be stained so it will be black.
        v. NOTE: these dilutions are for hybridomas at ~50ug/uL

5. Secondary (make immediately before using)
    a. **Secondary Cocktail** (leave on rocker away from light for 1 hour)
        i. Alexa Fluor 350 IgG_{2b} 1:1000 (blue)
        ii. Alexa Fluor 488 IgG_1 1:1000 (green)
        iii. Alexa Fluor 568 IgM 1:1000 (red)

Procedure:

1. Air dry slides for 10 minutes at room temperature and outline sections in pap pen (optional).
2. Incubate sections for 1 hour in blocking solution
3. Blot dry slides. Incubate section in 1˚ antibodies appropriately diluted in blocking solution (see above). Give the stock antibody tubes a quick shake/inversion before pipetting out of them. – leave away from light, on rocker for 2 hours.
4. Wash slides 3 x 5 minutes in a Columbia jar with 1 x PBS.

5. Blot dry slides. Incubate sections in 2˚ antibodies appropriately diluted in blocking solution for 1 hour at room temperature in the dark. (Note: precipitate forms in the stock tubes which show up as bright spots on the microscope; centrifuge for 15 seconds before pipetting out of stock tubes. Ensure as little light as possible makes contact with the 2˚ antibodies and sections from this point.)
6. Wash slides 3 x 5 minutes in a Columbia jar with PBS. Take the mounting medium, nail polish and coverslips.
7. Apply 15µL of Prolong to each slide and mount with a number 1 coverslip. (Perform this step in the microscope room in almost total darkness.) The coverslip can be pressed gently to remove bubbles, but do not apply pressure direction above sections, they will squish.
8. Tack the corners of the coverslip down with nail polish and place in a labeled, light-proof slide box.
9. Slides can be imaged after the nail polish has dried (5 to 10 minutes), but next day imaging seems to work better as the Prolong is allowed to set. Slides should be imaged no longer than 2 days after staining.

CSA/MFD by Fibre Type Analysis

In skeletal muscle there are a number of isoforms of myosin heavy chain that dictate muscle fibre types. This is one of multiple naming classifications for muscle. In humans there are only type I, IIA & IIX fibres while in rodents there are type I, IIA, IIX and IIB. Skeletal muscles are always made up of a combination of different fibre types that can dictate the oxidative capacity and twitch kinetics (force development and relaxation).
Fibre type spectrum & colouring

- Type I (blue)→ I/IIA→ IIA (green)→ IIA/X→ IIX (black)→ IIX/B→ IIB (red)

To analyze CSA/MFD:
We need to apply a scale calibration to these images to convert pixels into microns. When imaging you will need to take an image at the corrective objective with a scale bar saved. For the EVOS imager, typically use 125um scale bar.
Scale is 125umicrons is 290 pixels (Can accept 285-295 range) ** MUST BE CONSISTENT FOR THE STUDY

1. To add scale to image J
2. Open scale image- take the line tool and draw across scale bar
3. Analyze set scale→ automatically populate pixel length, you will need to manually type in known distance and unit (125 & microns)
4. Any other images you open with Image J will have that calibration→ just remember to uncheck popup box that asks to disable calibration

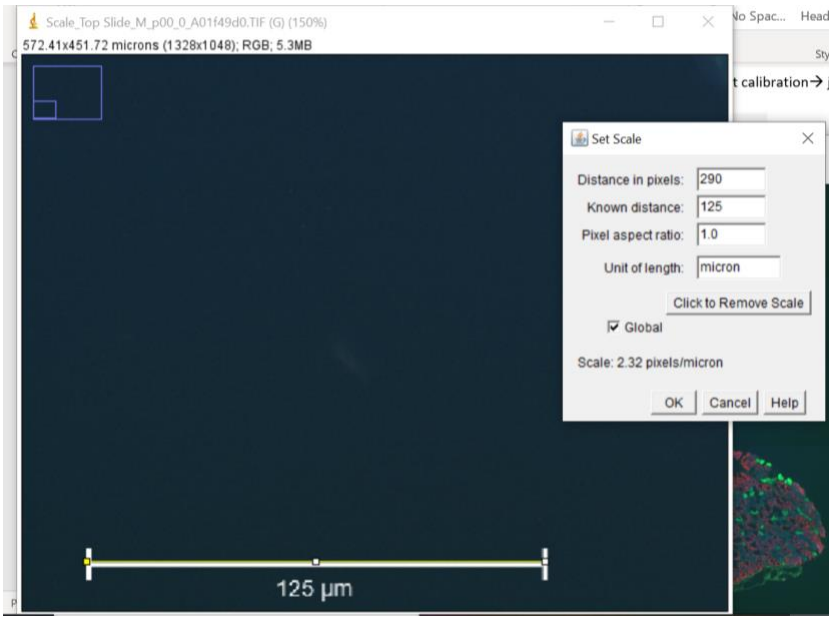

To add in Feret Diameter as a Measurement

1. Analyze→ Set measurement → check Feret diameter

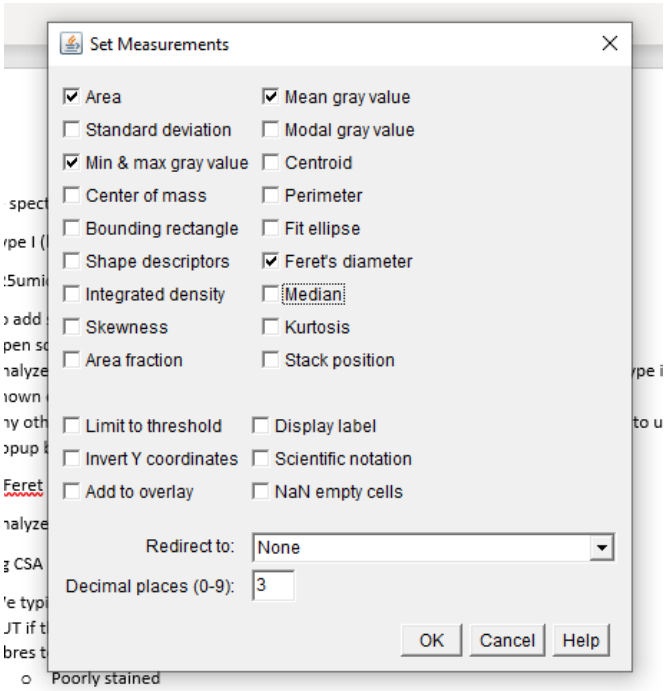

Measuring Cross Sectional Area (CSA)

2. Circle about **<u>30-50 fibers</u>** of each type by using the polygon tool and outlining the entire fibre. Make sure you are very zoomed in to see your fibres. Click "t" after you are done and the ROI manager will open up and highlight your fibre. Make sure "show all" is selected so you can see what fibres you have selected as you continue on.
    a. BUT if there are few fibres of a specific type then circle all
    b. NOTE: if fibres sizes are very inconsistent and you have a very large section you can circle more than 30 fibres.

c. If you want more contrast to see black (IIX) fibres go to Image → Adjust --> color balance and select blue from pull down menu and increase brightness and select APPLY ** DO not save over the image!!
* try not to make your fibre type selections after increasing brightness ---> this is purely for contrast to help you see the fibres better. This is not always necessary.

3. Fibers to avoid circling:
    a. Poorly stained (can't identify if they are supposed to be red, green or blue; remember black fibers are IIX)
    b. Hybrid fibers **** (you can analyze these if you are wondering if the muscle is transitioning but its not often done)
    c. Fibers on stitch lines (the image you see is actually a composite of multiple images so sometimes the often we use doesn't do the best job imaging.
    d. Longitudinal sections (example below)- these are when fibers are pulled as they are cut or they are cut at a poor angle. They are not the true fiber size.

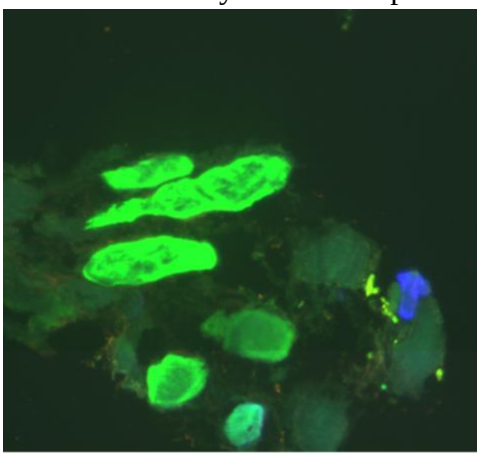

4. Once you are done circling all fibers in ROI manager highlight all areas and click measure
5. Take all measurements and paste into excel spread sheet- you cannot select specific columns in results on image J so easiest to paste into excel and then copy specific columns.
6. Copy over CSA (area) and MFD (MinFeret) into Analysis Sheet

7. Be careful to paste CSA under CSA and MFD under MFD under the correct section ID and correct fibre type. Each fibre type has their own tab for each measurement.

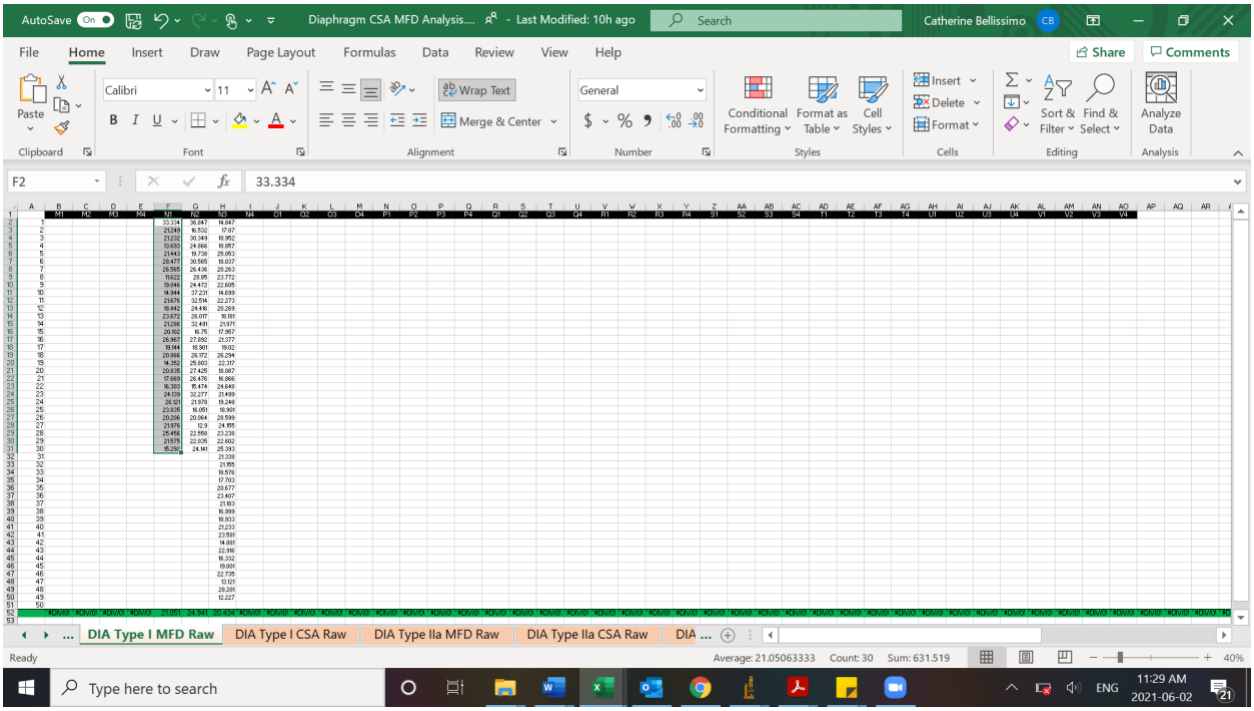

SAVING ANALYSIS

If you want, you can save analysis of circled sections by going to ROI manager→ FILL and it will automatically fill in each section with a colour. Then save the image separately as Sample ID_ Fibre type. This allows someone to go back and check your analysis and compare. See example below: